

Particle fusion in localization microscopy

Heydarian, Hamidreza

DOI

[10.4233/uuid:acdebbdd-009e-4a31-a79b-72fab820b85f](https://doi.org/10.4233/uuid:acdebbdd-009e-4a31-a79b-72fab820b85f)

Publication date

2020

Document Version

Final published version

Citation (APA)

Heydarian, H. (2020). *Particle fusion in localization microscopy*. [Dissertation (TU Delft), Delft University of Technology]. <https://doi.org/10.4233/uuid:acdebbdd-009e-4a31-a79b-72fab820b85f>

Important note

To cite this publication, please use the final published version (if applicable).
Please check the document version above.

Copyright

Other than for strictly personal use, it is not permitted to download, forward or distribute the text or part of it, without the consent of the author(s) and/or copyright holder(s), unless the work is under an open content license such as Creative Commons.

Takedown policy

Please contact us and provide details if you believe this document breaches copyrights.
We will remove access to the work immediately and investigate your claim.

PARTICLE FUSION IN LOCALIZATION MICROSCOPY

PARTICLE FUSION IN LOCALIZATION MICROSCOPY

Proefschrift

ter verkrijging van de graad van doctor
aan de Technische Universiteit Delft,
op gezag van de Rector Magnificus Prof. dr. ir. T.H.J.J. van der Hagen,
voorzitter van het College voor Promoties,
in het openbaar te verdedigen op dinsdag 17 maart 2020 om 10:00 uur

door

Hamidreza HEYDARIAN

Master of Science in Visual Computing,
Saarland University, Saarbrücken, Germany,
geboren te Mashhad, Iran.

Dit proefschrift is goedgekeurd door de

promotor: Prof. dr. B. Rieger
promotor: Prof. dr. S. Stallinga

Samenstelling promotiecommissie:

Rector Magnificus,	voorzitter
Prof. dr. ir. B. Rieger,	Technische Universiteit Delft
Prof. dr. ir. S. Stallinga,	Technische Universiteit Delft

Onafhankelijke leden:

Dr. J. Ries,	European Molecular Biology Laboratory, Heidelberg, Duitsland
Dr. P. Dedecker,	Katholieke Universiteit Leuven, België
Prof. dr. ir. F. J. Verbeek,	Universiteit Leiden
Dr. S. Cox,	King's College London, Verenigd Koninkrijk
Prof. dr. ir. B. P. F. Lelieveldt,	Technische Universiteit Delft
Prof. dr. ir. L. J. van Vliet,	Technische Universiteit Delft, reservelid



This work was carried out in the Computational Imaging group of the Imaging Physics (ImPhys) department at the faculty of Applied Sciences of Delft University of Technology and was supported by the European Research Council (grant no. 648580).

Keywords: single molecule localization microscopy, particle averaging, particle fusion, SMLM

Printed by: Gildeprint, Enschede, The Netherlands.

Front & Back: Fusion of 383 DNA-origami nanostructures imaged using DNA-PAINT technique.

Copyright © 2020 by H. Heydarian

An electronic version of this dissertation is available at
<http://repository.tudelft.nl/>.

CONTENTS

1	Introduction	1
1.1	Single molecule localization microscopy	2
1.1.1	SMLM modalities and data acquisition	2
1.1.2	Image processing	4
1.1.3	Postprocessing and quantification	6
1.2	Data alignment	6
1.2.1	Image alignment applications	6
1.2.2	Point cloud registration applications.	8
1.2.3	Classification of point cloud registration methods	10
1.3	Particle fusion in SMLM.	12
1.3.1	Template-based particle fusion	12
1.3.2	EM inspired particle fusion for SMLM	14
1.3.3	Pyramid particle fusion	15
1.3.4	Accelerated pyramid particle fusion	16
1.4	Research questions and thesis outline	17
	References	18
2	Template-Free 2D Particle Fusion in Localization Microscopy	23
2.1	Introduction	24
2.2	Results	25
2.3	Methods	29
2.3.1	Materials.	29
2.3.2	Microscopy setup	29
2.3.3	DNA origami self-assembly	29
2.3.4	Superresolution DNA-PAINT imaging with DNA origami	30
2.3.5	Single and multiemitter fitting of experimental data	31
2.3.6	Simulation setup.	32
2.3.7	All-to-all registration.	32
2.3.8	Computational complexity.	35
	References	35
2.A	Appendix	38
3	Three dimensional particle averaging for structural imaging of macromolecular complexes by localization microscopy	51
3.1	Introduction	52
3.2	Results	53
3.3	Methods	56
3.3.1	Sample preparation	56
3.3.2	Single molecule experiments.	58

3.3.3	Data fusion pipeline	61
3.3.4	Simulation setup.	62
3.3.5	Registration error measure in simulations	62
3.3.6	Pose variation in simulation	63
3.3.7	Analysis of NPC structural parameters	63
	References	64
3.A	Appendix	67
4	Conclusion and outlook	81
4.1	Conclusion	82
4.2	Short-term outlook	83
4.3	Long-term outlook	85
	References	88
	Summary	91
	Samenvatting	92
	Curriculum Vitae	93
	Acknowledgements	95

1

INTRODUCTION

1.1. SINGLE MOLECULE LOCALIZATION MICROSCOPY

Fluorescence microscopy is a standard and ubiquitous tool in biology to observe and study subcellular structures. The success of this imaging technique primarily relies on two factors: enhanced contrast enabled by the use of fluorescence and high specificity that is brought about by molecular labeling. A drawback of conventional fluorescence microscopes has been that the achievable resolution was fundamentally limited by the diffraction of visible light to about 200 nm.

Ernst Abbe, in 1873, analyzed the diffraction of light in image formation by a lens system and showed that an optical microscope cannot distinguish object features less than $d = \lambda/(2NA)$ apart. In this formula, λ is the wavelength of light (about 400-700 nm) and $NA = n \sin(\alpha)$ is the numerical aperture (about 1.4 for typical high NA objectives), defined in terms of the sample refractive index n and the semi-angle α of the cone of light captured by the objective lens. This limit was a barrier to study nanoscale cellular structures and processes until the advent of so-called superresolution microscopy [1].

Superresolution microscopy or optical nanoscopy is the set of techniques and tools which allow imaging well below the diffraction limit using far-field light microscopy [2]. Among these techniques, single molecule localization microscopy (SMLM) achieves sub-diffraction resolution by turning the emission of fluorescent molecules on and off (blinking), such that emitting molecules that are spatially proximate are typically not imaged at the same time [3]. This is achieved by using another dimension (time) in the image acquisition to record the blinking events at multiple frames. In SMLM, the precision with which the location of each individual molecule can be determined depends on the number of collected photons N and scales with $(\lambda/NA)/\sqrt{N}$.

Optical nanoscopy with SMLM is a multidisciplinary technique that starts with sample preparation, followed by data acquisition, data analysis and postprocessing. In the following sections, we will briefly discuss the relevant parts for this thesis and refer the interested reader to ref. [3, 4].

1.1.1. SMLM MODALITIES AND DATA ACQUISITION

EPI-FLUORESCENCE AND TIRF

Two popular microscopy setups for superresolution imaging are epi-fluorescence and total internal reflection fluorescence (TIRF) setups (Figure 1.1a). Both techniques share almost the same principle in which the labeled specimen is illuminated by a beam of light, originating from a light source, reflected by a dichroic beam splitter and focused by the objective lens. This illumination will cause the fluorescent molecules to transiently go to the excited state and return to their initial ground state while emitting fluorescent photons at a lower frequency (higher wavelength). The emission light from the specimen is captured by the objective lens, passes through the dichroic beam splitter and is focused by the tube lens on the image sensor. The two imaging systems are, however, different in the way that the sample volume is illuminated (Figure 1.1b). While, in the epi-fluorescence setting, the excitation light passes through the entire sample volume, in TIRF, only a thin layer of the entire volume, directly adjacent to the coverslip, is illuminated.

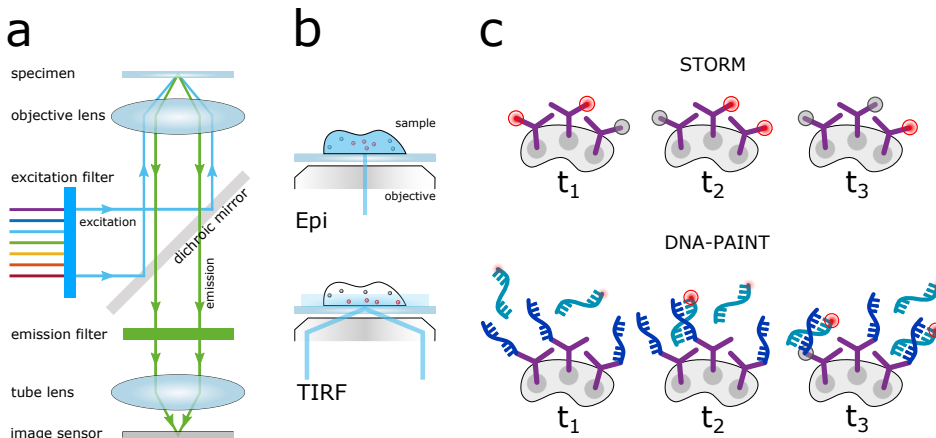


Figure 1.1: SMLM modalities and data acquisition. (a) Simplified schematic of a typical epi-fluorescence microscope showing how the excitation and emission paths are configured to be on the same side of the sample (b) Illumination beams at the interface of the objective lens and the coverslip in epi-fluorescence and TIRF settings. While epi-fluorescence activates more fluorophore in depth, TIRF allows for thin sectioning of the sample close to the coverslip. (c) STORM versus PAINT. Both modalities rely on the localization of fluorescent molecules. STORM works based on stochastic blinking of fixed fluorophores and, in PAINT, blinking occurs through cycles of binding and unbinding of imager strands that are present in the imaging volume and docking strands which are attached to the structure of interest in thin layer of the sample volume close to the coverslip.

PAINT AND STORM

Researchers proposed different sample preparation protocols and methods for achieving stochastic on-off switching during the past ten years, making use of a wide range of photo-biochemical techniques, introducing a plethora of acronyms [4–7]. In this thesis, the used data was acquired with stochastic optical reconstruction microscopy (STORM) [6] and point accumulation for imaging of nanoscale topography (PAINT) [7], which are two of the most common modalities for SMLM (Figure 1.1c). Blinking in STORM is induced by illuminating the fluorophores that are permanently bound to the structure of interest at high intensity. This causes the majority of the molecules to go into a dark, non-emitting state, from which they return at a relatively low rate. The minority of molecules in the normal, emitting state undergo many absorption-emission cycles that produce the photons that make up the fluorescent signal. In each cycle, there is a small probability of photobleaching. The on and off switching in PAINT occurs when single strand DNAs carrying a fluorophore (imager strand) transiently bind to their complementary strands (docking strand) and some later detach. The binding gives a huge increase in fluorescence emission in the context of TIRF imaging of a relatively thin and flat structure close to the cover slip. Typically, PAINT requires less excitation power and it accumulates more localizations per binding site as the imager strands are constantly present in the solution. This is at the cost of a longer acquisition time compared to STORM. Moreover, while the distribution of localizations per site is a mixed geometric-Poisson in STORM [8], it is Poissonian for PAINT. This is mainly due to the bleaching versus nonbleaching nature of fluorescence emission in these two modalities.

1.1.2. IMAGE PROCESSING

On the order of 10-100 thousands of frames are recorded in a typical SMLM experiment, such that in each frame only a small subset of the fluorescent molecules is in the on-state. Recording this huge number of frames ensures that most of the fluorescent molecules on the labeled structure are captured at least once. In contrast to conventional light microscopy images, these raw frames are not immediately interpretable, and several image processing steps are needed in order to fully recover all single molecule positions. This is achieved in an image processing pipeline which consists of the following steps [9] (Figure 1.2):

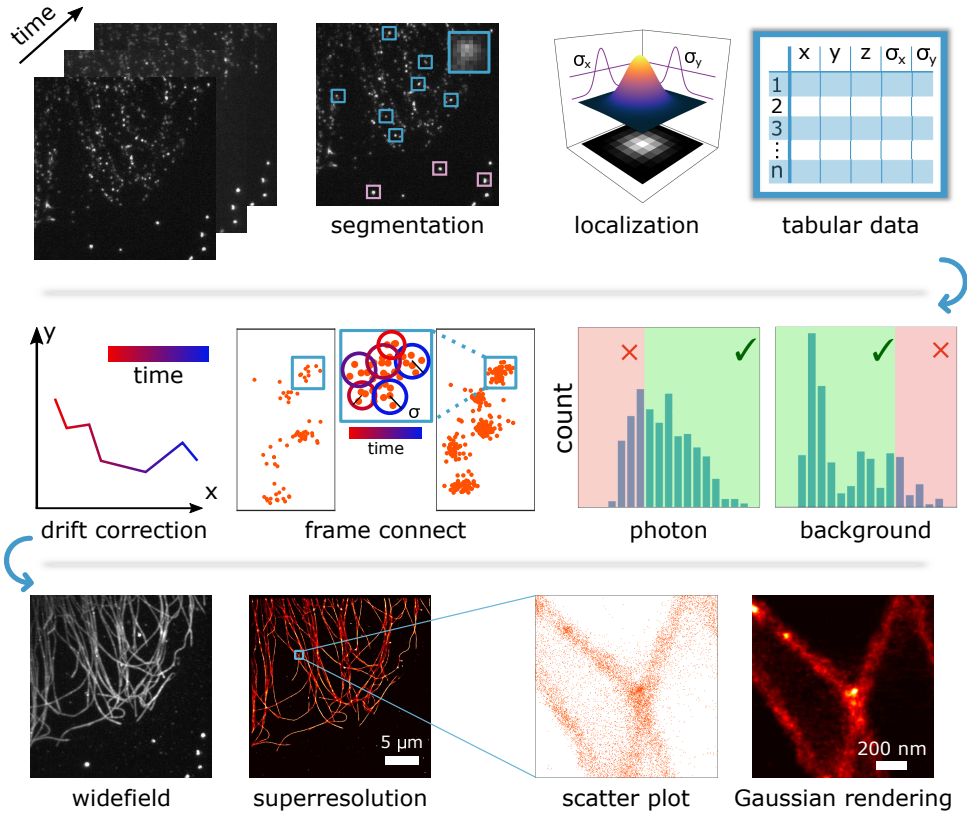


Figure 1.2: SMLM image processing pipeline. In a typical SMLM experiment, thousands of frames capture the blinking events of fluorescent molecules. The position of fluorescent molecules is found from the segmented regions of interest (blue squares) from the raw frames to form a list of coordinates. Filtering based on the estimated background and photon count, merging of repeated localizations (so-called frame connect) and drift correction (e.g. using fluorescent beads as in the purple squares) are the next steps in this pipeline. The last step is to stack all the found localizations in a single reconstruction and visualize them.

SEGMENTATION

The very first step in analyzing raw frames is the identification of the pixels containing signals from single molecules. The main challenge here is to discriminate between the

background noise and the (probably weak) signal from the fluorescent molecules. Various methods have been proposed in order to do the segmentation of the raw frames which are based on relatively simple user defined thresholds for separating signal from the background [6] to sophisticated probabilistic frameworks [10].

LOCALIZATION

Segmentation provides molecule locations with regions of interest (ROIs). It is, however, desirable to estimate the precise fluorescent molecule positions by incorporating the image formation model. Moreover, valuable information about the fluorescent emitters can be estimated along with its coordinates. This includes photon count, localization uncertainties (in x , y , and z) and background. Maximum likelihood estimation (MLE) and least squares (LS) fitting of the point spread function (PSF) model to the ROIs are the most effective and widely used approaches for localization [11, 12].

FILTERING

Autofluorescence, out-of-focus, diffusing and overlapping emitters result in poor localizations. Therefore, the next step in this pipeline is to remove them from further analysis. The filtering of bad localizations is mostly done based on the estimated parameters in the localization step (e.g. low photon count and high background), their computed Cramér-Rao lower bound and the goodness of fit to the PSF model [6]. Furthermore, localizations of the same fluorophore are connected across sequences of frames if they are in the neighborhood of each other (distance less than a few localization uncertainties). This results in a reduced number of localizations and better localization precision values.

DRIFT CORRECTION

Stage drift is a typical problem in SMLM experiments, and it can be severe for some modalities like DNA-PAINT with long acquisition time (up to a few hours). Drift correction can be done by using fluorescent beads as fiducial markers, as these can be tracked easily, or by performing 2D registration of localizations, e.g. by cross-correlation between blocks of consecutive frames that are grouped together. Recently, Dai et al. [13] proposed drift correction using synthetic nanostructures, e.g. grid patterns, as an alternative to beads, and achieved ~ 1 nm residual drift with this method.

RECONSTRUCTION AND VISUALIZATION

In the very last step, the list of coordinates (localizations) are accumulated to form a single reconstruction, i.e. an SMLM image. Therefore, in contrast to conventional microscopy techniques, this reconstruction is not a pixelated image on a uniform grid but rather a list of coordinates in 2D/3D Cartesian space. Naïvly, one can use a scatter plot to visualize localization data. But this only works when the data is sparse. The standard ways of visualization are two-dimensional histogram binning, possibly combined with a small amount of Gaussian blurring, and rendering of each localization using a 2D Gaussian blob with a standard deviation that is equal to its localization uncertainty [14].

1.1.3. POSTPROCESSING AND QUANTIFICATION

Researchers have developed a variety of methods and algorithms to analyze SMLM images and find new insights into nanoscale cellular structures and processes. Resolution assessment [15], cluster analysis [16], structural quantification [8, 17] and particle fusion [18] are among the techniques that have been developed so far in order to interpret this data. The focus of this thesis, which falls in this stage of the SMLM pipeline, is to propose a new approach for the alignment of a set of images of the same underlying structure (“particle fusion”) in SMLM for increasing signal-to-noise ratio and resolution and for averaging out stochastic variations in labeling.

1.2. DATA ALIGNMENT

Data alignment is a classical problem in signal and image processing. Here, one tries to match and register specific features of data obtained from different measurements. Often, the data is spatially transformed in 2/3D Cartesian space between acquisitions. The underlying transformations between the acquired data are typically translation, rotation, or scaling. The to-be aligned data exists in two categories: data on 2/3D regular grid (pixels or voxels) or unstructured set of points in \mathbb{R}^2 or \mathbb{R}^3 , so-called point clouds. In the following, we summarize various applications of data alignment based on this classification scheme, i.e. image alignment versus point cloud registration.

1.2.1. IMAGE ALIGNMENT APPLICATIONS

Digital images can be represented as two or three-dimensional arrays of finite size. Each element (pixel) of such an array holds an intensity value. Ideally, this intensity is proportional to the number of photons that is collected from the imaged scene at the image sensor. The need for alignment of multiple images, so-called image registration, can arise from motion in the imaged scene, e.g. cell movement, or from motion in the imaging system, e.g. stage drift. Plenty of techniques for image registration have been developed in the past 30 years [19]. An exhaustive summary of this field is beyond the scope of this thesis introduction. Instead, in the following we will briefly review the most important applications of image registration which are relevant and applicable to SMLM.

AVERAGING FOR DENOISING

Signal enhancement by averaging repeated measurements is a common technique in signal processing. For two-dimensional signals, i.e. images, this technique is mostly used for denoising. If the noise is a truly random and independent process (from the image) and the scene is fixed across different acquisitions, random fluctuations of the intensity around the actual pixel value will gradually even out as more data are averaged. In practice, however, these multiple noisy images are not perfectly matched, and one needs to align them first before averaging, as averaging without alignment results in blurring of the structures of interest. Figure 1.3a shows the result of averaging 100 synthetic images (left) which are affected by a zero mean Gaussian noise with (middle) and without alignment (right). It can be seen clearly in these figures that the noise has been suppressed to a large extent in both images, but that the edges are blurred in the image without alignment (right).

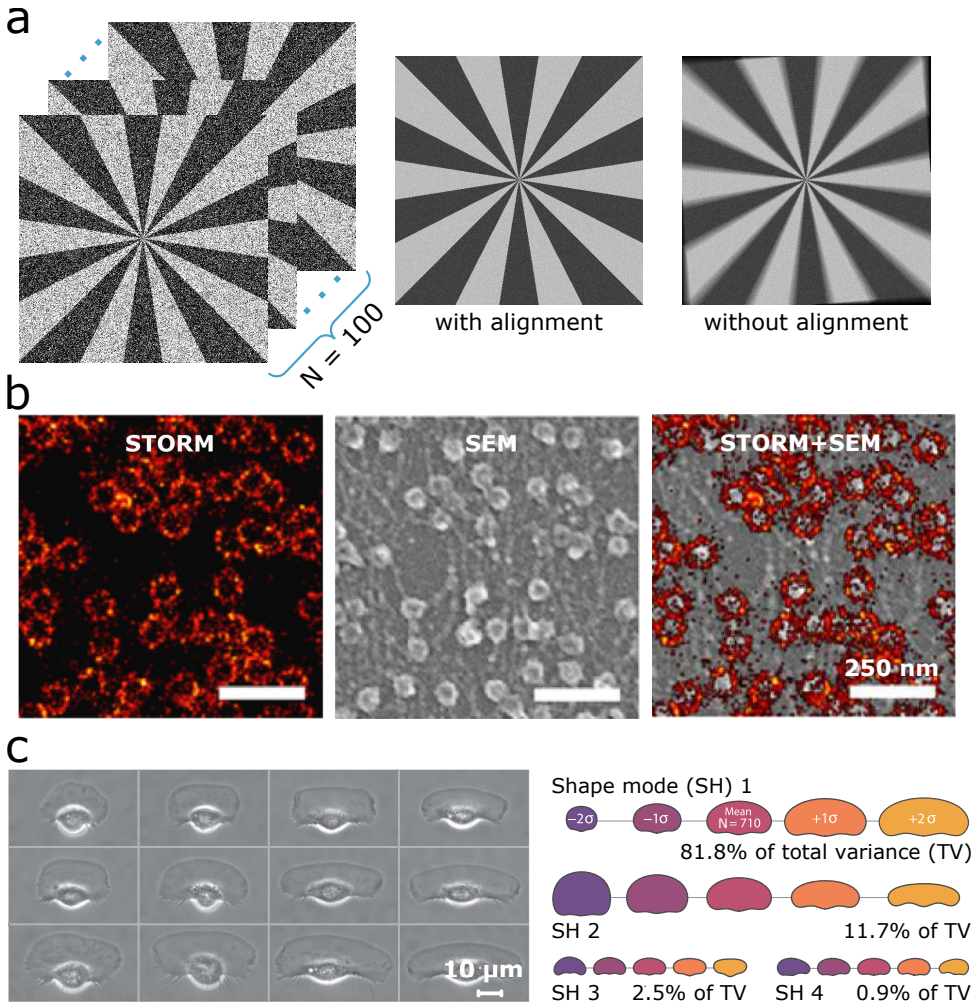


Figure 1.3: Applications of image registration. (a) Averaging for denoising. Hundreds of noisy Siemens star patterns (left) are averaged with (middle) and without (right) pre-alignment. (b) Multimodal image registration integrated the information of the STORM (left) and scanning electron microscope (SEM) (middle) images of nuclear pore complexes (NPCs) in a single CLEM reconstruction (right) [images adapted with permission from [20]]. (c) Shape analysis keratocytes. Variations of the keratocytes acquired using phase-contrast imaging is visible in differently aligned images (left). Once the images are aligned with each other, the population can be characterized by statistical shape analysis (right) [images adapted with permission from [21]].

MULTIMODAL IMAGE REGISTRATION

In many imaging applications, a single acquisition technique is not capable of capturing all the desired and useful information about the object of interest. Multimodal image acquisitions can provide information about different aspects of the object with the goal of information integration. This imaging approach is typically done sequentially. Therefore, there is a high chance of misalignment between the images captured with different

techniques.

For example, in medical imaging, multimodal image registration of computed tomography (CT), positron emission tomography (PET) and magnetic resonance imaging (MRI) images is a topic of considerable interest. Particularly useful image registration methods are variational approaches that optimize the mutual information between the distributions of intensities across the pixels. This is of value as images from different modalities can capture totally different properties of the object(s) of interest [19, 22].

Recently, correlative light-electron microscopy (CLEM), as a multi-modal imaging method, has been proposed as a tool to acquire subcellular images at different length scales and functionality [20]. Matching embedded physical fiducial markers which are detectable in both fluorescence and electron microscopy images is the most often used approach for correlating the two modalities [23]. Other approaches for this task include registration of manually spotted features (like corners) and automatic alignment of CLEM images [24]. The latter methods are mostly inspired by medical image registration techniques as previously discussed (Figure 1.3b).

ATLAS RECONSTRUCTION

Another purpose of image alignment can be to construct an average model or shape, a so-called template, representing the mean of a population of samples. In this context, samples are understood as different acquisitions of the same or similar structure. Applications of this technique range from building up atlases for anatomical structures of the body (such as the brain) in medical imaging to building dictionaries for cell structures and their variations in different environments in cell biology [21]. The statistical variations between the samples is also a topic of interest. One of the important challenges of this problem is how to construct the template such that it truly represents the whole population while at the same time it is not biased toward any of the individual samples (Figure 1.3c).

1.2.2. POINT CLOUD REGISTRATION APPLICATIONS

Point cloud data in \mathbb{R}^2 or \mathbb{R}^3 are acquired in different fields, such as remote sensing with light detection and ranging (LIDAR), gaming in which ranging devices like Kinect are used to scan bodies, and SMLM where fluorescent molecule positions are measured in 2D/3D space. Example applications of point cloud registration can thus be found in scene reconstruction, image feature matching and data fusion for SMLM.

SCENE RECONSTRUCTION AND MOSAICING

Microscope setups have a limited field of view (FOV), inversely proportional to the magnification of the objective lens. Especially high NA objective lenses, as used for super-resolution applications, have typically a high magnification. In many cases, imaging an area larger than the FOV is desired and, therefore, an image stitching or mosaicing approach is needed. This can be achieved if there is enough overlap between the tiles that make up the whole imaged area [25] (Figure 1.4a).

FEATURE (FIDUCIAL) MATCHING

One of the great features of fluorescence microscopy is the ability to perform multicolor imaging to study the interactions between different proteins in subcellular structures,

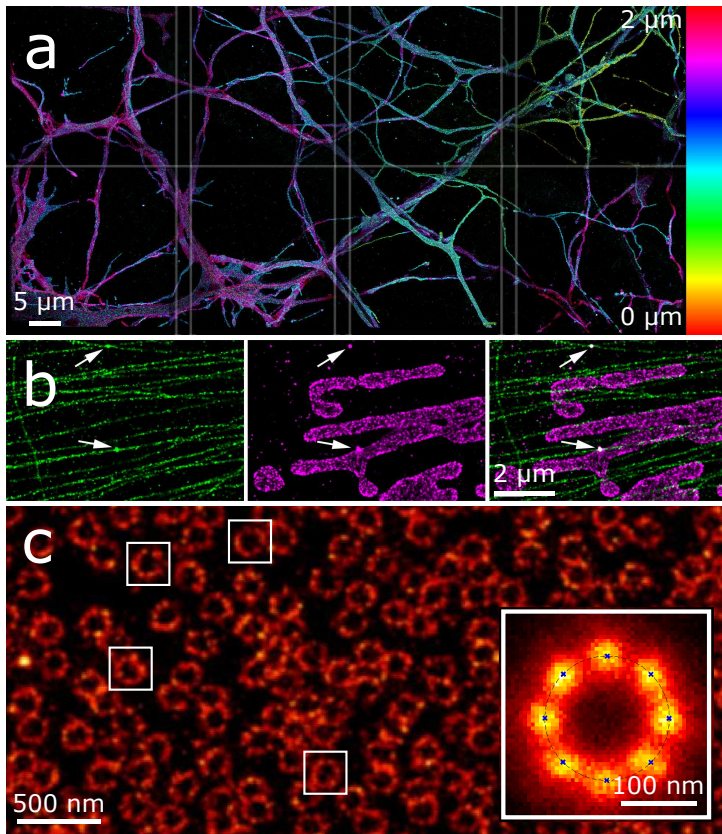


Figure 1.4: Applications of point cloud registration in SMLM. (a) A large field of view ($147\mu\text{m} \times 80\mu\text{m}$) image of hippocampal neurons reconstructed by stitching eight overlapping smaller images. The localizations are color-coded in z [images adapted with permission from [25]]. (b) Multicolor imaging of microtubules (green) and mitochondrial outer membrane protein (magenta). The two colors are registered using fiducial markers (white arrows) which are visible in both channels [images adapted with permission from [26]]. (c) Data fusion of ~ 400 NPCs acquired using STORM [images adapted with permission from [18]].

which are stained with fluorescent labels that differ in excitation and emission wavelength. The registration of the multicolor data for this application is mostly done by matching fiducial markers which are visible in both (or multiple) channels. If there is only a translation and rotation mismatch from one color acquisition to another, having only three fiducial markers would in principle suffice for a perfect alignment. In practice, nonrigid transformations and requirements on robustness of the procedure necessitate the use of multiple markers. The optimum transformation is usually defined with a least squares based minimum mismatch criterion [26] (Figure 1.4b).

PARTICLE FUSION

Particle fusion, also known as particle averaging or data fusion, tries to combine the information from multiple measurements of the same or similar structures (“particles”) in

a single reconstruction in order to fill-in missing information due to underlabeling and to increase signal to noise ratio (SNR) and resolution [18] (Figure 1.4c). One important feature of point cloud data in SMLM is that these point clouds are truly planar (in 2D) or volumetric (in 3D) compared to typical contour-like or surface point data from other acquisition techniques. Consequently, it is the local density of the points (localizations) that characterizes the data rather than the individual points. This is important because many of the point cloud processing methods from computer vision and image processing are based on estimating the surface normal of point data on a 2D manifold in 3D space, which is thus not applicable to localization data.

1.2.3. CLASSIFICATION OF POINT CLOUD REGISTRATION METHODS

Choosing the right method for point cloud registration depends very much on the type of the data. In this section, criteria are described for choosing an algorithm for the desired data alignment. Mathematically, a point cloud registration problem can be formulated as follows [19]. Given N sets of point clouds $(P_i)_{M_i \times d}$, labeled with an index $i \in \{1, \dots, N\}$, where $d = 2, 3$ is the spatial dimension and where M_i is the number of 2D or 3D points in the point cloud P_i , find the set of transformations $T(P_i, \theta_i)$, characterized by parameters θ_i , applied to the point clouds P_i , that minimizes a cost function (distance measure) $D(T(P_1, \theta_1), \dots, T(P_N, \theta_N))$ between the ensemble of the transformed sets:

$$(\theta_1^*, \dots, \theta_N^*) = \underset{\theta_i}{\operatorname{argmin}} D(T(P_1, \theta_1), \dots, T(P_N, \theta_N)). \quad (1.1)$$

Application of the estimated transformations on P_i aligns the different point clouds in a common reference frame, after which they can be averaged or fused. In SMLM, often the individual point clouds P_i are called particles, and the averaged or fused point cloud is referred to as the “superparticle”. In the following, we will discuss different aspects of this formalism.

RIGID VERSUS NONRIGID ALIGNMENT

Determining the relevant transformation type for the point clouds to be aligned is the first step in choosing a registration approach. In general, point clouds can undergo rigid or nonrigid transformations. Rigid transformations consist of translations, rotations and reflections. The common feature of these transformations is that they preserve the Euclidean distance between pairs of points. In 3D, this transformation can be described by the following matrix:

$$T = \begin{bmatrix} \mathbf{R} & \mathbf{t} \\ \mathbf{0} & \mathbf{1} \end{bmatrix}_{4 \times 4}, \quad (1.2)$$

where \mathbf{R} is a 3×3 rotation matrix and \mathbf{t} is a 3×1 translation vector. This matrix transforms a point $P = [x, y, z, 1]^T$ represented in homogeneous coordinates to Q using $Q = TP$. Any pairwise rigid registration problem minimizes a cost function with respect to the six degrees of freedom of the matrix T : three angles α_i , β_i and γ_i representing the 3D rotation and three displacement components x_i , y_i and z_i representing the translation. Therefore, $\theta_i = (\alpha_i, \beta_i, \gamma_i, x_i, y_i, z_i)$ for rigid alignment.

In contrast, nonrigid transformations generally do not have a specific definition and any deformation that is nonisometric is considered as nonrigid. Often used simple non-

rigid transformations are scaling and shearing transformations, which together with rotations and translations form the group of affine transformations. Except for these simple cases, nonrigid transformations cannot be described by a linear operator, i.e. a matrix.

PAIRWISE REGISTRATION VERSUS GROUPWISE REGISTRATION

Depending on the number of point clouds, registration algorithms fall into two classes: pairwise ($N = 2$ in Equation 1.1) or groupwise registration ($N > 2$). In pairwise registration, typically one of the point clouds is kept fixed and the other one is transformed for alignment. Therefore, Equation 1.1 simplifies to:

$$\theta^* = (\alpha^*, \beta^*, \gamma^*, x^*, y^*, z^*) = \underset{\theta}{\operatorname{argmin}} D(P_1, T P_1). \quad (1.3)$$

In groupwise registration, however, the final pose of the resulting superparticle depends on the way the alignment is realized. A straightforward method of groupwise registration is to divide the groupwise registration process into subsets of consecutive pairwise registration problems by keeping one particle fixed (pseudo-template) and then registering the rest to that template. This, however, may result in a problem known as template bias, which means that particular features of the point cloud that is chosen as the template are amplified in the resulting superparticle, while these features may not be representative for the collective of all point clouds. In order to solve this problem, reference-free alignment methods have been proposed in the literature which treat all point clouds equally to avoid any bias toward a specific one [27]. Another challenge of groupwise registration problems is the global offset problem. A global angular or translational transformation can be applied to the absolute pose of all sets without changing the quality of the final fused set due to the lack of a universal reference frame.

POINT CORRESPONDENCE

When two point clouds contain the same points only transformed with respect to the other, as in the alignment of fiducial markers, one often first establishes point correspondences and only then performs the alignment. Depending on the target cost function, most of the same-size point cloud alignment problems have a closed form solution. In contrast, finding correspondences in variable size point cloud registration problems is typically not possible as the number of possible assignments is very large. In SMLM, this correspondence cannot be made at all as underlabeling results in incomplete structures which are missing labels at up to 50-70% of their binding sites. Moreover, depending on the blinking statistics, the number of points (localizations) per binding site can be different within one point cloud (particle). In such problems, soft assignments where the point to point assignment is not binary but weighted (for example according to a probability distribution) can be used [28]. Alternatively, methods have been developed which consider the local density of the points in each cloud instead of the individual points [29]. While these density-based registrations are superior in terms of robustness with respect to noise and outliers, they create a new problem of density estimation.

ADDITIONAL INFORMATION AND PRIOR KNOWLEDGE

In many applications, points in Cartesian coordinate are not the only data that are acquired. In SMLM for example, every localization event not only comprises the estimated

coordinates, but usually comes with the estimates of the localization uncertainties in x , y (and z for 3D localization point clouds), signal photon count, frame number and background photon count. Color channel information is also available in multicolor experiments. Incorporating these extra information in the registration process can be useful or even necessary. For example, one desired feature for particle fusion is the use of localization uncertainties as they give proper weight to more precisely localized molecules compared to those with low localization precision.

In addition to the mentioned local information, there are other global features which are also of great importance to be incorporated into the registration pipeline. By global, we refer to the features that are built upon subsets of data points in a point cloud. This includes information about the symmetry of the point cloud, whether the points lie on a known manifold such as a sphere or cylinder, and any other prior knowledge which helps the optimization algorithm to converge faster and more robustly. Utilizing such extra information should be adapted properly to avoid any undesired bias in the resulting superparticle.

1.3. PARTICLE FUSION IN SMLM

SMLM data has certain features that make groupwise point cloud registration (or particle fusion in SMLM terminology) more complicated compared to point cloud data acquired in other applications. A key problem in SMLM is the problem of incomplete data. Complete labeling of the structure of interest is almost impossible due to low binding affinity of fluorescent labels. The degree of labeling (DOL) is typically on the order of 30-50%, i.e. less than half of the potential binding sites get labeled. A second complication is that a variable number of localizations is recorded from each labeled site due to stochastic variations of the on/off kinetics. In addition, the spread of localizations around the labeled site is distributed depending on the actual photon count of the localizations. These stochastic variations arise from the binding and/or switching kinetics of the fluorescent labels, and from the statistical variations in the number of recorded photons from a single emitter. Moreover, false positive localizations, background and residual drift can deteriorate the quality of the particles significantly. Finally, in 3D, the anisotropy in the localization uncertainty due to the relatively poor performance of localization in the axial direction results in an elongation of the distribution of localizations in the axial direction.

The existing approaches for particle fusion of SMLM data can be broken down into three categories: template-based approaches, methods that are borrowed from (cryo-) electron microscopy (cryo-EM) and pyramid registration. In the following, we provide an overview of the prior art in the scientific literature within these categories and describe their pros and cons.

1.3.1. TEMPLATE-BASED PARTICLE FUSION

Researchers have made use of various high-resolution imaging techniques like EM over the past few decades to study subcellular structures with resolutions down to a few Angstroms [32]. This means that accurate models are available in advance for some structures of interest for SMLM particle fusion. In several studies, these references are

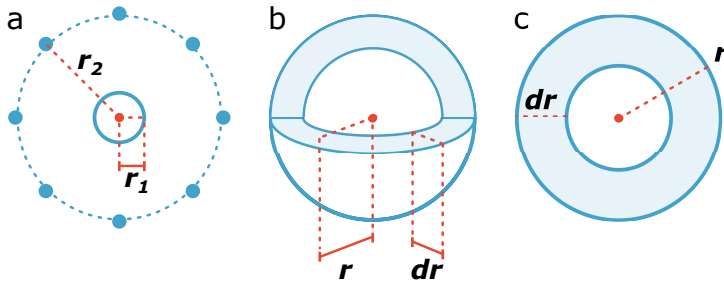


Figure 1.5: Example templates used in SMLM for particle fusion. (a) Simple (solid) and eight-fold symmetric (dotted) with radius r_1 and r_2 , respectively, as a model for fusing NPC and WGA particles [18]. (b) Monte-Carlo-based virus (MCV) model for particle fusion of STORM viral proteins [30]. Sphere radius r and its thickness dr are the template parameters. (c) 2D projections of the endocytic sites are fitted to an annulus with radius r and thickness of dr to center the disc-like particles [31].

used as a template to which the acquired data are fitted.

Löschberger et al. [18], in 2012, used an eight-fold symmetric ring and a simple ring as templates to fuse localizations of labeled gp210 proteins in the nuclear pore complex (NPC) and the wheat germ agglutinin (WGA) in its center, respectively (Figure 1.5a). In this study, the optimum rotation angles and translation vectors were found by minimizing the sum of the distances of localizations in each segmented particle to the model points. Several other studies showed the power of template-based approach following this successful work. Laine et al. [30] used a thick hollow sphere as a model to fuse STORM localizations of the tegument proteins VP16, VP1/2 and pUL37, and envelope protein gD particles ($N = 50 - 100$) in the study of the Herpes simplex virus type-1 (Figure 1.5b). Gray et al. [33] combined template-based fitting and image cross correlation for visualization of viral structures. In their workflow the user needs to manually select a subset of viral images as seeds for the alignment of the rest of the images. Recently, Mund et al. [31] used an annulus as a geometric model to align SMLM images of endocytic proteins imaged using 2D STORM (Figure 1.5c). This, however, was used only for determining the radial distribution of localization data and no other structural information was inferred from the data.

The advantage of template-based particle fusion is its favorable computational complexity, which is linearly proportional to the number of particles. This is only possible when an in-advance accurate and proper model exists. Template-based particle fusion algorithms, however, are susceptible to the template bias problem described previously, implying that features of the template are reproduced in the final superparticle even when the model underlying the template is completely wrong. Figure 1.6 shows the fusion of the NPC data as described in [18] using a correct eight-fold symmetric template and a wrong nine-fold symmetric template, respectively. As it can be seen, the data fits quite well to both models. This shows how imposing strong assumptions via a template can result in a bias.

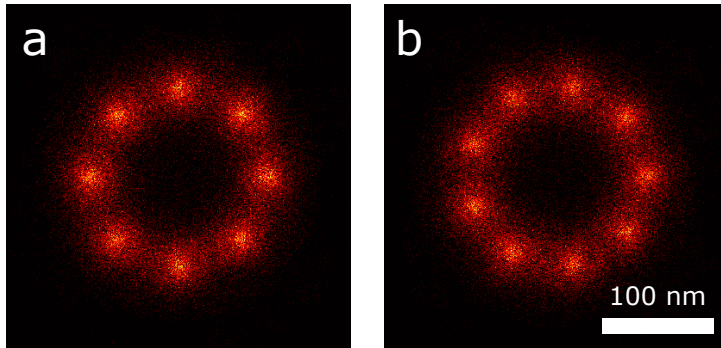


Figure 1.6: Template-bias problem. Fusion of NPC data [18] using the correct eight-fold (a) and wrong nine-fold (b) symmetric ring templates.

1.3.2. EM INSPIRED PARTICLE FUSION FOR SMLM

Another class of particle fusion in SMLM consists of the methods which adapt techniques from single particle analysis (SPA) in EM [34]. SPA tries to classify, align and average typically thousands of very low SNR 2D projections as the first step in the 3D reconstruction of the structure. The acquired data in EM comes in the form of pixelated images. Therefore, in order to be able to use these routines for localization data in SMLM, one needs to first render the 2D coordinates as gray scale pixelated images. This is mostly achieved by rendering each localization event by a 2D Gaussian function with a width equal to the corresponding localization uncertainty and subsequently displaying the continuous sum of Gaussians on a discrete pixel grid [14].

The earliest work on utilizing EM routines for performing SMLM particle fusion traces is that of Szyzborska et al. [35], in which the commercially available software package iMagic [36] was used for the alignment of different subunits of the NPC, the so-called nucleoporins (NUPs). With this approach the average radius of different NUPs was measured, providing clues on the spatial arrangement of the different NUPs in the NPC. However, in any of their reconstructions, the eight-fold symmetry of the NPCs was not resolved (Figure 1.7a). In 2016, Dai et al. [13] averaged DNA-origami nanostructures made on lattice patterns with a minimum grid size of 5 nm and imaged using PAINT by the application of the EMAN.2 [37] software package (Figure 1.7b) which is an open source image processing toolbox developed for SPA in cryo-EM. Two other studies have pushed this further by generating 3D reconstructions of macromolecular structures using 2D SMLM projections. Salas et al. [38] used again iMagic for SPA of 3D DNA-origami rods and tetrahedrons imaged with PAINT (Figure 1.7c) and later, Sieben et al. [39] took a similar approach for making 3D volume reconstructions of the human centriole (Cep164, Cep57, Cep152, Cep63) and of the bacteriophage T4 using another EM software package called Scipion (Figure 1.7d). In addition to the mentioned works which directly used available EM software, there are also other attempts for 2D/3D particle fusion [41–43] in which the researchers used customized EM routines for this purpose.

The main drawback of these approaches is the central premise of cryo-EM based

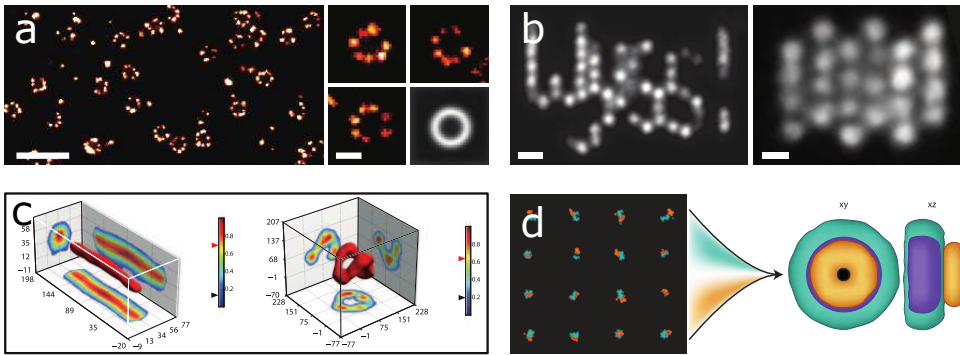


Figure 1.7: EM inspired particle fusion for SMLM. (a) Fusion of 4171 Nup133 particles using the iMagic software package. Scale bars are 500 nm and 100 nm, respectively. [images adapted with permission from [35]] (b) Class averages of “Wyss!” and lattice patterned DNA-Origami nanostructures produced using the EMAN.2 software solution. [images adapted with permission from [13]]. 3D reconstructions of a rod, tetrahedron [38] (c) and human centriole [39] (d) using SPA-based subroutines from EM32. [images adapted with permission from [38, 40]]

SPA: All particles are represented by 2D pixelated images and are first classified according to the most likely projection of the underlying 3D structure. Then, averaging within orientation classes is applied and a 3D reconstruction is made based on the estimated orientation. All these key elements are not relevant or even directly applicable to SMLM datasets. First, the data need not necessarily be described in terms of 2D pixelated images. In particular for 3D SLMLM data this ignores the volumetric information that is already available in the individual point clouds. Second, the image data does not come in the form of projections of a 3D structure on a 2D plane. Last but not least, these approaches completely ignore the difference in image formation models, noise sources and most importantly underlabeling.

1.3.3. PYRAMID PARTICLE FUSION

Different from the methods discussed so far, Broeken et al. [44] proposed a new coordinate-based cost function for pairwise registration of SMLM particles and a pyramid setup for template-free alignment of multiple particles. In this study, the Bhattacharya cost function [45] from statistical pattern recognition was adapted as a metric for optimizing the transformation parameters. This cost function minimizes the sum of all localization-to-localization mismatches between the two particles, in such a way that the weight of each couple of localizations in the sum decreases exponentially with the distance after the transformation. In this way, outlier localizations are ignored in the minimization. Another feature of this cost function is that it can properly consider the heterogeneity and the anisotropy of 2D/3D localization uncertainties by using these uncertainties in the exponential weighting of the localization-to-localization distances. This cost function is defined as:

$$D = \sum_{i=1}^{K_t} \sum_{j=1}^{K_m} \exp\left(-(\vec{x}_{t,i} - M(\vec{x}_{m,j}))^T (\Sigma_{t,i} + R\Sigma_{m,j}R^T)^{-1} (\vec{x}_{t,i} - M(\vec{x}_{m,j}))\right), \quad (1.4)$$

in which $\vec{x}_t, \vec{x}_m \in R^n$ are the localization coordinates of the two particles (t and m) with K_t and K_m localizations, $\Sigma_t, \Sigma_m \in R^{n \times n}$ the corresponding uncertainties of the form $\Sigma = \text{diag}(\sigma_1^2, \dots, \sigma_n^2)$. Here, the particle \vec{x}_m is transformed according to the function $M(\vec{x}) = R\vec{x} + \vec{s}$ that applies rotation (R) and translation (\vec{s}) to position \vec{x} .

Unfortunately, the double summation in this cost function makes it computationally expensive ($O(K_t K_m)$) for particles with large numbers of localizations. For example, in PAINT this can be ~ 3000 for a particle with several tens of binding sites as each binding site is imaged multiple times. Moreover, this cost function is only suitable for pairwise registration. In this work, these two problems were overcome by choosing a template as one of the inputs to the cost function, which in this case was the eight-fold NPC structure with only eight points. In this way, ~ 8000 images of localized Nup133 proteins in the NPC of HeLa cells were fused [44]. It was further suggested (but not implemented) to make the approach template-free by pairwise registration of all the initial particles to form a second layer of pairwise fused particles, and subsequently repeating the process until only a single superparticle remains (Figure 1.8a). The computational complexity of such a pyramid registration scheme is quadratic in the number of particles, which together with the complexity of Bhattacharya cost function is a roadblock for a practical implementation, despite the great promise of being template-free.

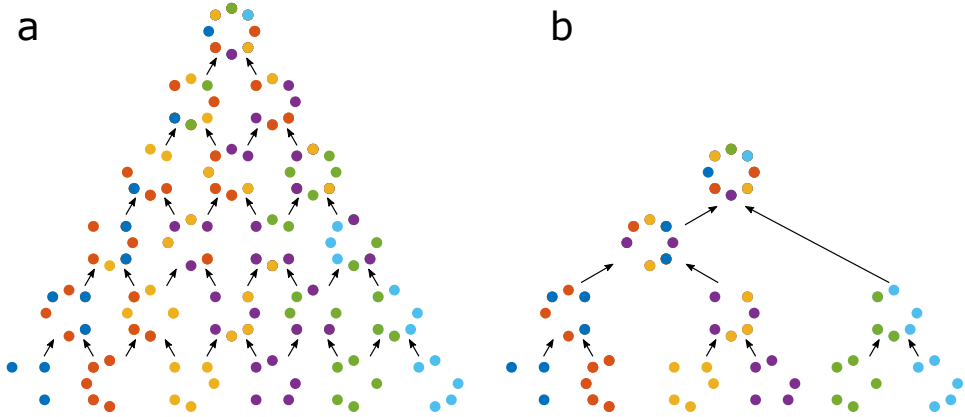


Figure 1.8: Schematic of pyramid registration. (a) Full pyramid as suggested in [44]. (b) Simplified pyramid.

1.3.4. ACCELERATED PYRAMID PARTICLE FUSION

Our first attempt to realize a template-free particle fusion method was built upon the pyramid approach as suggested in [44]. The idea was to optimize the pyramid approach together with an acceleration for the cost function optimization. First, the pyramid structure was simplified by registering each particle to only one other particle in each layer (Figure 1.8b). This resulted in a better scaling of the computational complexity with the number of particles, namely as $O(\log(N))$. Furthermore, the particles were shuffled randomly in each layer in order to prevent biases. Then, the search space of the Bhattacharya cost function was reduced by pairwise pre-alignment of all particles using a fast Gaussian mixture model (GMM) registration approach [46]. In this method

all localization data are given a constant uncertainty equal to the ensemble mean value. Multiple initializations of this GMM approach provided several candidate rigid transformation parameters out of which the best was chosen by evaluating the Bhattacharya cost function. Figure 1.9 shows the result of fusing three experimental datasets and three corresponding simulated datasets of DNA-origami nano-structures at different labeling densities, forming the letters “MPI”, and “LMU” and a grid structure with 20 nm binding site spacing. The experimental datasets were measured, and the simulated datasets were modeled, using the PAINT technique. The experimental datasets consisted of 800 particles, the simulated datasets of 256 particles.

It was found that the accelerated pyramid particle fusion resulted in a good quality superparticle provided that the quality of the initial particles was sufficiently good (Figure 1.9a-d), i.e. for a density of labeling (DOL) of about 70% or higher. Alas, it turned out to have shortcomings that made the method less applicable for realistic experimental conditions, which typically entail a lower labeling density (Figure 1.9e-f). First, features of the superparticle at the top of the pyramid can be traced back to one pair of particles in the first layer. If this pair is of low quality, then the whole pyramid will be built upon this poor-quality registered pair of particles. Any registration error at these lower layers will be propagated to upper layers and since there is no feedback loop for correction, the error can even be amplified. Second, at the first layer of this accelerated pyramid approach, we only performed $N/2$ pairwise registrations out of $N(N-1)/2$ available pairs. This means that a large amount of information is discarded which could be very useful for improving robustness at poor imaging conditions.

1.4. RESEARCH QUESTIONS AND THESIS OUTLINE

The goal of this thesis is to overcome the drawbacks of the existing methods for particle fusion in SMLM. Specifically, the new method must address several key issues that are particular to SMLM data.

- It is desirable that the new approach dedicated to SMLM properly takes into account localization data at the highest precision, i.e. as point clouds rather than rendered images on a pixel or voxel grid.
- The fusion pipeline should also incorporate the corresponding, possibly anisotropic, localization uncertainties.
- Ideally, it should not need any prior knowledge of the underlying structure, but optionally be able to exploit geometrical characteristics like symmetry.
- It is essential that the algorithm can handle both 2D and 3D data.
- Considering the limited quality of typical experimental SMLM data arising from e.g. a low labeling density, the method should exploit the maximum information that is available from the data to compensate for the missing information.
- Each SMLM modality, like STORM and PAINT, exhibits different statistical properties in the resulting localization data. The envisioned particle fusion method should properly handle these differences or not be sensitive to them.

In [chapter 2](#), we present a solution for template-free fusion of 2D SMLM particles and evaluate its performance on simulated and experimental datasets generated and acquired using STORM and PAINT techniques, respectively. Next in [chapter 3](#), we extend our pipeline to 3D and show how particle fusion can enable structural analysis of macromolecular complexes such as the NPC. Finally, we outline a summary of the conclusions and both a short-term and long-term outlook to particle fusion in SMLM in [chapter 4](#).

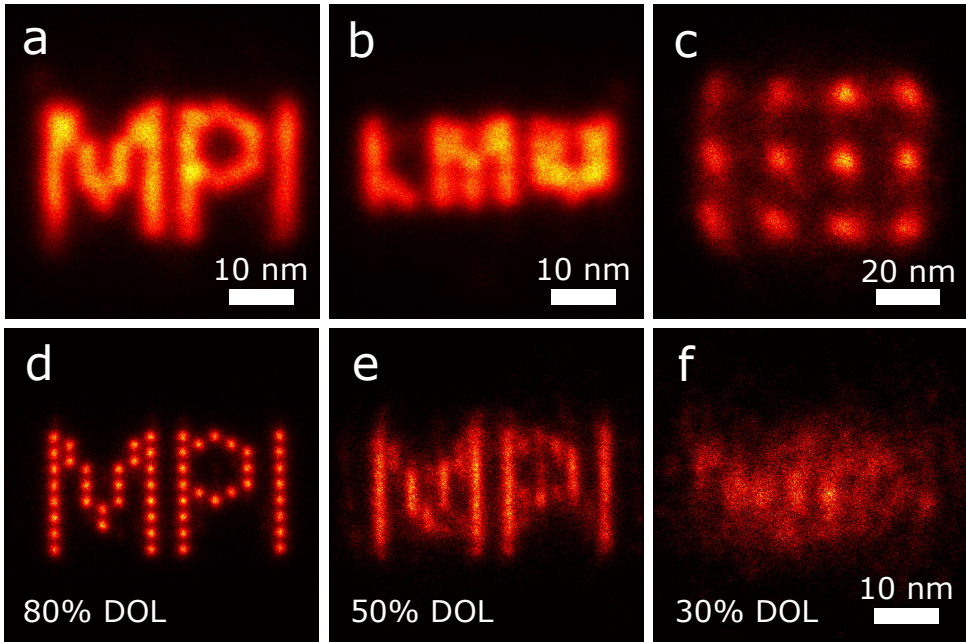


Figure 1.9: Accelerated pyramid registration of experimental (a-c) and simulated (d-f) DNA-Origami nanostructures imaged using PAINT. [Data courtesy of Ralf Jungmann]

REFERENCES

- [1] Bo Huang, Mark Bates, and Xiaowei Zhuang. Super-resolution fluorescence microscopy. *Annual review of biochemistry*, 78, 2009.
- [2] Lothar Schermelleh, Rainer Heintzmann, and Heinrich Leonhardt. A guide to super-resolution fluorescence microscopy. *The Journal of Cell Biology*, 190(2), 07 2010.
- [3] Teresa Klein, Sven Proppert, and Markus Sauer. Eight years of single-molecule localization microscopy. *Histochemistry and Cell Biology*, 141(6), 2014.
- [4] Angélique Jimenez, Karoline Friedl, and Christophe Leterrier. About samples, giving examples: Optimized single molecule localization microscopy. *Methods*, 2019.

- [5] Eric Betzig, George H. Patterson, Rachid Sougrat, O. Wolf Lindwasser, Scott Olenych, Juan S. Bonifacino, Michael W. Davidson, Jennifer Lippincott-Schwartz, and Harald F. Hess. Imaging intracellular fluorescent proteins at nanometer resolution. *Science*, 313(5793), 2006.
- [6] Michael J. Rust, Mark Bates, and Xiaowei Zhuang. Sub-diffraction-limit imaging by stochastic optical reconstruction microscopy (storm). *Nature Methods*, 3(10), 2006.
- [7] Alexey Sharonov and Robin M. Hochstrasser. Wide-field subdiffraction imaging by accumulated binding of diffusing probes. *Proceedings of the National Academy of Sciences*, 103(50), 2006.
- [8] Robert P. J. Nieuwenhuizen, Mark Bates, Anna Szymborska, Keith A. Lidke, Bernd Rieger, and Sjoerd Stallinga. Quantitative localization microscopy: Effects of photophysics and labeling stoichiometry. *PLOS ONE*, 10(5), 05 2015.
- [9] B. Rieger, R. Nieuwenhuizen, and S. Stallinga. Image processing and analysis for single-molecule localization microscopy: Computation for nanoscale imaging. *IEEE Signal Processing Magazine*, 32(1), 2015.
- [10] Carlos S. Smith, Sjoerd Stallinga, Keith A. Lidke, Bernd Rieger, and David Grunwald. Probability-based particle detection that enables threshold-free and robust in vivo single-molecule tracking. *Molecular Biology of the Cell*, 26(22), 2015.
- [11] Daniel Sage, Thanh-An Pham, Hazen Babcock, Tomas Lukes, Thomas Pengo, Jerry Chao, Ramraj Velmurugan, Alex Herbert, Anurag Agrawal, Silvia Colabrese, Ann Wheeler, Anna Archetti, Bernd Rieger, Raimund Ober, Guy M. Hagen, Jean-Baptiste Sibarita, Jonas Ries, Ricardo Henriques, Michael Unser, and Seamus Holden. Super-resolution fight club: assessment of 2d and 3d single-molecule localization microscopy software. *Nature Methods*, 16(5), 2019.
- [12] Martin Ovesný, Pavel Křížek, Josef Borkovec, Zdeněk Švindrych, and Guy M Hagen. Thunderstorm: a comprehensive imagej plug-in for palm and storm data analysis and super-resolution imaging. *Bioinformatics*, 30(16):2389–2390, 2014.
- [13] Mingjie Dai, Ralf Jungmann, and Peng Yin. Optical imaging of individual biomolecules in densely packed clusters. *Nature Nanotechnology*, 11(9), 2016.
- [14] A. Cambi and D.S. Lidke. *Cell Membrane Nanodomains: From Biochemistry to Nanoscopy*. CRC Press, 2014.
- [15] Robert P. J. Nieuwenhuizen, Keith A. Lidke, Mark Bates, Daniela Leyton Puig, David Grünwald, Sjoerd Stallinga, and Bernd Rieger. Measuring image resolution in optical nanoscopy. *Nature methods*, 10(6), 2013.
- [16] Patrick Rubin-Delanchy, Garth L. Burn, Juliette Griffié, David J. Williamson, Nicholas A. Heard, Andrew P. Cope, and Dylan M. Owen. Bayesian cluster identification in single-molecule localization microscopy data. *Nature Methods*, 12(11), 2015.

- [17] Jervis Vermal Thevathasan, Maurice Kahnwald, Konstanty Cieliski, Philipp Hoess, Sudheer Kumar Peneti, Manuel Reitberger, Daniel Heid, Krishna Chaitanya Kasuba, Sarah Janice Hoerner, Yiming Li, Yu-Le Wu, Markus Mund, Ulf Matti, Pedro Matos Pereira, Ricardo Henriques, Bianca Nijmeijer, Moritz Kueblbeck, Vilma Jimenez Sabinina, Jan Ellenberg, and Jonas Ries. Nuclear pores as versatile reference standards for quantitative superresolution microscopy. *Nature Methods*, 16(10), 2019.
- [18] Anna Löscherger, Sebastian van de Linde, Marie-Christine Dabauvalle, Bernd Rieger, Mike Heilemann, Georg Krohne, and Markus Sauer. Super-resolution imaging visualizes the eightfold symmetry of gp210 proteins around the nuclear pore complex and resolves the central channel with nanometer resolution. *Journal of Cell Science*, 125(3), 2012.
- [19] J. Modersitzki and Oxford University Press. *Numerical Methods for Image Registration*. OUP Oxford, 2004.
- [20] Anna Löscherger, Christian Franke, Georg Krohne, Sebastian van de Linde, and Markus Sauer. Correlative super-resolution fluorescence and electron microscopy of the nuclear pore complex with molecular resolution. *Journal of Cell Science*, 127(20), 2014.
- [21] Kinneret Keren, Zachary Pincus, Greg M. Allen, Erin L. Barnhart, Gerard Marriott, Alex Mogilner, and Julie A. Theriot. Mechanism of shape determination in motile cells. *Nature*, 453(7194), 2008.
- [22] Francisco P. M. Oliveira and João Manuel R. S. Tavares. Medical image registration: a review. *Computer Methods in Biomechanics and Biomedical Engineering*, 17(2), 2014.
- [23] Benjamin G. Kopek, Gleb Shtengel, C. Shan Xu, David A. Clayton, and Harald F. Hess. Correlative 3d superresolution fluorescence and electron microscopy reveal the relationship of mitochondrial nucleoids to membranes. *Proceedings of the National Academy of Sciences*, 109(16), 2012.
- [24] Isabell Begemann and Milos Galic. Correlative light electron microscopy: Connecting synaptic structure and function. *Frontiers in Synaptic Neuroscience*, 8(28), 2016.
- [25] Melike Lakadamyali, Hazen Babcock, Mark Bates, Xiaowei Zhuang, and Jeff Lichtman. 3d multicolor super-resolution imaging offers improved accuracy in neuron tracing. *PLOS ONE*, 7(1), 2012.
- [26] Johnny Tam, Guillaume Alan Cordier, Joseph Steven Borbely, Ángel Sandoval Álvarez, and Melike Lakadamyali. Cross-talk-free multi-color storm imaging using a single fluorophore. *PLOS ONE*, 9(7), 2014.
- [27] Gary KL Tam, Zhi-Quan Cheng, Yu-Kun Lai, Frank C Langbein, Yonghuai Liu, David Marshall, Ralph R Martin, Xian-Fang Sun, and Paul L Rosin. Registration of 3d point clouds and meshes: a survey from rigid to nonrigid. *IEEE transactions on visualization and computer graphics*, 19(7), 2012.

- [28] Steven Gold, Chien Ping Lu, Anand Rangarajan, Suguna Pappu, and Eric Mjolsness. New algorithms for 2d and 3d point matching: pose estimation and correspondence. In *Proceedings of the 7th International Conference on Neural Information Processing Systems*. MIT Press, 1994.
- [29] Yanghai Tsing and Takeo Kanade. A correlation-based approach to robust point set registration. In *European conference on computer vision*, pages 558–569. Springer, 2004.
- [30] Romain F. Laine, Anna Albecka, Sebastian van de Linde, Eric J. Rees, Colin M. Crump, and Clemens F. Kaminski. Structural analysis of herpes simplex virus by optical super-resolution imaging. *Nature Communications*, 6(1), 2015.
- [31] Markus Mund, Johannes Albertus van der Beek, Joran Deschamps, Serge Dmitrieff, Philipp Hoess, Jooske Louise Monster, Andrea Picco, François Nédélec, Marko Kaksonen, and Jonas Ries. Systematic nanoscale analysis of endocytosis links efficient vesicle formation to patterned actin nucleation. *Cell*, 174(4), 2018.
- [32] Xiao Fan, Jia Wang, Xing Zhang, Zi Yang, Jin-Can Zhang, Zhao Lingyun, Hai-Lin Peng, Jianlin Lei, and Hong-Wei Wang. Single particle cryo-em reconstruction of 52 kda streptavidin at 3.2 angstrom resolution. *Nature Communications*, 10, 12 2019.
- [33] Robert D. M. Gray, Corina Beerli, Pedro Matos Pereira, Kathrin Maria Scherer, Jerzy Samolej, Christopher Karl Ernst Bleck, Jason Mercer, and Ricardo Henriques. Virusmapper: open-source nanoscale mapping of viral architecture through super-resolution microscopy. *Scientific Reports*, 6, 2016.
- [34] Joachim Frank. *Three-dimensional electron microscopy of macromolecular assemblies: visualization of biological molecules in their native state*. Oxford University Press, 2006.
- [35] Anna Szymborska, Alex de Marco, Nathalie Daigle, Volker C. Cordes, John A. G. Briggs, and Jan Ellenberg. Nuclear pore scaffold structure analyzed by super-resolution microscopy and particle averaging. *Science*, 341(6146), 2013.
- [36] Marin van Heel and Wilko Keegstra. Imagic: A fast, flexible and friendly image analysis software system. *Ultramicroscopy*, 7(2), 1981.
- [37] Guang Tang, Liwei Peng, Philip R. Baldwin, Deepinder S. Mann, Wen Jiang, Ian Rees, and Steven J. Ludtke. Eman2: An extensible image processing suite for electron microscopy. *Journal of Structural Biology*, 157(1), 2007.
- [38] Desirée Salas, Antoine Le Gall, Jean-Bernard Fiche, Alessandro Valeri, Yonggang Ke, Patrick Bron, Gaetan Bellot, and Marcelo Nollmann. Angular reconstitution-based 3d reconstructions of nanomolecular structures from superresolution light-microscopy images. *Proceedings of the National Academy of Sciences*, 114(35), 2017.
- [39] Christian Sieben, Niccolò Banterle, Kyle M. Douglass, Pierre Gönczy, and Suliana Manley. Multicolor single-particle reconstruction of protein complexes. *Nature Methods*, 15(10), 2018.

- [40] Mark Bates. Single-particle analysis for fluorescence nanoscopy. *Nature Methods*, 15(10):771–772, 2018.
- [41] Xiaoyu Shi, Galo Garcia, Julie C. Van De Weghe, Ryan McGorty, Gregory J. Pazour, Dan Doherty, Bo Huang, and Jeremy F. Reiter. Super-resolution microscopy reveals that disruption of ciliary transition-zone architecture causes joubert syndrome. *Nature Cell Biology*, 19(10), 2017.
- [42] Joerg Schnitzbauer, Yina Wang, Shijie Zhao, Matthew Bakalar, Tulip Nuwal, Baohui Chen, and Bo Huang. Correlation analysis framework for localization-based super-resolution microscopy. *Proceedings of the National Academy of Sciences*, 115(13), 2018.
- [43] X. Shi, 3rd Garcia, G., Y. Wang, J. F. Reiter, and B. Huang. Deformed alignment of super-resolution images for semi-flexible structures. *PLoS One*, 14(3), 2019.
- [44] Jordi Broeken, Hannah Johnson, Diane S. Lidke, Sheng Liu, Robert P. J. Nieuwenhuizen, Sjoerd Stallinga, Keith A. Lidke, and Bernd Rieger. Resolution improvement by 3d particle averaging in localization microscopy. *Methods and Applications in Fluorescence*, 3(1), 2015.
- [45] Sung-Hyuk Cha. Comprehensive survey on distance/similarity measures between probability density functions. *City*, 1(2):1, 2007.
- [46] B. Jian and B. C. Vemuri. Robust point set registration using gaussian mixture models. *IEEE Transactions on Pattern Analysis and Machine Intelligence*, 33(8), 2011.

2

TEMPLATE-FREE 2D PARTICLE FUSION IN LOCALIZATION MICROSCOPY

Current methods for fusing multiple localization microscopy images of a single underlying structure can improve signal-to-noise ratio and resolution, but suffer from template bias or sensitivity to registration errors. We present a template-free particle fusion based on an all-to-all registration, which provides robustness against individual mis-registrations and underlabeling. We achieve 3.3 nm FRC image resolution from fusing 383 DNA-origami nanostructures with 80% labeling density, to 5.0 nm for 30% labelling.

2.1. INTRODUCTION

SINGLE molecule localization microscopy (SMLM) provides the ability to image well below the diffraction limit [2]. The resolution in the final reconstructed image is limited by the localization uncertainty and the emitter density down to about 20 nm [3]. The fusion of multiple acquisitions into one hyper-resolved reconstruction can mitigate these limiting factors when many identical copies of the same structure (particle) can be imaged [4, 5]. This final reconstruction has effectively many more localizations than each individual SMLM image, which results in a better signal-to-noise-ratio (SNR) and hence effectively a better resolution. This approach is similar to single particle analysis (SPA) in cryo-electron microscopy (cryo-EM) [6, 7].

A few studies have applied SPA to SMLM despite fundamental differences in image formation [5, 8–11]. Most importantly, fluorescent labeling is often incomplete and only 30-70% density of labeling (DOL) is typically achieved [12]. Statistical variations in localization uncertainty, false positive localizations [13, 14] and repeated localizations of the same fluorophore are additional complications compared to cryo-EM.

Methods for data fusion for SMLM are known that use a template [4, 5, 9, 15] for alignment, which have the risk of generating a structure that is biased towards this template [16]. A template-free pyramid registration approach for SMLM datasets [15] registers N particles pairwise into $N - 1$ reconstructions, a second set of pairwise registrations reduces this to $N - 2$ reconstructions, etc. This method, as any iterative method of combining pair-wise registrations, suffers from a large sensitivity to registration errors in the bottom layer of the pyramid, which propagate into subsequent layers of the procedure.

Here, we present a particle fusion approach which assumes no prior knowledge of the structure to be imaged (template-free), that works directly on the localization data (including the uncertainties), and that is robust against registration errors and underlabeling. The key idea is to use an all-to-all registration procedure, in which each particle is registered to all the others, implying $N(N - 1)/2$ pair registrations for N given particles. This generates the maximum information that can be extracted from aligning N particles.

Each pair registration results in an estimate of the relative orientation and position of the two particles. What is needed, however, are the N absolute orientations and positions of all particles. For this step we utilize a technique from the field of computer vision in which camera position and orientation are estimated from a sequence of images taken from a scene (“structure from motion”) [17]. Lie-algebraic representations of the transformation parameters (rotations and translations) are averaged in this technique, providing robustness to outlier pair registrations (see for details [subsubsection a](#)). In this way, we make optimal use of the very large redundancy in the $N(N - 1)/2$ pair registration parameters, and overcome the main flaw of any iterative registration method. A critical improvement over [17] is the use of a sparsity promoting L_1 norm (see [Methods section](#)).

The performance is further improved by making use of self-consistency. The found N absolute transformation parameters are used to retrodict the $N(N - 1)/2$ relative transformation parameters, which can then be compared to the values found from the all-to-all registration. Registration pairs with a deviation in these relative transformation parameters that is too high (defined by a suitable threshold) are discarded for a second

round of Lie-algebraic averaging. This removal of outlier registration pairs results in a reconstruction that is used in a final step as a data-driven model to bootstrap the registration process. This last step is especially effective for low DOL.

The major drawback of all-to-all registration is the computational cost, which scales as N^2 instead of as N for a template-based registration. Therefore, we have devised a computationally efficient implementation of the registration algorithm. Starting point is the Bhattacharya cost function [15]:

$$D = \sum_{i=1}^{K_t} \sum_{j=1}^{K_m} \exp\left(-(\vec{x}_{t,i} - M(\vec{x}_{m,j}))^T (\Sigma_{t,i} + R\Sigma_{m,j}R^T)^{-1} (\vec{x}_{t,i} - M(\vec{x}_{m,j}))\right), \quad (2.1)$$

where the two particles t and m are represented by K_t and K_m localizations, with $\vec{x}_t, \vec{x}_m \in R^n$ the localization coordinates of the two particles (n is the number of spatial dimensions), $\Sigma_t, \Sigma_m \in R^{n \times n}$ the corresponding uncertainties of the form $\Sigma = \text{diag}(\sigma_1^2, \dots, \sigma_n^2)$ and $M(\vec{x}) = R\vec{x} + \vec{s}$ the function that applies rotation (R) and translation (\vec{s}) to position \vec{x} . This cost function has the advantage that it works directly on localization data, eliminating the need for a pixelated representation of the SMLM data. Furthermore, it can take into account (varying and anisotropic) localization uncertainties. In order to reduce the computational cost, we prealign the particles using a fast Gaussian mixture model (GMM) based registration method [18] (Methods section for details). We further speed-up the computation by implementing both the GMM and the Bhattacharya cost function evaluation on a GPU.

2.2. RESULTS

We have tested our method on three different datasets with $\sim 80\%$, $\sim 50\%$ and $\sim 30\%$ DOL. The datasets contain 2D DNA origami nanostructures with 37 designed binding sites on a hexagonal grid with 5 nm spacing displaying the letters TUD (Figure 2.1a). These were imaged using DNA-PAINT [10] (see Methods section) resulting in an SMLM image (see Figure 2.1b-d for part of the full field of view). Manual segmentation of the 80% DOL dataset resulted in 383 instances of the imaged logos that were fed into the all-to-all registration pipeline (Figure 2.1e). The average number of localizations per particle is around 2060 and the mean localization uncertainty is 0.81 ± 0.26 nm. Figure 2.1f shows our final reconstruction, which has an excellent correspondence to the designed origami. The image resolution, quantified with the Fourier Ring Correlation [3] (FRC) value is 3.3 nm for the reconstruction (see Figure 2.1g), a value close to $\lambda/175$ (with $\lambda = 580$ nm the fluorescence emission wavelength). The reconstruction quality at the outside of the origami is consistent with the low incorporation efficiency of strands on the outside of origami's as observed earlier [19].

The proposed particle fusion algorithm was further benchmarked with lower DOL PAINT data. Figure 2.2 illustrates the evolution of the reconstruction through the different steps of the fusion pipeline. These were obtained by fusing (manually segmented) 442 (Figure 2.2a-c) and 549 (Figure 2.2d-f) TUD logos for the 50% and 30% DOL datasets. With an average number of localizations per particle of 630 and 453 for 50% and 30% DOL, respectively, we were able to reconstruct the logo, which is unrecognizable in the raw data (Figure 2.2c, f). The final reconstructions consist of around 280,000 and 250,000

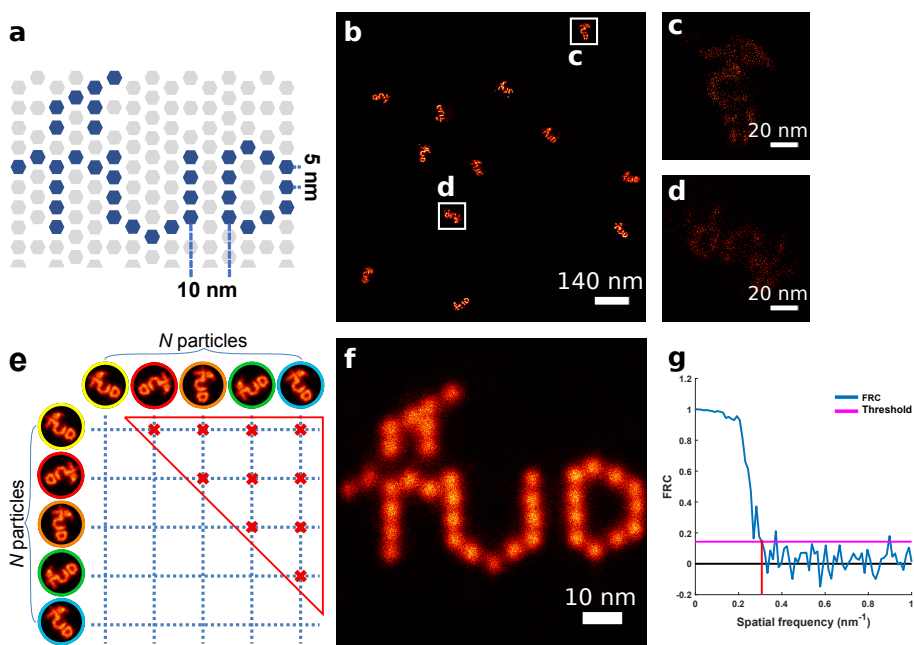


Figure 2.1: Template free 2D particle averaging for localization microscopy. (a) Schematic representation of the DNA origami for a grid structure designed to carry 37 DNA-PAINT docking sites of the logo “TUD”. Strands are color-coded to denote strand extensions. (b) Regions of interest of the reconstructed DNA-PAINT SMLM image of many particles. (c, d) Highlighted areas in b depicting similar copies of the structure with different orientation. (e) All-to-all registration schematic showing all $N(N - 1)/2$ pairwise registrations (red crosses). The N absolute registration parameters (translation and rotation) are robustly obtained from the redundant relative registration parameters. (f) Final reconstruction as a result of fusing 383 individual particles. (g) The average Fourier ring correlation (FRC) curve the final reconstruction in f showing an image resolution of 3.3 ± 0.3 nm.

localizations, respectively. The fusion of raw particles leads to an FRC resolution of 3.5 nm and 5.0 nm for 50% and 30% DOL, respectively. We have also compared our results with the cryo-EM software package EMAN.2 [6]. While the reconstruction for 50% DOL is similar in visual appearance to our approach, EMAN.2 fails to produce any part of the logo for 30% DOL (compare Figure 2.2f, l). The final reconstruction quality of our method seems to be limited by residual drift on the order of 1-2 nm, assessed by visual comparison with simulated data (Figure A1). This is further supported by simulation results without drift (Figure A2). Additional simulations show that average localization uncertainties larger than the binding site distance result in unresolvable binding sites in the final reconstruction even with perfect registration (Figure A3).

Although our particle fusion method performs robustly even for low DOL, it cannot neutralize the effect of false positive localizations. We use conventional single emitter fitting, followed by localization filtering based on the local sparsity of localization events (see Methods section for details). Alternatively, methods that better handle spatially proximate emitters [20] or detect and remove false positives [14] can be used (Figure A4).

In addition to the above PAINT data, we applied our method to experimental and

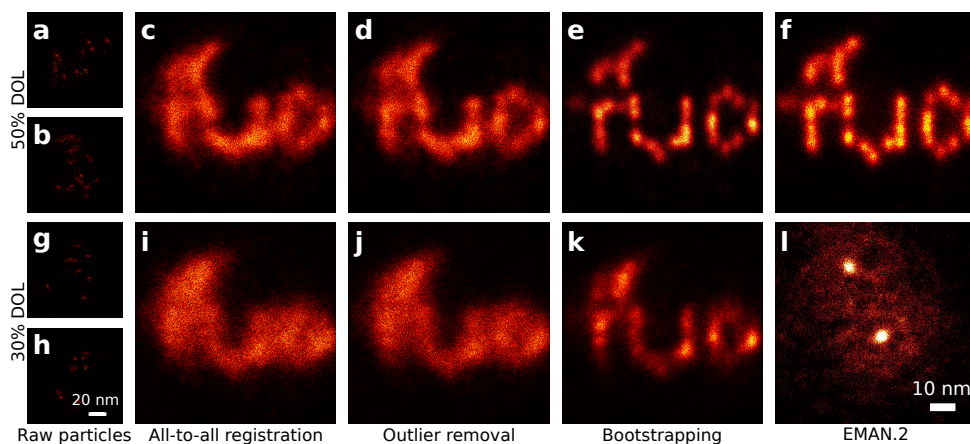


Figure 2.2: (a-b) Two example raw particles with 50% DOL. (c-e) The evolving super-particle for the dataset with 50% DOL. All-to-all registration and averaging of 442 logos with 50% DOL resulted in the blurry reconstruction shown in c. This was further improved by removing outlier registrations in d which is subsequently used as the data-driven model in an all-to-template registration (bootstrapping). The final reconstruction in e illustrates the superparticle with around 400,000 localizations. (f) Reconstruction using EMAN.2 software with 253 included particles and the minimum of 3 classes for the class averaging. (g-h) Two example raw particles with 30% DOL. (i-k) The evolving superparticle for the dataset with 30% DOL. Similar to the first row, each image depicts the output of each step of the particle fusion pipeline. The final reconstruction in k) is the result of fusing 549 logos with around 250,000 localizations. (l) Reconstruction using EMAN.2 software with 113 included particles and the minimum of 3 classes for the class averaging. EMAN.2 fails to produce any meaningful reconstruction for 30% DOL. In all of the reconstructions in each row, the number of localizations is the same except for the EMAN.2 where classification excludes 42% and 79% of the data for 50% and 30% DOL respectively.

simulated localization data that include bleaching, and that therefore have a different statistical distribution of localization events per fluorophore [21]. We analyzed STORM images acquired from the integral membrane protein gp210 in the NPC (data described previously [4]) from which we manually segmented 304 NPCs with on average 313 localizations. Figure 2.3a shows our reconstruction which reproduces the ring structure of the NPC without any prior assumptions. The hotspot in Figure 2.3a-b is a reconstruction artefact caused by the nonuniform distribution of localizations over the 8 sites of each individual NPC. This statistical variation is enhanced during the registration step as rings are most likely registered such that the sites with more than the average number of localizations become aligned. This artefact can be removed by taking into account the symmetry as prior knowledge (but not any other structural information). We randomly add multiples of $2\pi/8$ to the obtained absolute estimated rotation angles, leading to the uniform distribution as depicted in Figure 2.3c-d. Using EMAN.2 we obtained the averages shown in Figure 2.3e-f, exhibiting a set of 8 blobs with less visibility compared to our method, and suffering from the same hotspot artefact. We did not succeed to include the symmetry in EMAN.2 as there is no access to the estimated absolute angles and no way to explicitly impose the symmetry.

We also tested the applicability of our method to simulated STORM images (see subsection 2.3.6). We generated TUD logos of 65% DOL with three different bleaching rates,

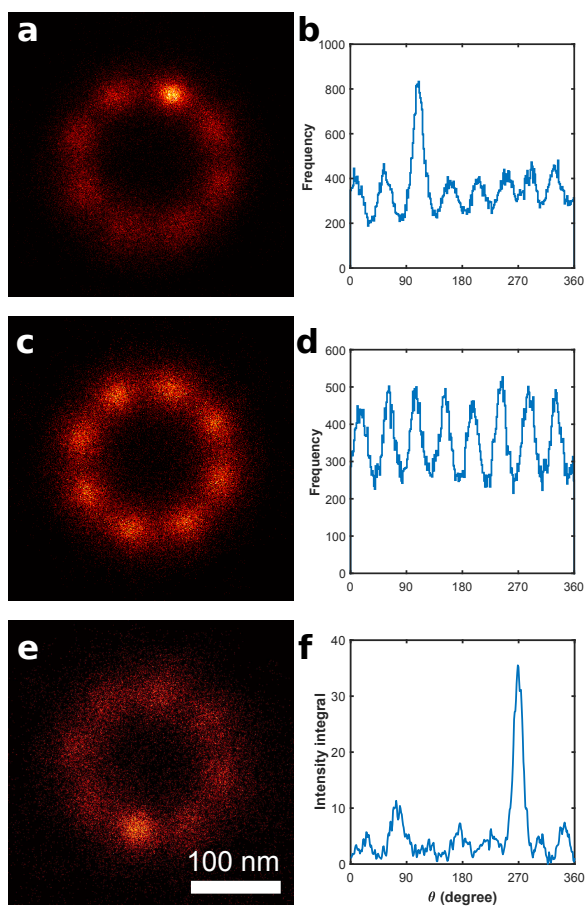


Figure 2.3: (a) Fusion of 304 NPCs with our method retrieves the 8-fold symmetric ring structure without prior knowledge. (b) Localization distribution over azimuthal angles of the reconstruction in a). (c) Reconstruction after incorporating the 8-fold symmetry in the registration, solving the hotspot artefact. (d) Localization distribution over azimuthal angles of the reconstruction in c). (e) Reconstruction by EMAN.2 resulting in 139 included particles (minimum of three classes for class averaging). (f) Azimuthal intensity plot of e). The same hotspot artefact appears, and the visibility of the 8 blobs is less with EMAN.2 compared to our method.

corresponding to average number of localizations per sites of ~ 33 , ~ 13 and ~ 7 , respectively. Our method successfully reconstructs the logo for all three cases, whereas EMAN.2 only succeeds at the lowest bleaching rate (Figure A5). We compared STORM to PAINT data keeping labeling density and average number of localizations per particle the same (Figure A6), indicating that STORM images require a higher labeling density for achieving a successful reconstruction ($\sim 50\%$ DOL compared to $\sim 30\%$ for PAINT). We attribute this to bleaching effects, which skew the distribution of localizations per binding site, effectively lowering the fraction of sites with sufficiently high labeling density.

In summary, we have developed a template-free 2D particle fusion algorithm, which is robust to poor experimental conditions. We benchmarked the performance on PAINT

data, where we achieved a resolution of 3.3 nm for 80%, 3.5 nm for 50% and 5.0 nm for around 30% DOL. We successfully reconstructed an 8-fold symmetric ring structure from STORM data without a priori structural information. The framework can be generalized to treat 3D data as each subcomponent of the pipeline is not restricted to 2D.

2.3. METHODS

2.3.1. MATERIALS

Unmodified, dye-labeled and biotinylated DNA oligonucleotides were purchased from MWG Eurofins. Streptavidin was purchased from Invitrogen (catalog number: S-888). BSA-Biotin was obtained from Sigma-Aldrich (catalog number: A8549). Coverslips were purchased from Marienfeld (Cover slips 18 18 mm, #1.5, catalog number: 0107032). Microscopy slides were ordered from Thermo Fisher Scientific (catalog number: 10756991). Double-sided adhesive tape was purchased from Scotch (catalog number: 665D). Epoxy glue was ordered from Toolcraft (catalog number: TC-EPO5-24). M13mp18 scaffold was obtained from New England BioLabs (catalog number: N4040s). Freeze 'N Squeeze columns were ordered from Bio-Rad (catalog number: 7326165). Agarose was obtained from Biomol (catalog number: 01280.100). 50×TAE Buffer was ordered from Fluka Analytical (catalog number: 67996-10L-F). SYBR safe DNA gel stain was purchased from Invitrogen (catalog number: SS33102). DNA gel loading dye was ordered from Thermo Fisher Scientific (catalog number: R06111). Protocatechuate 3,4-Dioxygenase pseudomonas (PCD) (catalog number: P8279), 3,4-Dihydroxybenzoic acid (PCA) (catalog number: 37580-25G-F) and (+-)-6-Hydroxy-2,5,7,8-tetra-methylchromane-2-carboxylic acid (Trolox) (catalog number: 238813-5G) were obtained from Sigma. 1M Tris pH 8.0 (catalog number: AM9856), 1M Magnesium (catalog number: AM9530G), 0.5 M EDTA pH 8.0 (catalog number AM9261) and 5 M NaCl (catalog number: AM9759) was obtained from Ambion, H₂O (catalog number: 10977-035) was ordered from gibco. Tween 20 was ordered from Sigma-Aldrich (catalog number: p2287).

2.3.2. MICROSCOPY SETUP

DNA-PAINT experiments were carried out on an inverted Nikon Ti-Eclipse microscope (Nikon Instruments) with the Perfect Focus System. For the experiment, an oil-immersion objective (Plan Apo 100x, numerical aperture (NA) 1.49, oil, Nikon Instruments) was used. As excitation laser, a 561 nm (200 mW nominal, Coherent) was used. Excitation light was filtered with a laser clean-up filter (zet561/10x, Chroma Technology Corp). As dichroic a laser dichroic mirror was used (zt561rdc, Chroma Technology Corp). Fluorescence light was spectrally filtered with an emission filter (et575lp, et600/50m, Chroma Technology Corp.) and imaged on a scientific complementary metal-oxide-semiconductor (sCMOS) camera (Zyla 4.2, Andor Technologies).

2.3.3. DNA ORIGAMI SELF-ASSEMBLY

The DNA origami structures were formed in a one-pot reaction with a 50 μ l total volume containing 10 nM scaffold strand (M13mp18), 100 nM core staples, 1 μ M biotinylated staples and 1 μ M of the staples extended with DNA-PAINT docking sites for the 20 nm

grid and 10 nm grid drift markers. For the 80% DOL case of the TUD logo, a 1 μM concentration of staples extended for DNA-PAINT was used. In the 50% DOL case of the TUD logo, a mixture of 0.8 μM extended staples and 0.2 μM not extended staples was used. For the 30% DOL case of the TUD logo, a mixture of 0.6 μM extended staples with 0.4 μM not extended staples was used. The folding buffer was 1x TE buffer with 12.5 mM MgCl₂. The structures were annealed using a thermal ramp. First, incubating for 5 min at 80 °C, then going from 65 to 4 °C over the course of 3 hours. After self-assembly, the structures were mixed with 1x loading dye and then purified by agarose gel electrophoresis (1.5% agarose, 0.5x TAE, 10 mM MgCl₂, 1x SYBR Safe) at 3 V/cm for 3 hours. Gel bands were cut, crushed and filled into a Freeze 'N Squeeze column and spun for 5 min at 1000xg at 4 °C. As DNA-PAINT docking site a TT spacer followed by a 9 nucleotide 3' extension was used (5'-staple-TT-ATACATCTA-3'). The imager was the 9-nucleotide reverse complement of the docking site with a Cy3b fluorescent molecule attached at the 3' end (5' TAGATGTAT-Dye-3').

2.3.4. SUPERRESOLUTION DNA-PAINT IMAGING WITH DNA ORIGAMI

For chamber preparation, a piece of coverslip (no. 1.5, 18 x 18 mm², ~0.17 mm thick) and a glass slide (3 x 1 inch², 1 mm thick) were sandwiched together by two strips of double-sided tape to form a flow chamber with inner volume of ~20 μl . First, 20 μl of biotin-labeled bovine albumin (1 mg/ml, dissolved in Buffer A (10 mM Tris-HCl pH 7.5, 100 mM NaCl, 0.05% Tween 20, pH 7.5)) was flown into the chamber and incubated for 2 min. Then the chamber was washed using 40 μl of Buffer A. Second, 20 μl of streptavidin (0.5 mg/ml, dissolved in Buffer A) was then flown through the chamber and incubated for 2 minutes. Next, the chamber was washed with 40 μl of Buffer A and subsequently with 40 μl of Buffer B (5 mM Tris-HCl pH 8, 10 mM MgCl₂, 1 mM EDTA, 0.05% Tween 20, pH 8). Then ~100 pM of the TUD DNA origami structures, ~100 pM of the 10 nm grid DNA origami structures and ~200 pM of the 20 nm DNA origami structures were flown into the chamber and allowed to bind for 2 minutes. Afterwards the chamber was washed with 40 μl of Buffer B again. Finally, the imaging buffer with Buffer B and 1x Trolox, 1x PCA, and 1x PCD12 with the Cy3b-labeled imager strand was flown into the chamber. The chamber was sealed with epoxy before subsequent imaging. For the 30% and 80% DOL experiment, an imager concentration of 1 nM was used. For the 50% DOL experiment, an imager concentration of 2 nM was used. At the end, the actual labeling densities were determined by counting the number of occupied sites on each particle versus the number of designed sites on the logo, i.e. 37 binding sites.

For all three experiment (80%, 50% and 30% DOL) an Andor Zyla 4.2 with a readout bandwidth of 200 MHz at 16 bit was used. A 2x2 pixel binning was applied resulting in an effective pixel size of 130 nm (taking the 100x magnification of the microscope into account). The recorded field of view was 512x512 pixel (66.5 μm x 66.5 μm). The acquisition frame rate of 2.86 Hz for the 50% and 30% DOL case and 3.33 Hz for the 80% DOL case was used over the course of 100,000 frames. The excitation intensity was ~1.86 kW/cm² at 561 nm at the sample plane.

2.3.5. SINGLE AND MULTIEMITTER FITTING OF EXPERIMENTAL DATA

Single molecule reconstruction and drift correction was performed as described before [10]. The average number of photons per localization events for 80%, 50% and 30% DOL are 7.0×10^4 , 4.9×10^4 and 5.3×10^4 while the background photon counts per frame per pixel are 1.1×10^3 for the first two datasets and 0.9×10^3 for the last one respectively. Average uncertainties are 0.96 nm, 1.33 nm and 1.28 nm for 80%, 50% and 30% DOL datasets respectively. The uncertainties are estimated per localization from the data as previously reported [22]. Data was postprocessed by omitting localizations with localization uncertainties above 2 nm. In order to reduce the effect of false positive localization in single emitter fitted dataset, we filtered 80% and 50% DOL datasets before fusion. In each segmented particle, localizations are discarded if there are less than 10 localizations in a circular neighborhood of radius $r = 0.015$ pixels around the localization of interest (see Figure A7 for filtering effect on the final reconstruction). The effect of false positives on 30% DOL data is less serious due to the fact that the probability of overlapping emission patterns is low. Therefore, for single emitter fitted 30% DOL data, we did not filter the raw particles.

Multiemitter fitting was performed in the following way. Subregions identified as containing TUD logos were selected from the raw data for multiemitter fitting. Each time frame in each TUD containing subregion was analyzed independently. Multiemitter fitting was performed by finding the posterior probability distribution of the parameters $\theta = \{x_1, y_1, I_1, \dots, x_N, y_N, I_N, \alpha, \beta, \gamma\}$ using Markov Chain Monte Carlo (MCMC), where x_n, y_n, I_n correspond to the location and intensity of the n th emitter and α, β, γ parameterize a tiled plane background model. The mean and standard deviation of x_n, y_n were used for further analysis. The MCMC chain was initialized by first using a Reversible Jump MCMC [23] procedure to find the most probable number of emitters and their locations. The point spread function (PSF) model used in the fitting was created by localizing, shifting and averaging together more than 100 high signal, single emitter events from the raw data. A 4x subsampled PSF was created by padding the Fourier transform. The model of each single emitter was created by linear interpolation of the subsampled PSF and scaling by I . The x_n, y_n were connected across time frames and only binding events that spanned two or more frames were retained. False positive and large uncertainty localizations were removed from the data. A large uncertainty was defined as a standard deviation larger than 0.0075 pixels. False positives were removed by keeping localizations if they had N_{min} number of localizations within a distance D . For each data set, N_{min} and D were found by taking D as the median localization uncertainty (before thresholding) and N_{min} as the median number of localizations within a distance D . Using visual inspection of several origami structures, N_{min} and D were then adjusted to minimize false localizations between docking stands while retaining as many localizations as possible. For 80%, 50%, and 30% DOL labelling, the values used for N_{min} and D were 10, 10, and 9 localizations within 0.0075, 0.008 and 0.0095 pixels respectively (pixel size 130 nm).

The final distribution of localizations per particle (Figure A8) agrees qualitatively with the assessed DOL for the three datasets. The width of the distributions is an indication that the overall distribution is a convolution of the Poissonian distribution of the number of localizations per binding site and the distribution of active binding sites

according to the average DOL.

2.3.6. SIMULATION SETUP

We assessed the performance of our method on simulated data to which end we generated sets of 256 TUD logos matching the experimental specifications of our setup with 100% (most optimal condition), 50% and 30% density of labeling (DOL). The simulation creates a DNA origami design pattern on which docking sites are defined as in the actual design (Figure 1a). Our model consists of 37 binding sites arranged on a 5 nm hexagonal grid to form the shape TUD. Based on the DOL, a fraction of these binding sites, which is drawn from a uniform distribution, are occupied for each simulated structure. For simulated PAINT datasets, M_i localizations are assigned to each site according to a Poisson distribution with a mean value of $N_{\text{frame}} / (T_{\text{on}} + T_{\text{off}})$ where N_{frame} and $T_{\text{on}} / T_{\text{off}}$ are the number of recorded frames and the mean lifespan of an on/off fluorescent label, respectively. For STORM data, M_i is computed as the minimum of $M_{i;b}$ and $1 + M_{i;g}$ where $M_{i;b}$ is a random variable drawn from a Binomial distribution with N_{frame} number of trials and a success probability of $1 - e^{-k_{\text{on}}}$ ($k_{\text{on}} = 1 / T_{\text{on}}$) and $M_{i;g}$ is drawn from a geometric distribution with probability parameter of $1 - e^{-k_b}$ with k_b as the bleach rate. Here, we use $N_{\text{frame}} = 100,000$ and $1,000$ for PAINT and STORM datasets, respectively, and $T_{\text{on}} = 3$ and $T_{\text{off}} = 2,000$ for both techniques. In reality, finite length flexible linkers cause fluorophores to move over the surface of a hemisphere located at each binding site and therefore only their 2D projection is recorded. We set the linker size to 0.66 nm. With $n_{ph} = 5,000$ detected signal photons, $n_{bg} = 1$ background photons per pixel, back-projected pixel size of 130 nm and $\sigma_0 = 1.066$ px nominal spot width, lateral localization uncertainties are computed using equation 6 from ref. [24]. This results in an effective (average) localization uncertainty of ~ 2.3 nm. This uncertainty is larger than the pure experimental localization uncertainty from the photon count, but incorporated to some degree the residual drift in the experimental data. Subsequently, these uncertainties are used to randomly displace the previously computed localizations around each binding site, according to a normal distribution. Finally, all the generated particles are randomly rotated within 0 and 360 degree and translated within a range of 10 nm around the center, according to a uniform distribution.

2.3.7. ALL-TO-ALL REGISTRATION

The developed particle fusion algorithm consists of four main building blocks: 1) computing the upper triangular matrix A that contains all relative registrations (Figure 1e), which we call the all-to-all registration matrix, 2) calculating the absolute orientations from these relative elements, 3) registration outliers removal and 4) bootstrapping the registrations.

RELATIVE REGISTRATIONS

Each element of the matrix A is obtained by optimizing equation 2.1 in a coarse to fine manner. We align each pair of particles using the Gaussian mixture model (GMM) registration method [18] with multiple initial angles. This provides us with a set of transformation parameters (rotation angle, translation vector) out of which we select the set that maximizes the Bhattacharya cost function as the final value for the set of relative

transformation parameters for that pair. The GMM registration method minimizes the special case of the Bhattacharya cost function in which all localization uncertainties are equal:

$$D = \sum_{i=1}^{K_t} \sum_{j=1}^{K_m} \exp\left(-\|\tilde{x}_{t,i} - M(\tilde{x}_{m,j})\|^2 / 2\sigma^2\right). \quad (2.2)$$

For this case, there exists an analytical approximation to the problem with only linear computational complexity [18]. Here, σ is a tuning parameter which is dataset specific and which we set empirically to $0.01 \times l$, where l is the camera pixel size in nm, for 80% and 50% DOL and $0.1 \times l$ for 30% DOL experimental data. The GMM cost function is optimized using the interior-point algorithm for multiple initial angles ranging from $-\pi$ to π evenly spaced by $\pi/4$. The Bhattacharya cost function equation 2.1 is evaluated for each of the local optima of the GMM cost function that are found and the set of transformation parameters with the optimum Bhattacharya cost function is finally selected. This procedure results in an all-to-all registration matrix A with $(N(N-1))/2$ relative registration parameters. Each element $a_{i,j}$, $i, j \in \{1, \dots, N\}$, $\forall j > i$, of this matrix is the set of estimated relative rigid transformation parameters M_{ij} , that aligns particle i to particle j :

$$M_{ij} = \begin{bmatrix} R_{ij} & t_{ij} \\ 0 & 1 \end{bmatrix}, \quad (2.3)$$

with $R_{ij} \in \text{SO}(n)$ and $t_{ij} \in R^{(n \times 1)}$ being the relative rotation matrix and the translation vector, respectively, in n spatial dimensions.

FROM RELATIVE TO ABSOLUTE TRANSFORMATION PARAMETERS

In order to properly align all particles without bias towards the final reconstruction, we need to estimate the absolute transformation parameters M_i for $i = 1, \dots, N$. The consistency equation that relates the relative parameters to absolute parameters is given by:

$$M_{ij} = M_j M_i^{-1}, \forall j > i. \quad (2.4)$$

Direct linear numerical solution of equation 2.4 is difficult as the M_i contain a rotation matrix which is modulo 2π . To handle this problem, we use the (smooth) Lie-algebraic representation of the transformation [17, 25] which solves the following optimization problem instead:

$$\underset{M_1, \dots, M_N}{\operatorname{argmin}} \sum_{\substack{i,j \\ i>j}} \rho(d(M_{ij}, M_j M_i^{-1})), \quad (2.5)$$

with distance function $d(X, Y) = \|\log(Y X^{-1})\|_F$, with F denoting the Frobenius norm (square root of the sum of absolute squares of the elements of the matrix) and $\rho(x) = |x|$ the L_1 loss function. The use of this norm makes the procedure robust to outliers [26]. This is important as the registration can be trapped in a local minimum for nearly symmetric particles at 180 degree rotations. We solve the optimization problem 2.5 using an iterative gradient descent approach [17, 27]. For our 2D geometry, we use as input a matrix with $4 \times 4 \times N(N-1)/2$ elements which holds the $N(N-1)/2$ stack of all the relative matrices M_{ij} of size 4×4 together with the indicator matrix of size $2 \times N(N-1)/2$ which stores the correspondence indices of $N(N-1)/2$ particle pairs.

REMOVAL OF OUTLIER REGISTRATIONS VIA SELF-CONSISTENCY

After the first round of Lie-algebraic averaging, N sets of absolute transformation parameters are obtained. By plugging them into equation 2.4, $(N(N-1))/2$ relative transformation parameters \hat{M}_{ij} are obtained, which can differ from the parameters M_{ij} estimated from the all-to-all registration. It appears that these differences are mostly in the rotation rather than the translation; hence, we only do this consistency check based on the \hat{R}_{ij} (or equivalently in 2D the angle $\hat{\alpha}_{ij}$).

Figure A9 shows the histograms of the quantity $|\hat{\alpha}_{ij} - \alpha_{ij}|$ for different DOL. Next to the correct pair registrations (the central peak) there are clearly outliers. Furthermore, the outlier fraction increases when the DOL decreases. Removal of these outlier registrations is therefore a mandatory. We have implemented this by excluding registration pairs with $|\hat{\alpha}_{ij} - \alpha_{ij}| > \epsilon$, with ϵ a threshold parameter, for a second round of Lie-algebraic averaging.

Assuming that the all-to-all registration matrix A is a graph in which each matrix element A_{ij} is an edge that connects node (particle) i to node j , we can perform the optimization as long as this graph is connected, i.e. for every pair there is at least one path connecting them. Intuitively, the outlier removal step is equivalent to optimizing this graph for the most consistent path through all the nodes. For very low DOL, most of these paths are inconsistent. Therefore, a smaller threshold results in a better reconstruction as long as the number of the remaining new relative parameters is larger than $N-1$. In this work, we set the threshold parameter $\epsilon = 5$ degree as it is the smallest angle that still keeps the graph of all-to-all registration for the worst dataset (30% DOL) connected.

This step does not remove particles from the fusion but only filters the redundant set of registration parameters. The large fraction of outlier pair registrations is the reason why the redundancy of the all-to-all registration is needed for achieving a robust fusion pipeline, and why a pyramid registration would lead to an inferior reconstruction (because of the error propagation from the randomly picked wrong pair registrations at the bottom layer of the pyramid).

It worth mentioning that this step is actually a simplified variant of the RANSAC based motion averaging scheme as detailed in ref. [27]. We obtain, however, the absolute angles in step 2 using all available relative angles instead of computing the initial absolute angles based on the minimum number of relative angles, i.e. $N-1$. This is especially important for very low DOL datasets as the result of averaging only $N-1$ random relative angles is too corrupted to provide a good initial start for RANSAC.

BOOTSTRAP REGISTRATIONS

The above steps already provide a good reconstruction. It is, however, beneficial to use the outcome as a data driven model/template to realign all individual particles to this model, i.e. bootstrapping the registrations [27]. The all-to-template registration, in this step, is done based on registering every single particle to a resampled version of the super-particle from step 3. The resampling is crucial as we want to do the realignment based on the most consistent localizations in the dense areas of the previous reconstruction. We randomly draw samples from the total set of localizations with a probability density function proportional to the density of localizations. We set the number of resampled localizations to 5,000 for the experimental data as it represents about 2 particles

for 80% DOL and 5-10 particles for 50% and 30% DOL, which already gives a good overall shape. This value must not be chosen too large as to avoid overfitting to noise (false positives in the data). For the 50% DOL dataset, we obtain a better reconstruction when the bootstrapping is repeated twice (Figure A10). It appears that after iterating twice, the registration has converged. For 100% DOL, the reconstruction already converges at the first iteration whereas for 30% DOL, the image gets worse due to the two very dense areas. Finally, we registered each of the raw particles to the data-generated template using the routine as described in step 1.

We benchmarked the performance of our proposed registration method on simulated 100% DOL data for which we have the groundtruth registration parameters. Figure A11 shows that the histogram of the overall error between the final estimated angles and the ground-truth from simulation. The histogram fits a normal distribution with a standard deviation of 0.9 degree. Considering the dimensions of the origami, this error will result in a displacement of ± 0.55 nm at the edges of the logo at worst case, indeed smaller than the minimum binding sites distance and approximately equal to the average localization uncertainty. The corresponding reconstruction in Figure A2g also indicates a perfect match with the origami design.

2.3.8. COMPUTATIONAL COMPLEXITY

We achieved a complete all-to-all registration of 383 structures (resulting in $\sim 73,000$ pair registrations) of on average 2,060 localizations per origami (80% DOL) on four K40c Tesla cards on a 40 core server (Xeon E5-2670v3) in 2 hours and in 40 hours on a cheap GPU in a regular desktop PC (Quadro K620, 2 GB RAM, 8 core Xeon E5-1660v3). These run times correspond to the most computationally expensive dataset. However, in practice for highly labeled data, averaging a small subset of registrations can yield a fast but high quality reconstructions. Figure A12 shows the reconstruction of 80% DOL data with only $\sim 2\%$ of the registration pairs with a computational time of ~ 10 minutes.

REFERENCES

- [1] Hamidreza Heydarian, Florian Schueder, Maximilian T. Strauss, Ben van Werkhoven, Mohamadreza Fazel, Keith A. Lidke, Ralf Jungmann, Sjoerd Stallinga, and Bernd Rieger. Template-free 2d particle fusion in localization microscopy. *Nature Methods*, 15(10), 2018.
- [2] Teresa Klein, Sven Proppert, and Markus Sauer. Eight years of single-molecule localization microscopy. *Histochemistry and Cell Biology*, 141(6), 2014.
- [3] Robert P. J. Nieuwenhuizen, Keith A. Lidke, Mark Bates, Daniela Leyton Puig, David Grünwald, Sjoerd Stallinga, and Bernd Rieger. Measuring image resolution in optical nanoscopy. *Nature methods*, 10(6), 2013.
- [4] Anna Löschberger, Sebastian van de Linde, Marie-Christine Dabauvalle, Bernd Rieger, Mike Heilemann, Georg Krohne, and Markus Sauer. Super-resolution imaging visualizes the eightfold symmetry of gp210 proteins around the nuclear pore complex and resolves the central channel with nanometer resolution. *Journal of Cell Science*, 125(3), 2012.

- [5] Anna Szymborska, Alex de Marco, Nathalie Daigle, Volker C. Cordes, John A. G. Briggs, and Jan Ellenberg. Nuclear pore scaffold structure analyzed by super-resolution microscopy and particle averaging. *Science*, 341(6146), 2013.
- [6] Guang Tang, Liwei Peng, Philip R. Baldwin, Deepinder S. Mann, Wen Jiang, Ian Rees, and Steven J. Ludtke. Eman2: An extensible image processing suite for electron microscopy. *Journal of Structural Biology*, 157(1), 2007.
- [7] Mikhail Kudryashev, Daniel Castaño-Díez, and Henning Stahlberg. Limiting factors in single particle cryo electron tomography. *Computational and Structural Biotechnology Journal*, 1(2).
- [8] Schuyler B. Van Engelenburg, Gleb Shtengel, Prabuddha Sengupta, Kayoko Waki, Michal Jarnik, Sherimay D. Ablan, Eric O. Freed, Harald F. Hess, and Jennifer Lippincott-Schwartz. Distribution of escrt machinery at hiv assembly sites reveals virus scaffolding of escrt subunits. *Science*, 343(6171):653–656, 2014.
- [9] Robert D. M. Gray, Corina Beerli, Pedro Matos Pereira, Kathrin Maria Scherer, Jerzy Samolej, Christopher Karl Ernst Bleck, Jason Mercer, and Ricardo Henriques. Virusmapper: open-source nanoscale mapping of viral architecture through super-resolution microscopy. *Scientific Reports*, 6, 2016.
- [10] Joerg Schnitzbauer, Maximilian T. Strauss, Thomas Schlichthaerle, Florian Schueder, and Ralf Jungmann. Super-resolution microscopy with dna-paint. *Nature Protocols*, 12(6), 2017.
- [11] Desirée Salas, Antoine Le Gall, Jean-Bernard Fiche, Alessandro Valeri, Yonggang Ke, Patrick Bron, Gaetan Bellot, and Marcelo Nollmann. Angular reconstitution-based 3d reconstructions of nanomolecular structures from superresolution light-microscopy images. *Proceedings of the National Academy of Sciences*, 114(35), 2017.
- [12] Anne Burgert, Sebastian Letschert, Sören Doose, and Markus Sauer. Artifacts in single-molecule localization microscopy. *Histochemistry and Cell Biology*, 144(2), Aug 2015.
- [13] Sebastian van de Linde, Steve Wolter, Mike Heilemann, and Markus Sauer. The effect of photoswitching kinetics and labeling densities on super-resolution fluorescence imaging. *Journal of Biotechnology*, 149(4):260 – 266, 2010. BioImaging - Contributions from Biology, Physics and Informatics.
- [14] Patrick Fox-Roberts, Richard Marsh, Karin Pfisterer, Asier Jayo, Maddy Parsons, and Susan Cox. Local dimensionality determines imaging speed in localization microscopy. *Nature communications*, 8, 2017.
- [15] Jordi Broeken, Hannah Johnson, Diane S. Lidke, Sheng Liu, Robert P. J. Nieuwenhuizen, Sjoerd Stallinga, Keith A. Lidke, and Bernd Rieger. Resolution improvement by 3d particle averaging in localization microscopy. *Methods and Applications in Fluorescence*, 3(1), 2015.

- [16] Richard Henderson. Avoiding the pitfalls of single particle cryo-electron microscopy: Einstein from noise. *Proceedings of the National Academy of Sciences*, 110(45), 2013.
- [17] V. Govindu. Lie-algebraic averaging for globally consistent motion estimation. In *2013 IEEE Conference on Computer Vision and Pattern Recognition*, volume 1. IEEE Computer Society, jul 2004.
- [18] B. Jian and B. C. Vemuri. Robust point set registration using gaussian mixture models. *IEEE Transactions on Pattern Analysis and Machine Intelligence*, 33(8), 2011.
- [19] Maximilian T. Strauss, Florian Schueder, Daniel Haas, Philipp C. Nickels, and Ralf Jungmann. Quantifying absolute addressability in dna origami with molecular resolution. *Nature Communications*, 9(1), 2018.
- [20] Fang Huang, Samantha L. Schwartz, Jason M. Byars, and Keith A. Lidke. Simultaneous multiple-emitter fitting for single molecule super-resolution imaging. *Biomed. Opt. Express*, 2(5), May 2011.
- [21] Robert P. J. Nieuwenhuizen, Mark Bates, Anna Szymborska, Keith A. Lidke, Bernd Rieger, and Sjoerd Stallinga. Quantitative localization microscopy: Effects of photophysics and labeling stoichiometry. *PLOS ONE*, 10(5), 05 2015.
- [22] Carlas S Smith, Nikolai Joseph, Bernd Rieger, and Keith A Lidke. Fast, single-molecule localization that achieves theoretically minimum uncertainty. *Nature methods*, 7(5):373, 2010.
- [23] Sylvia Richardson and Peter J. Green. On bayesian analysis of mixtures with an unknown number of components (with discussion). *Journal of the Royal Statistical Society: Series B (Statistical Methodology)*, 59(4), 1997.
- [24] Bernd Rieger and Sjoerd Stallinga. The lateral and axial localization uncertainty in super-resolution light microscopy. *Chemphyschem : a European journal of chemical physics and physical chemistry*, 15, 03 2014.
- [25] Ke Ye and Lek-Heng Lim. Cohomology of cryo-electron microscopy. *SIAM Journal on Applied Algebra and Geometry*, 1(1):507–535, 2017.
- [26] R. Hartley, K. Aftab, and J. Trumpf. L1 rotation averaging using the weiszfeld algorithm. In *CVPR 2011*, June 2011.
- [27] Venu Madhav Govindu. Robustness in motion averaging. In P. J. Narayanan, Shree K. Nayar, and Heung-Yeung Shum, editors, *Computer Vision – ACCV 2006*, Berlin, Heidelberg, 2006. Springer Berlin Heidelberg.

2.A. APPENDIX

2

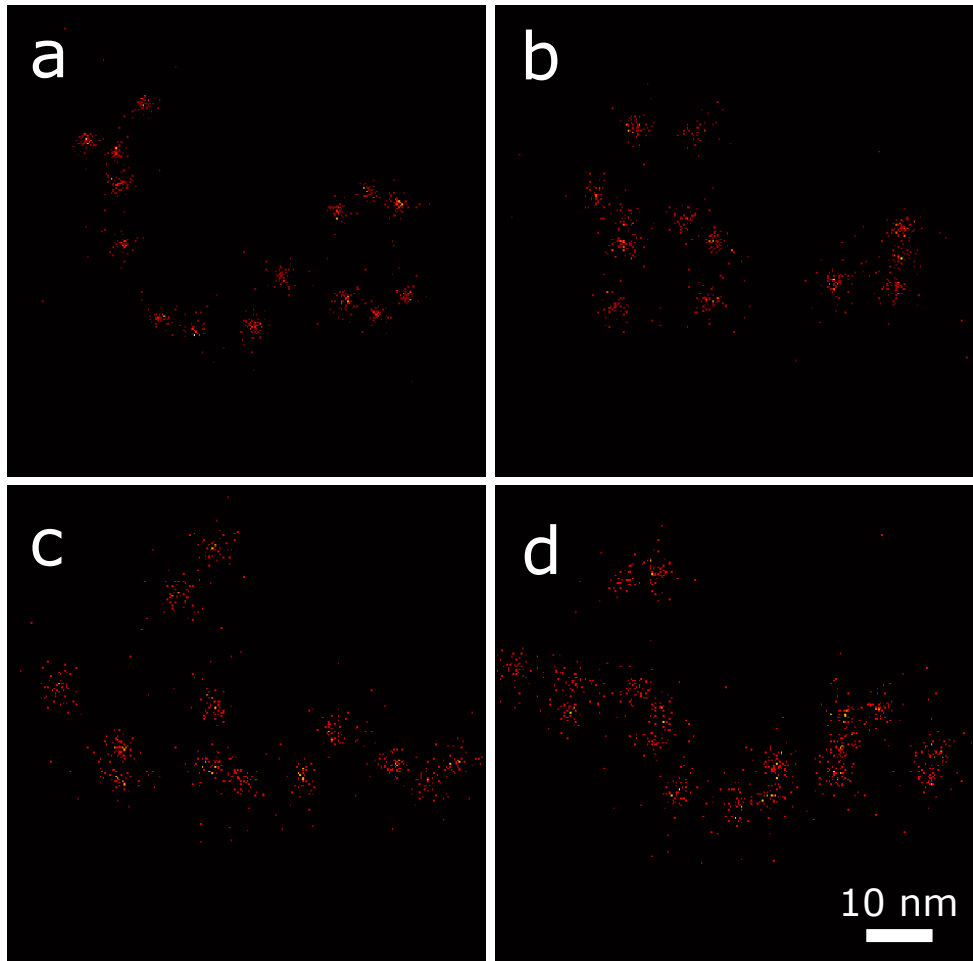


Figure A1: Comparison between simulated 50% DOL samples with different average localization uncertainties with a sample from 50% DOL experimental dataset. (a-c) Simulated samples with mean localization uncertainties of 1.2 nm, 1.8 nm and 2.3 nm respectively. (d) A sample from the experimental dataset with an average localization uncertainty of 0.8 nm. The comparison reveals that the sample from experimental dataset (d) is more similar to figure (c) in visual appearance with larger localization uncertainty rather than figure (a). This difference in the computed uncertainty for the experimental data is likely due to a residual drift after drift correction of about 1-2 nm.

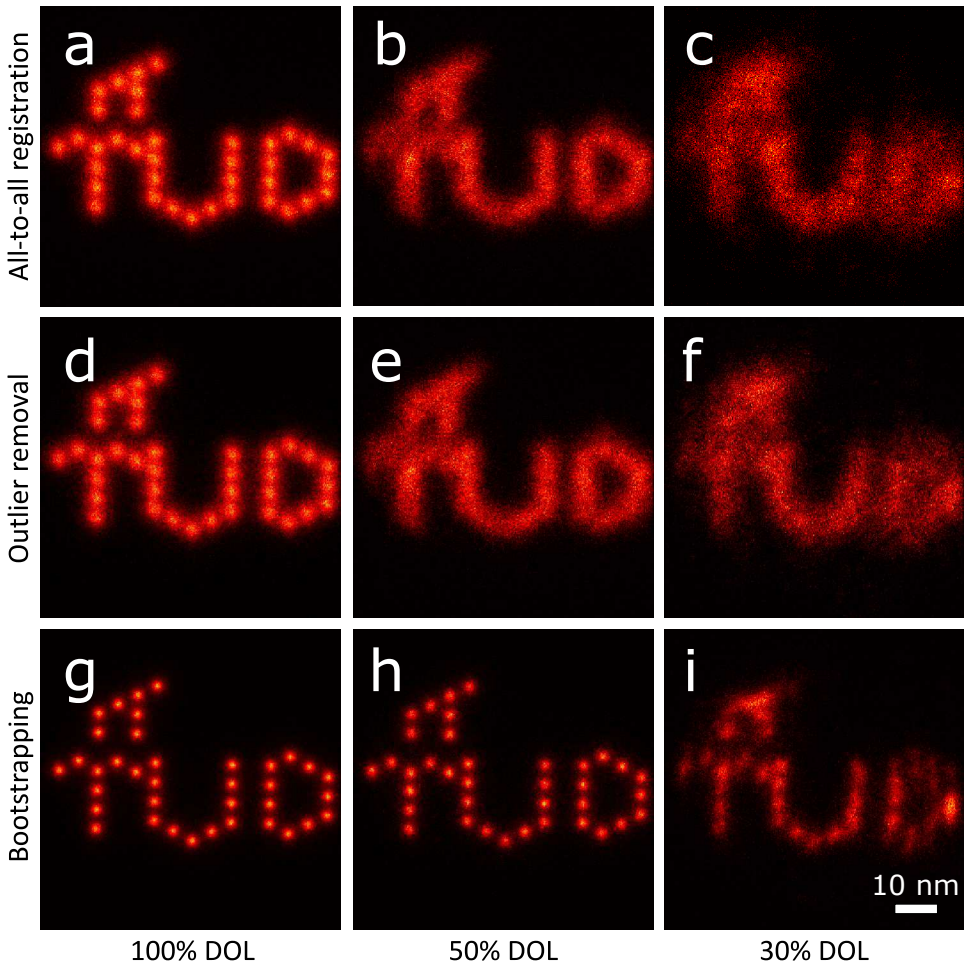


Figure A2: Particle fusion performance on 256 simulated TUD logos with different density of labeling. The output of the algorithm at different steps of the particle fusion for (a-c) All-to-all registration outputs. (d-f) Outlier removal. (g-i) Bootstrapping registrations. The final reconstructions in g-i are the results of fusing 256 logos with around 470,000, 230,000 and 145,000 localizations respectively. In all the reconstructions in each column, the number of localizations is the same. A comparison of the images (a-i) and [Figure 2.2](#) indicates a good match between simulation and experiment. The final results in h and i, however, have better contrast than those from experiment. This is attributed to the effects of residual drift and of false positive localizations, which are not taken into account in the simulations.

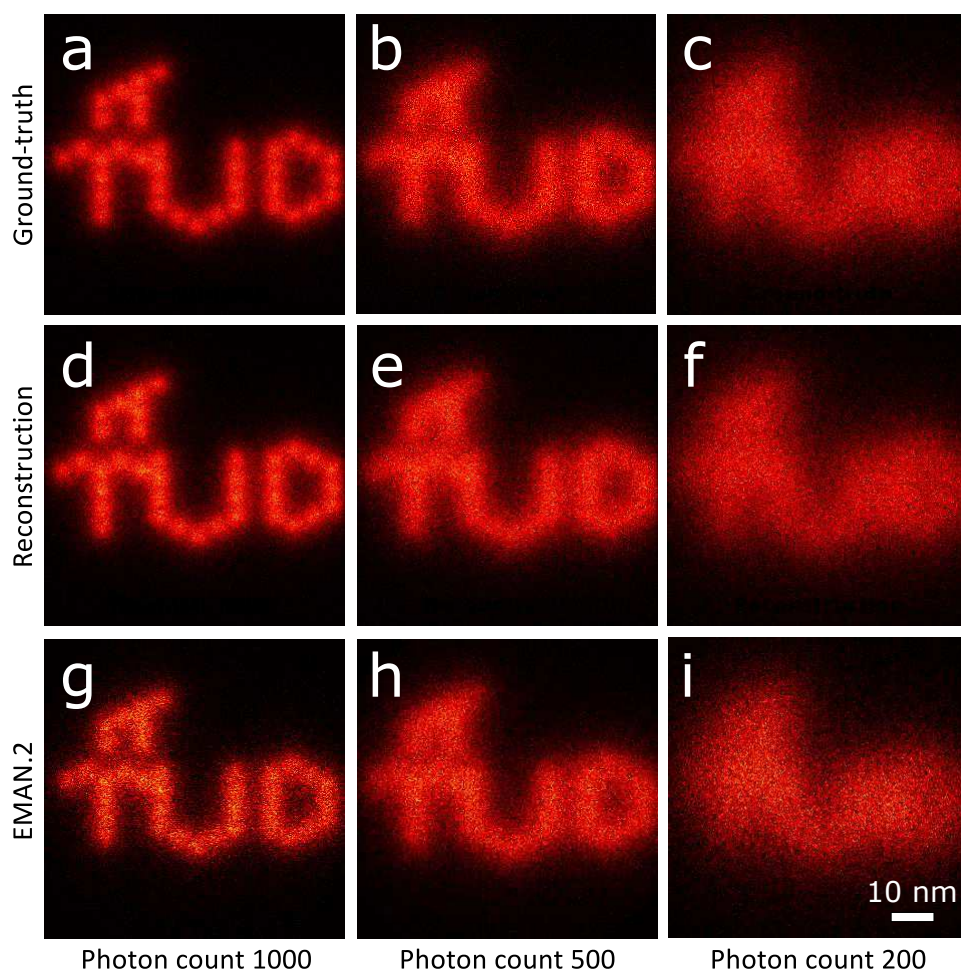


Figure A3: Particle fusion performance on 256 simulated PAINT TUD logos with different photon counts and 100% DOL. (a-c) Ground-truth reconstructions for photon counts of 1000, 500 and 200 or equivalently average localization uncertainties of 5, 7 and 11 nm, respectively. (d-f) Our reconstructions (g-i) Reconstructions using EMAN.2 with 115, 202 and 147 included particles and the minimum of three classes for the class averaging. While the quality of reconstructions is close to the ground-truth both for our method and EMAN.2, the docking sites are hardly resolved as the mean localization uncertainties for all datasets is larger or equal than the minimum binding site distance (5 nm for our datasets).

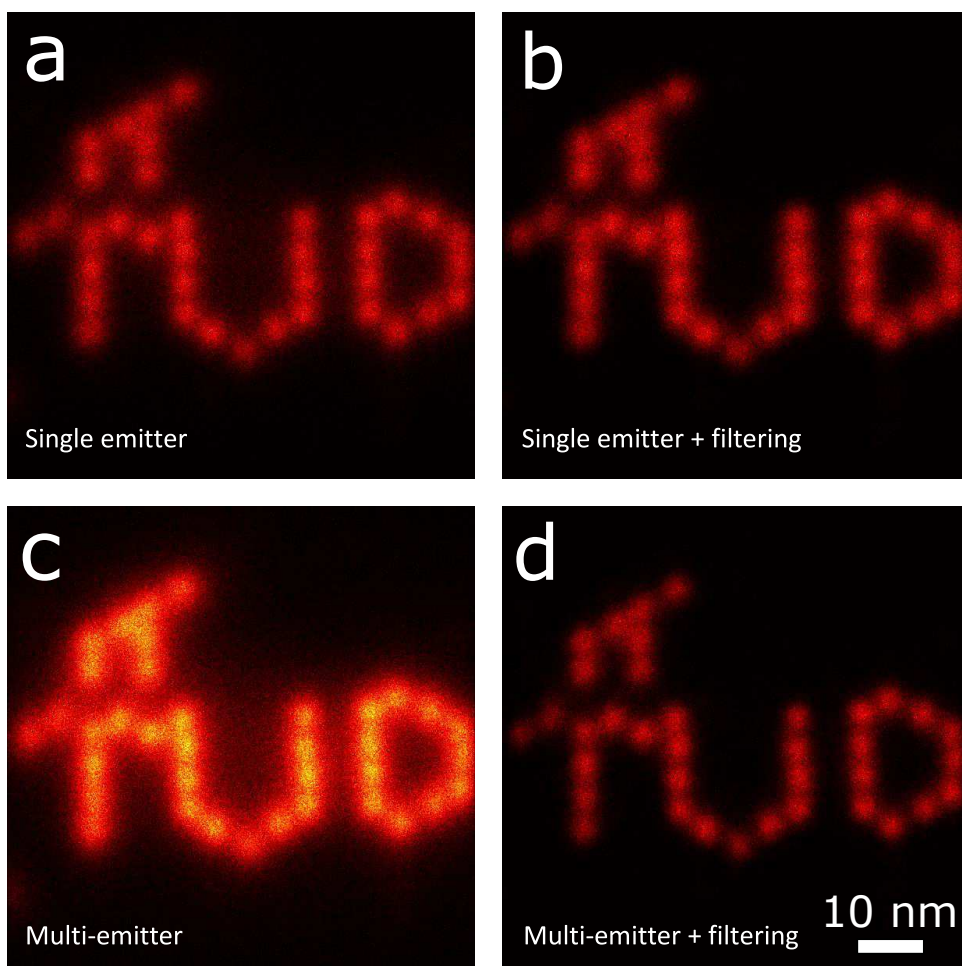


Figure A4: Comparison between the fusion of experimental 80% DOL particles with localizations based on single-emitter and multiemitter fitting and with and without filtering out localizations that are too far away from any other localization. (a) Reconstruction of single emitter fitted particles without filtering (1,017,559 localizations). (b) Reconstruction of filtered (with neighbourhood parameter $r = 0.015$ pixels) single emitter fitted particles (788,875 localizations). (c) Reconstruction of multiemitter fitted particles without filtering (2,591,464 localizations). (d) Reconstruction of filtered (with neighbourhood parameter $r = 0.015$ pixels) multiemitter fitted particles with filtering (548,091 localizations). Comparing figures b and d suggests that the combination of multiemitter fitting and filtering can yield an improved reconstruction with better resolvability of the binding sites, probably because of a reduction of false positive localizations.

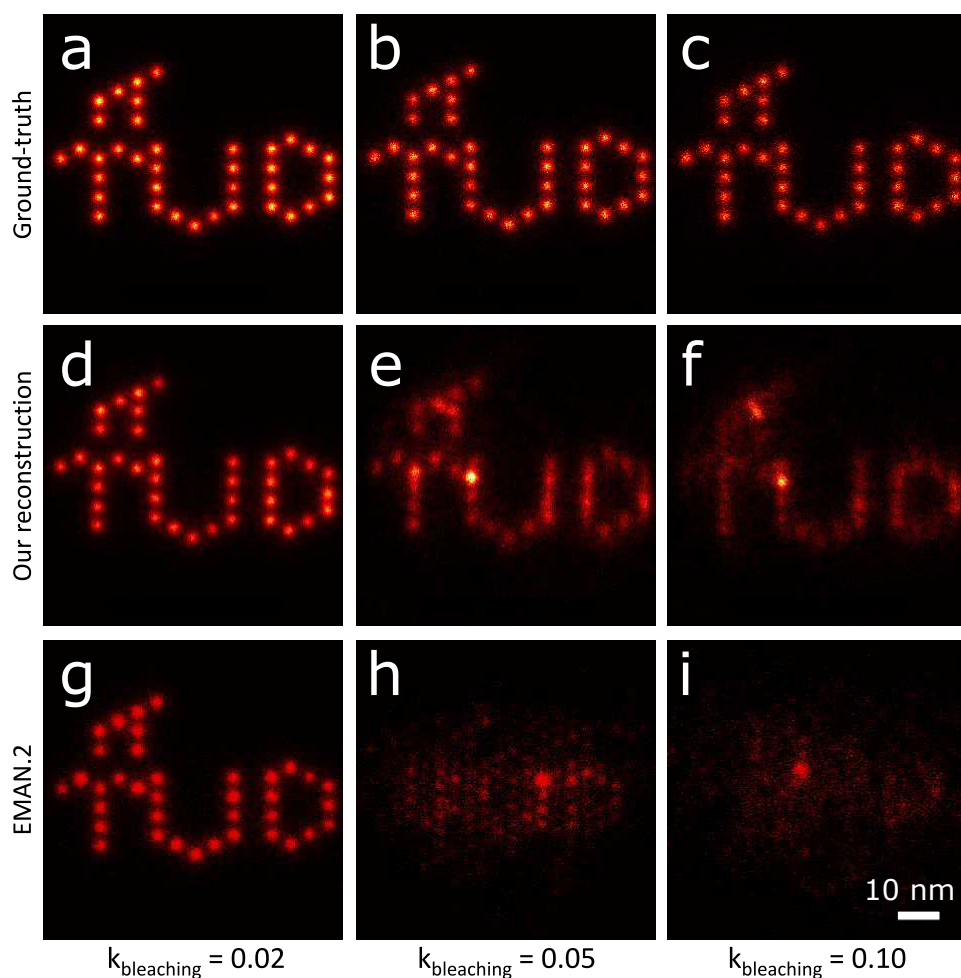


Figure A5: The effect of bleaching rate on particle fusion performance for 65% DOL on simulated STORM-type datasets with a photon count of 5000 and 1000 recorded frames. (a-c) Groundtruth fusion of 256 particles with bleaching rates corresponding to an average number of localizations per binding site equal to ~ 33 , ~ 13 and ~ 7 . (d-f) Our reconstructions. (g-i) Reconstructions using EMAN.2 with 95, 51 and 53 included particles (minimum of three classes for the class averaging). A higher bleaching rate results in a lower number of localizations per sites and a less uniform distribution, which degrades the particle fusion performance. Our method outperforms EMAN.2 at higher bleaching rates.

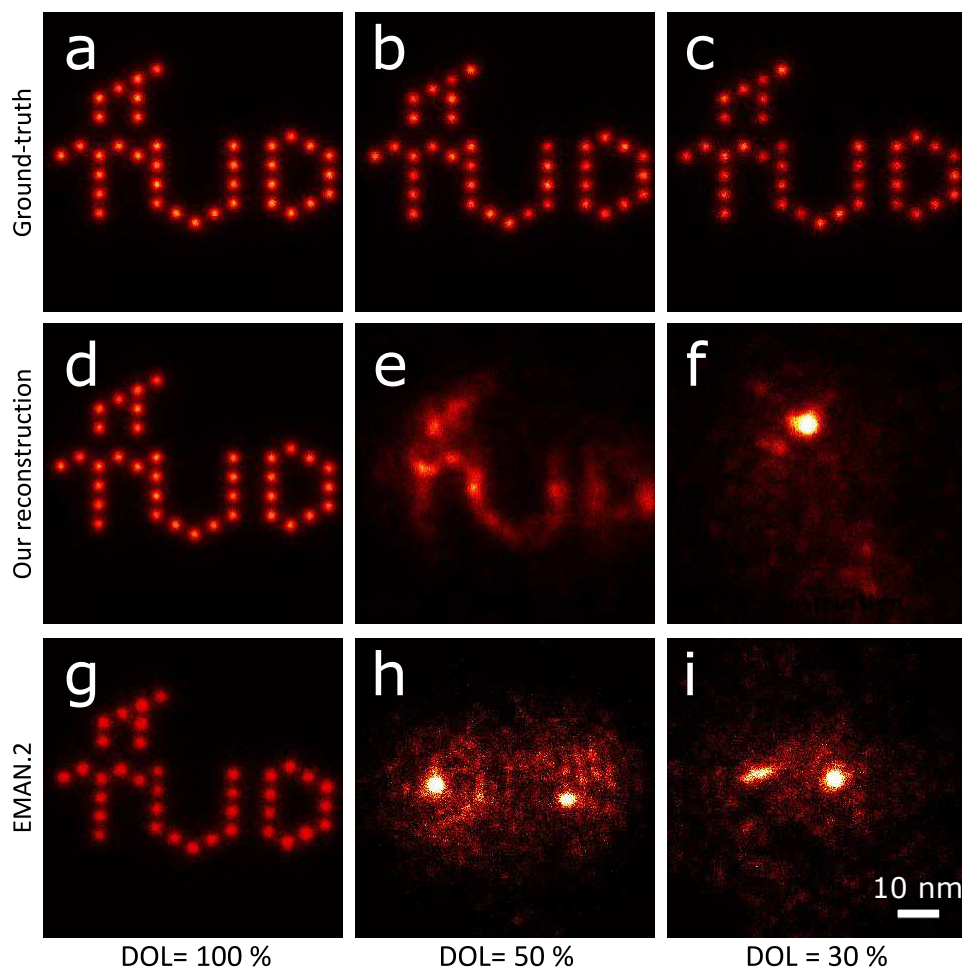


Figure A6: Particle fusion performance comparison of our method and EMAN.2 on simulated STORM datasets as a function of DOL (bleaching rate corresponding to an average of ~ 33 localizations per binding site and 5000 photons per localization event). (a-c) Groundtruth fusion of 256 particles (d-f) Our reconstructions. (g-i) Reconstructions using EMAN.2 with 71, 90 and 128 included particles (minimum of three classes for the class averaging). With the chosen bleaching rate, the average number of localizations per particle for the three datasets is similar to the corresponding simulated PAINT data in [Figure A2](#). While for 100% DOL the reconstruction of STORM data is as good as for PAINT and close to the groundtruth, successful reconstructions require a DOL of at least $\sim 50\%$. Our method outperforms EMAN.2 for all degrees of underlabeling.

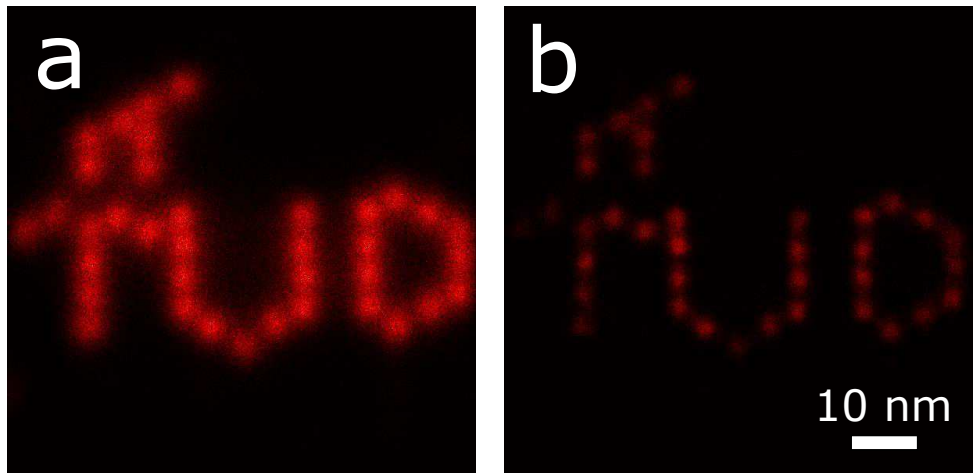


Figure A7: The effect of the filtering setting on localizations that are too far away from any other localization on the final reconstruction for the experimental 80% DOL dataset. (a) The fusion of 383 TUD logos filtered with the parameter $r = 3 \times 0.0075$ pixel size resulted in 939,707 localizations. (b) The fusion with filter parameter $r = 0.0075$ pixel size resulted in 151,729 localizations. The figures show that decreasing the neighbourhood parameter (r) will identify more localizations as false positives. While in figure (a) only 10% of the localizations are discarded, more than 75% of all localizations are identified as false positives in (b), which appears too much to be considered as a correct assessment of false positives.

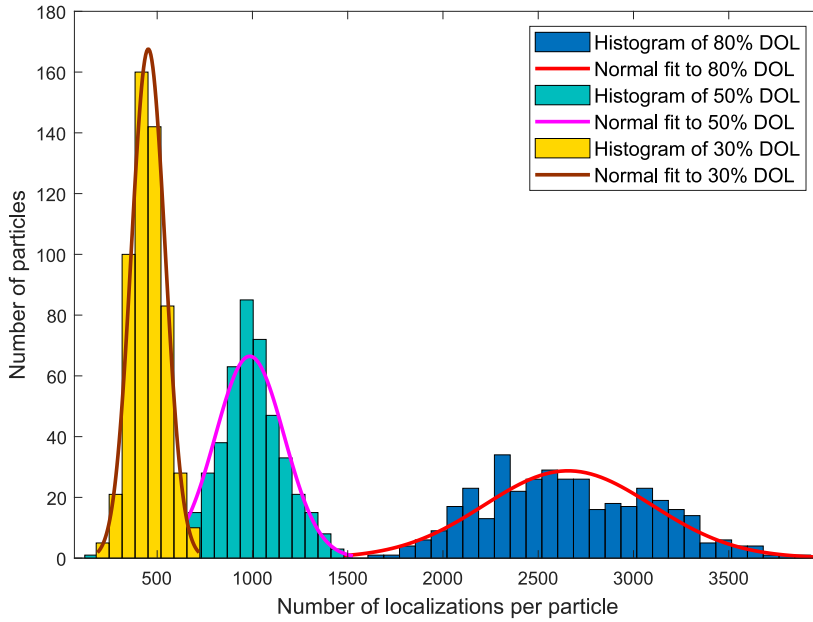


Figure A8: Histogram of the number of localizations per particle in 80%, 50% and 30% DOL datasets with fitted normal distributions (80% DOL: mean 2.66×10^3 , variance 1.94×10^5 ; 50% DOL: mean 9.85×10^2 , variance 3.24×10^4 ; 30% DOL: mean 4.53×10^2 , variance 7.74×10^3). The variance exceeds the mean as the overall distribution is a convolution of the distribution of the number of localizations per binding site (which can be assumed to be Poissonian) and the distribution of active binding sites given the average DOL.

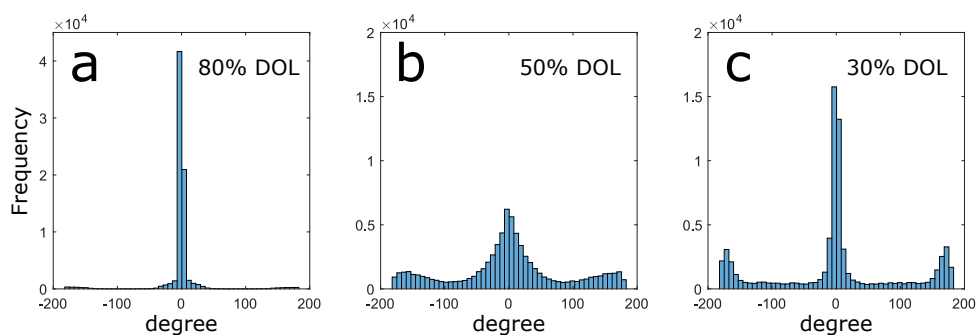


Figure A9: Histograms of the distribution of the inconsistency between the estimated relative angles after Lie-algebraic averaging and the initial relative angles from the all-to-all registration for the experimental datasets. The distribution typically is a mix of three contributions: a peak with width of a few to 20 deg around the correct angle (~ 0 degree), a peak around 180 degree, due to the close-to-symmetric shape of the 'TUD' logo, and a uniform background distribution. The fraction of erroneous pair registrations (the second and third component) increases with decreasing DOL, and is a significant fraction of the total number of pair registrations. This is the reason why the redundancy of the all-to-all registration is a necessary ingredient of the particle fusion process.

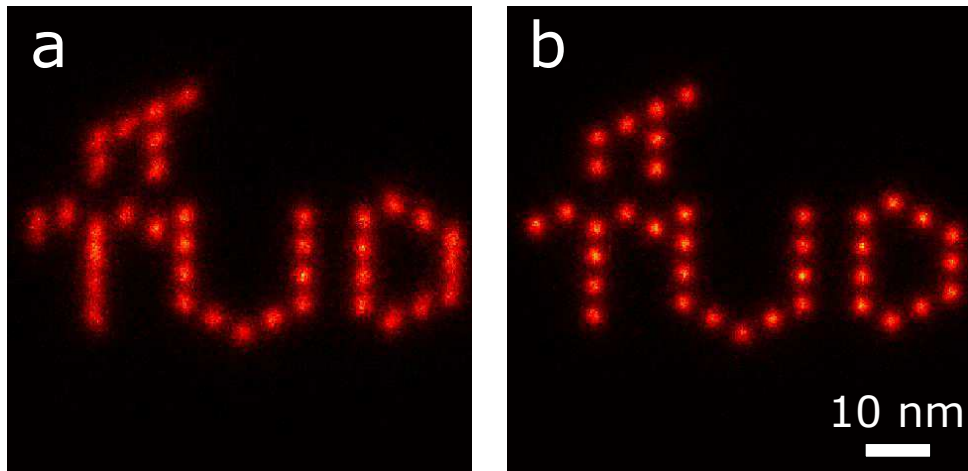


Figure A10: The effect of repeated bootstrapping registration step on 50% DOL simulated data. (a) The bootstrapping output at the first iteration. (b) The output after the second iteration. Iterating the bootstrapping step can further improve the result until convergence. For 50% DOL, the registration already converges after the second iteration.

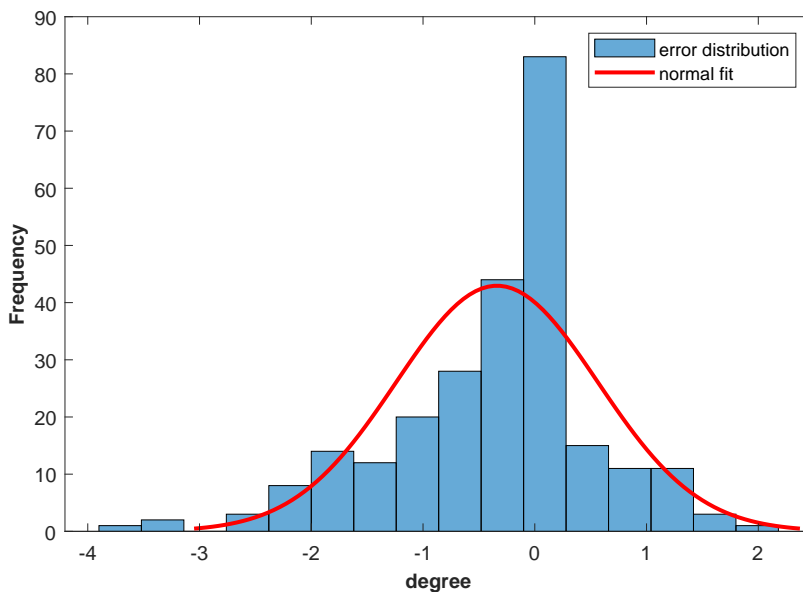


Figure A11: Histogram of the overall registration error (rotation angle) for the simulated 100% DOL dataset which includes 256 TUD logos. A normal distribution with a standard deviation of 0.9 degree (red curve) is shown for comparison. Since the length of the bounding box of the logo is 70 nm, this amount of error will maximally result in a displacement of ± 0.55 nm at the edges of the logo. This is smaller than the distance of the binding sites (5 nm) and very close to the mean localization uncertainty. Consequently, the impact of the overall outlier removal is minimal on the final reconstruction as depicted in [Figure A2g](#).

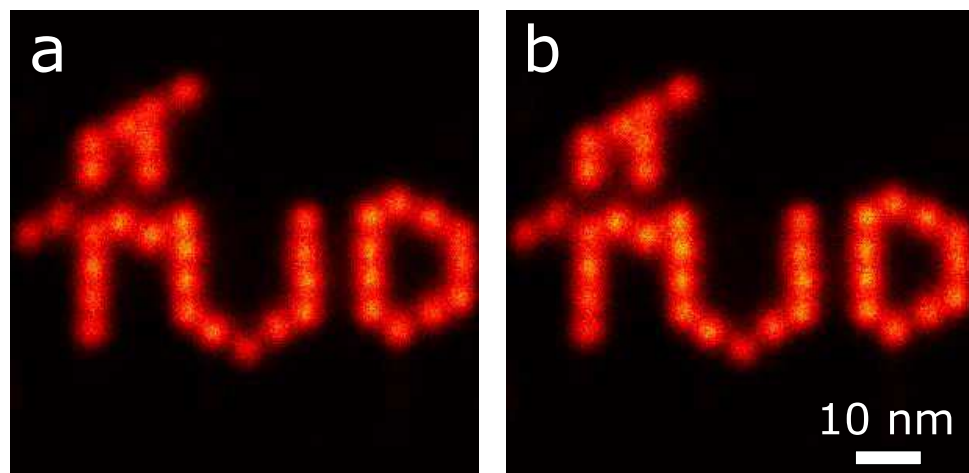


Figure A12: The effect of averaging over a subset of pair registrations on the final reconstruction for the 80% DOL experimental data. (a) The result of averaging over all 73153 elements of the all-to-all registration matrix. (b) The result of averaging over 1200 (less than 2%) elements of the all-to-all registration matrix. Both reconstructions have 788875 localizations as a result of fusing 383 TUD logos with 80% DOL. Below 2%, the reconstruction is still possible for this dataset, however, the final logo then becomes blurry especially at the edges where the effect of the registration error is severe.

3

THREE DIMENSIONAL PARTICLE AVERAGING FOR STRUCTURAL IMAGING OF MACROMOLECULAR COMPLEXES BY LOCALIZATION MICROSCOPY

We present an approach for 3D particle fusion in localization microscopy which dramatically increases signal-to-noise ratio and resolution in single particle analysis. Our method does not require a structural template, and properly handles anisotropic localization uncertainties. We demonstrate 3D particle reconstructions of the Nup107 subcomplex of the nuclear pore complex (NPC), cross-validated using multiple localization microscopy techniques, as well as two-color 3D reconstructions of the NPC, and reconstructions of DNA-origami tetrahedrons.

This chapter is based on the paper [1]. Submitted.

3.1. INTRODUCTION

Single molecule localization microscopy (SMLM) is capable of resolving biological structure at the nanometer scale. However, SMLM image resolution is ultimately limited by the density of the fluorescent labels on the structure of interest and the finite precision of each localization [2, 3]. Recently, methods for obtaining higher precision localizations have been reported, which work by either increasing the number of collected photons per molecule via e.g. cryogenic imaging [4, 5], or by introducing patterned illumination [6, 7]. The first limitation remains, however, and one approach to boosting the apparent degree of labeling (DOL) and filling in missing labels can be applied when the sample consists of many identical copies of the structure of interest (e.g. a protein complex). In this case, by combining many structures into a single superparticle, the effective labelling density is increased, and the resulting super-particle has a high number of localizations leading to a significantly improved signal-to-noise ratio and resolution.

Previous approaches to this problem can be classified as either template-based or adaptations of existing single particle analysis (SPA) algorithms originally developed for cryo-electron microscopy (EM). Template-based methods [8, 9] are computationally efficient, however, they are susceptible to template bias artefacts. Methods derived from SPA for cryo-EM have previously been adapted [10, 11] and employed to generate 3D volumes from 2D projection data. These approaches are, however, intrinsically 2D to 3D, as they assume that the raw data are projections. Recently, Shi et. al [12] also described a structure-specific method for 3D fusion, although they implicitly assume cylindrical particles and projected the volume onto top views only.

Here, we introduce a 3D particle fusion approach for SMLM which does not require, but can incorporate, a priori knowledge of the target structure. It works directly on 3D localizations, accounts for anisotropic localization uncertainties, and can perform cross-channel alignment of multicolor data. We demonstrate our method with 3D reconstructions of the Nuclear Pore Complex (NPC) obtained from three different SMLM techniques. The results exhibit a two orders of magnitude SNR amplification, and FSC-resolution values as low as 14-16 nm, which is sufficient to enable the identification of distinct proteins within a large macromolecular complex such as the NPC.

The processing pipeline is built upon our previous 2D method [13] with modifications to each step to handle 3D localizations (Figure 3.1a). Briefly, we first register all N segmented particles in pairs, which provides $N(N-1)/2$ relative registration parameters M_{ij} (3D rotation and translation from particle i to j). To find the absolute poses M_i , we map the relative poses from the group of 3D rotations and translations, $SE(3)$, to its associated Lie-algebra and then average them (see Methods section) [14]. With the absolute poses determined, we then recompute the relative transformations to perform a consistency check. This makes use of the geodesic distance on $SO(3)$ between the initial relative rotations R_{ij} and the estimates from the Lie-algebraic averaging \hat{R}_{ij} :

$$d(R_{ij}, \hat{R}_{ij}) = \frac{1}{\sqrt{2}} \left\| \log \left(\hat{R}_{ij}^{-1}, R_{ij} \right) \right\|_F. \quad (3.1)$$

Here, \log is the matrix logarithm and $\|A\|_F = \sqrt{\text{tr}(AA^T)}$ the Frobenius norm. The geodesic distance on $SO(3)$ ranges between 0 and π , we set an empirical threshold $\epsilon = 1$

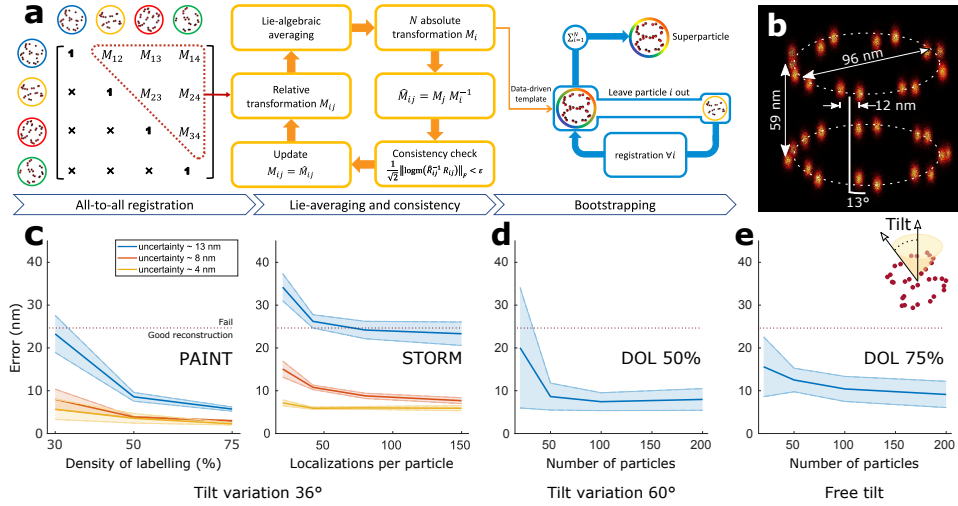


Figure 3.1: The 3D SMLM particle fusion pipeline and results of the simulation study. (a) Pair registration of all segmented particles results in relative transformations M_{ij} (translations and rotations). The redundant information in the all-to-all registration matrix is utilized for improving the registration errors by means of Lie-algebraic averaging, which results in M_i absolute transformations. The relative transformations are re-computed as $M_j M_i^{-1}$. From them, a consistency check is applied via a threshold ϵ on the rotation error to remove outlier registrations M_{ij} from the all-to-all matrix. After two iterations, this results in a data-driven template. Finally, five rounds of bootstrapping are applied to improve the final reconstruction by registering every particle to the derived template. (b) Groundtruth fusion of 100 simulated NPCs indicating the height, radius, the angular shift between the cytoplasmic and nuclear rings in the same NPC. (c) Registration error for simulated PAIN and STORM data for different degree of labeling (DOL), mean localization uncertainties ($\sigma = 4, 8$ and 13 nm) and number of localizations per particle. Successful superparticle reconstruction is possible below a registration error of 25 nm. (d) Registration error of simulated PAIN data with 50% DOL and tilt angle of 60 degrees at different number of particles per dataset. (e) Registration error of simulated PAIN data with 75% DOL and arbitrary pose at different number of particles per dataset. Solid lines indicate the mean and shaded area show the standard error of the mean ($n=15$).

radian to remove inconsistent pairwise registration entries in the all-to-all matrix. The transformations retained after the consistency check are used to generate a data-driven template. Each single particle is then registered to density-resampled versions of this template for 3-5 iterations. During this process, prior knowledge of symmetry can be incorporated. Additionally, we propose a computationally efficient means of sorting and removing outliers (see Methods section).

3.2. RESULTS

We evaluated our algorithm using simulations of the Nup107 subcomplex of the NPC (Figure 3.1c-e). Nup107 is a nucleoporin which is part of the Nup107-160 complex [15] together with eight other nucleoporins. Our groundtruth model consists of 2×16 copies of Nup107 arranged in 8 pairs on the two rings of the NPC, with a 13 deg azimuthal shift (Figure 3.1b).

The quality of registration was assessed with an error measure based on the residual registration error of the underlying binding sites (see Methods section), which is inde-

pendent of the localization precision. We found that for registration errors larger than the distance between the 8-fold symmetric subunits of the NPC rings (~ 25 nm) the reconstruction was so poor that we considered the alignment to be a failure (Figure 3.A1).

We simulated both PAINT and STORM imaging, to assess how the switching kinetics of the fluorescent labels affects the particle fusion (Figure 3.A2). For PAINT, we generated particles with a DOL of 75%, 50%, and 30%, localization uncertainties of 3, 8, and 13 nm in-plane and three times worse in the axial direction, and tilt angles spanning a range of ± 36 degrees (Figure 3.A3). For STORM, we kept the DOL fixed at a realistic value of 50% while varying the average number of localizations per particle from 20 to 150 (corresponding to different fluorophore bleaching rates), and with the same range of localization uncertainties and tilt angles as before.

For each simulation condition, we generated 15 datasets containing 100 particles each. We found that a registration error below 8-10 nm was required (Figure 3.A1) to fully resolve the sixteen pairs of Nup107 sites. For PAINT, this was achieved for a minimum DOL of 50% and a localization precision better than 8 nm (Figure 3.1c). For STORM, we observe that for high localization precision (~ 4 nm) the registration error is below 10 nm even for a low number of localizations per particle (down to 20). For a lower average localization precision of ~ 13 nm, the registration errors of all simulated STORM datasets were above 20 nm. This is similar to the error range of PAINT data at 30% DOL.

Consistent with our previous work [13] therefore, we observe that STORM imaging requires a higher DOL than PAINT to achieve a similar performance. The simulations also indicate that a high-quality reconstruction (error < 10 nm) requires at least 50-100 particles (Figure 3.1d) for PAINT data with 50% DOL. Even for unconstrained random pose variations and 75% DOL, the required number of particles for a successful registration remains relatively constant (Figure 3.1e). We applied our algorithm to experimental SMLM data of NPCs in fixed U2OS cells (Figure 3.2). Cells expressing Nup107-SNAP labeled with Alexa Fluor 647-benzylguanine were imaged with three different SMLM techniques, 3D astigmatic PAINT (Figure 3.A5), 3D astigmatic STORM [16, 17] and 4Pi STORM [18, 19]. Figure 3.2a, e and i show the results of fusing 306, 356, and 750 segmented particles for the three modalities, which had an average number of localizations per particle of 88, 70, and 58, respectively. After fusion, the FSC resolution was ~ 15 nm (isotropic, see Figure 3.A6).

We measured the distance between the cytoplasmic and nuclear rings as 60.5, 61.6 and 62.9 nm for PAINT, STORM and 4Pi STORM data, respectively (Figure 3.2b, g and l), and we determined the average radius to be 49.1, 53.2 and 51.1 nm and 50.8, 51.8, 52.8 nm for the two rings (Figure 3.2c-d, h-i and m-n).

Finally, the phase shift differences between the two rings (for analysis see Methods section) were found to be ~ 10 deg, 14 deg and 14 deg (Figure 3.2e, j and o, Figure 3.A7). These measurements are in good agreement with cryo-EM based models derived from the work of von Appen et al. [20], who found a phase shift of 14 deg, height of 59 nm, outer ring radius of 49.7 nm and inner ring radius of 46.6 nm. The experiments for NPCs in the lower nuclear membrane indicate a narrow tilt angle distribution (~ 14 degree, see Figure 3.A4), well within the tilt tolerance limit assessed from the simulations.

In a second experiment, we used multicolor 4Pi STORM to simultaneously visualize two components of the NPC (see Figure 3.3). U2OS cells expressing Nup107-SNAP were

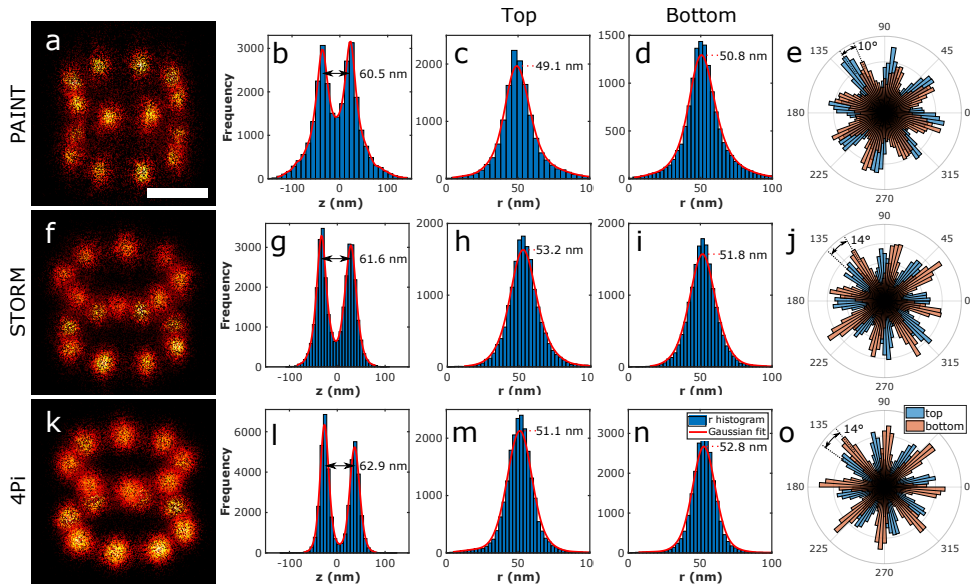


Figure 3.2: 3D Particle fusion of Nup107 acquired with different 3D localization microscopy techniques. (a) Fusion of 306 particles acquire by 3D astigmatic PAINT. (b) Histogram of the Z coordinate of localizations in the superparticle. (c) Histogram of the radius of cytoplasmic ring localizations, (d) nuclear ring. (e) Rose plot of the localization distribution over azimuthal angles for the cytoplasmic (blue) and nuclear (orange) rings of the super-particle. (f) Fusion of 356 particles acquired by 3D astigmatic STORM. (g-j) Similar to (b-e). (k) Fusion of 750 particles acquired by 4pi STORM. (l-o) Similar to (b-e).

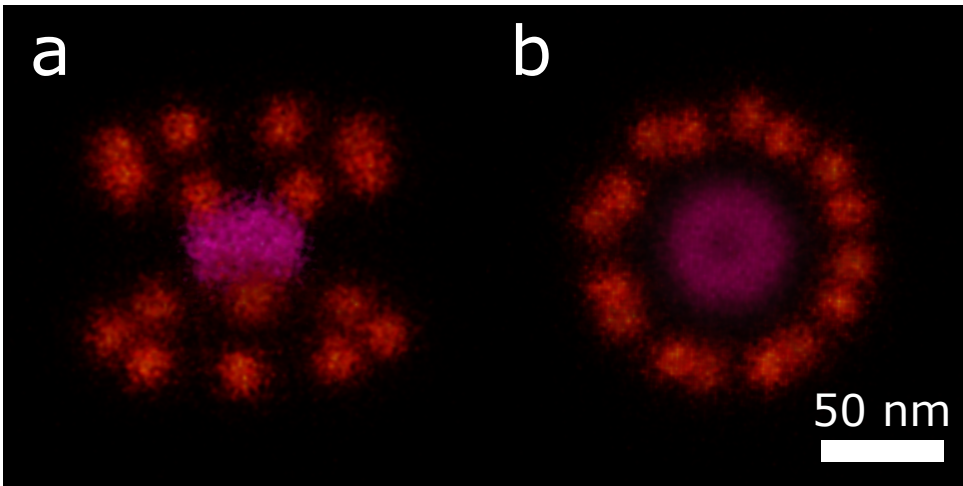


Figure 3.3: Fusion of 831 multi-colour 4pi STORM images of nuclear membranes stained for Nup107 and wheat germ agglutinin (WGA). (a) Side view. (b) Top view. Applying particle fusion on Nup107 channel (red) provides a set of absolute transformations which were subsequently used to align the corresponding WGA channel, which stains FG-repeat nucleoporins in the central channel region of the NPC (magenta).

stained with Cy5.5-benzylguanine, and also with Wheat Germ Agglutinin (WGA) conjugated to Alexa Fluor 647, which is known to bind to FG-repeat nucleoporins in the central channel region of the NPC. First, we performed particle fusion on the Nup107 localizations. Next, we applied the transformations determined from the first step to the WGA channel, and then superimposed the two color channels in a single volume with a common origin. The resulting multicolor superparticle shows the location and dimensions of the central channel of the NPC with respect to the nuclear and cytoplasmic Nup107 rings. Despite the unstructured nature of the FG-repeats, by aligning with respect to the rigid Nup107 structure, the fused WGA data maps out the spatial distribution of FG-repeats within the channel.

In a final experiment, we fused 256 tetrahedron-shaped DNA origami nanostructures acquired with PAINT (Figure 3.A8-10). The height of the tetrahedron was measured from the peak-to-peak distance of the z-histogram of the superparticle to be ~ 90 nm (Figure 3.A10d). This implies a side length of 104 nm which agrees well with the origami design of 100 nm [21].

In conclusion, we have developed a general purpose, template-free 3D particle fusion algorithm for SMLM that is robust to typical experimental conditions, and have shown its performance using simulations, the Nup107 subcomplex of the NPC for three different imaging setups, and DNA-origami tetrahedrons. By boosting the SNR of the data, our particle fusion method increases the effective spatial resolution and makes possible the reliable identification of protein locations within macromolecular complexes, thereby adding specificity to EM-SPA methods via correlative approaches. In addition, as few as 50 particles were required for accurate reconstructions, enabling the exciting possibility to detect transient, infrequently populated states.

3.3. METHODS

3.3.1. SAMPLE PREPARATION

3D ASTIGMATIC PAINT

NUP107

Cell culture U2-OS cells were passaged every other day and used between passage number 5 and 20. The cells were maintained in DMEM supplemented with 10% Fetal Bovine Serum and 1% Penicillin/Streptomycin. Passaging was performed using 1x PBS and Trypsin-EDTA 0.05%. 24 hours before immunostaining, cells were seeded on ibidi 8-well glass coverslips at 30,000 cells/well.

Cell fixation Prefixation was performed with prewarmed 2.4% Paraformaldehyde (PFA) for 20 seconds followed by the permeabilization at 0.4% Trion-X 100 for 10 seconds. Next, cells were fixed (main fixation) with 2.4% PFA for 30 minutes. After 3x rinsing with 1x PBS the cells were quenched with 50 mM Ammoniumchloride (in 1x PBS) for 4 minutes. Then, cells were washed 3x with 1xPBS followed by incubation in 1x PBS for 5 minutes twice. For SNAP-labeling, cells were incubated with 1 μ M of SNAP-ligand-modified DNA oligomer in 0.5% BSA and 1 mM DTT for 2 hours. Finally, cells were washed 3x for

5 minutes in 1x PBS, incubated with 1:1 dilution of 90 nm gold particles in 1x PBS as drift markers, washed 3 × 5 minutes and immediately imaged.

DNA origami tetrahedron

The tetrahedron DNA origami structures were formed in a one-pot reaction with a 50 μ l total volume containing 10 nM scaffold strand (p8064), 100 nM core staples, 100 nM connector staples, 100 nM vertex staples, 100 nM biotin handles, 100 nM DNA-PAINT handles, and 1400 nM biotin anti-handles in folding buffer (1x TE (5 mM Tris, 1 mM EDTA) buffer with 10 mM MgCl₂). The solution was annealed using a thermal ramp cooling from 80 to 4 °C over the course of 15 hours. After self-assembly, the structures were mixed with 1x loading dye and then purified by agarose gel electrophoresis (1.5% agarose, 0.5x TAE, 10 mM MgCl₂, 1x SYBR Safe) at 3 V/cm for 3 hours. Gel bands were cut, crushed and filled into a Freeze 'N Squeeze column and spun for 5 minutes at 1000xg at 4 °C.

3D ASTIGMATIC STORM

Samples and data for the STORM modality were prepared and acquired according to Li et al. [17].

4PI STORM

Cell culture The U2OS cells were seeded on 18 mm #1.5 round coverslips which had been sterilized in 70% ethanol, dried and washed three times with 1x PBS. All coverslips used for 4Pi-SMLM were coated with a mirror-reflective aluminum film over one quarter of their surface, for the purpose of alignment in the 4Pi microscope. Mirror coating was accomplished using a thermal evaporator at the Optics Workshop of the Max-Planck-Institute for Biophysical Chemistry, Göttingen. Seeded cells were allowed to attach overnight at 37 °C and 5% CO₂ in a cell culture incubator.

Cell fixation Cells were rinsed twice with PBS and pre-fixed with 2,4% paraformaldehyde (PFA; Electron Microscopy Sciences; cat.# 15710) in PBS (+Ca²⁺/Mg²⁺) for 30 seconds. The cells were then immediately permeabilized with 0.5% Triton X-100 (Sigma-Aldrich; cat.# T8787) in PBS (+Ca²⁺/Mg²⁺) for 10 minutes and directly fixed afterwards with 2,4% paraformaldehyde (PFA; Electron Microscopy Sciences; cat.# 15710) in PBS (+Ca²⁺/Mg²⁺) for another 30 minutes. After fixation, the samples were rinsed three times with PBS and quenched for remaining fixative with 50 mM NH₄Cl for 5 minutes. After quenching, the sample was rinsed three times with PBS and washed three times for 5 minutes with PBS. The fixed samples were immediately stained using one of the protocols described below.

NPC labeling with SNAP-tag After fixation, samples were blocked with a few drops of Image-iT FX Signal Enhancer (Thermo-Fisher; cat.# I36933) for 30 minutes. The benzylguanine (BG)-conjugated AF647 (SNAP-Surface; NEB; cat.# S9136S) was diluted to 1 μ M in blocking solution (0,5% (w/v) BSA, 1 mM DTT in 1x PBS) and incubated with the

sample for 1 hour. This was followed by a final round of three rinsing and 5 minutes washing steps.

Dual-color NPC labeling After fixation, samples were blocked with a few drops of Image-iT FX Signal Enhancer (Thermo-Fisher; cat.# I36933) for 30 minutes. Benzylguanine (BG)-conjugated Cy5.5 was synthesized and kindly provided by the Chemical Facility of the Max Plank Institute in Göttingen. The BG-Cy5.5 was diluted to 200 nM in blocking solution (0,5% (w/v) BSA, 1 mM DTT in 1x PBS) and incubated with the sample for 2 hours. Next, the sample was rinsed three times with PBS and washed three times for 5 minutes with PBS. Immediately prior to imaging, the samples were also stained with Wheat Germ Agglutinin (WGA) coupled to Alexa 647 (Thermo Fisher # W32466). First, the WGA-Alexa 647 was diluted in 1% BSA in PBS to a concentration of 0.04 $\mu\text{g}/\text{mL}$, and the sample was incubated in this solution for 5 minutes. The sample was then washed three times for 5 minutes with PBS.

3.3.2. SINGLE MOLECULE EXPERIMENTS

3D ASTIGMATIC PAINT

NUP107

Setup Fluorescence imaging was carried on an inverted microscope (Nikon Instruments, Eclipse Ti2) with the Perfect Focus System, applying an objective-type TIRF configuration with an oil-immersion objective (Nikon Instruments, Apo SR TIRF CE100, numerical aperture 1.49, Oil). A 561 nm (MPB Communications Inc., 2W, DPSS- system) laser was used for excitation. The laser beam was passed through cleanup filters (Chroma Technology, ZET561/10) and coupled into the microscope objective using a beam splitter (Chroma Technology, ZT561rdc). Fluorescence light was spectrally filtered with an emission filter (Chroma Technology, ET600/50 m and ET575lp) and imaged on a sCMOS camera (Andor, Zyla 4.2 Plus) without further magnification, resulting in an effective pixel size of 130 nm (after 2×2 binning).

Imaging Imaging was carried out using an imager strand concentration of 1 nM (P3-Cy3B) in cell imaging buffer (buffer C) 30,000 frames were acquired at 200 ms integration time. The readout bandwidth was set to 200 MHz. Laser power (@561 nm) was set to 130 mW (measured before the back focal plane (BFP) of the objective), corresponding to 0.73 kW/cm^2 at the sample plane.

Axial calibration Calibration was carried out as described earlier [15].

Tetrahedron

Setup Tetrahedron imaging experiments were carried out on an inverted Nikon Eclipse Ti microscope (Nikon Instruments) with the Perfect Focus System, attached to a Yokogawa spinning disk unit (CSU-W1, Yokogawa Electric). An oil-immersion objective (Plan Apo 100x, NA 1.45, oil) was used for all experiments. The excitation

laser (561 nm, 300 mW nominal, coherent sapphire or 532 nm, 400 mW nominal, Cobolt Samba) was directly coupled into the Yokogawa W1 unit using a lens (focal length $f = 150$ mm). The pinhole size of the disk was $50 \mu\text{m}$. As dichroic mirror, a Di01-T405/488/568/647-13x15x0.5 from Semrock or t540spxxr-uf1 from Chroma was used. Fluorescence light was spectrally filtered with emission filters (607/36 nm from Semrock or ET585/65m + ET542lp from Chroma) and imaged on an EMCCD camera (iXon 897, Andor Technologies), resulting in a pixel size of 160 nm. The power at the objective was measured to be $\sim 10\%$ of the input power.

Imaging For the tetrahedron imaging experiment (2 nM of P1-Cy3b imager in buffer B) the Andor iXon 897 with a readout bandwidth of 5 MHz at 16 bit and 5x pre-amp gain was used. The EM gain was set to 100. 30,000 frames with an integration time of 800 ms were acquired. Imaging was performed using the Yokogawa W1 spinning disk unit with an excitation intensity of $\sim 226 \text{ W/cm}^2$ at 561 nm at the sample (laser was set to $\sim 38 \text{ mW}$). No additional magnification lens was used resulting in an effective pixel size of 160 nm.

Calibration 3D images were acquired using a plan-convex cylindrical lens with a focal length of $f = 0.5$ m, ~ 2 cm away from the camera chip. The calibration was done as in earlier studies. For the processing of the data the software package Picasso [22] was used.

3D ASTIGMATIC STORM

Samples and data for the STORM modality were prepared and acquired according to Li et al. [17]. In short, homozygous Nup107-SNAP U2-OS cell lines were fixed and labeled with Alexa Fluor 647 benzylguanine and imaged on a custom-built setup that contains a cylindrical lens in the emission path for astigmatic 3D localization. The data were fitted using an experimental PSF model calibrated using a z-stack of beads that were immobilized on the coverslip [16]. Subsequently, fitting errors induced by the refractive index mismatch were corrected based on a calibration of beads immobilized in a gel [17].

4PI STORM

Setup The design of the 4Pi microscope was based on an earlier design published by Aquino et al. [18], which was then extensively modified to achieve higher image quality and usability. Specifically, the design was changed to incorporate feedback systems to maintain the sample focus position, higher NA objectives to collect more light, a completely redesigned sample stage allowing for fast and reliable sample mounting and linear translation when adjusting the sample position, a redesigned 4Pi image cavity allowing for maintenance of the beam path alignment, and new acquisition and control software to allow accurate control of the instruments involved in the system stabilization and acquisition of the raw image data. The laser illumination sources used for STORM imaging included a red laser for imaging (642nm CW, 2W, MPB Communications Inc.) and a UV laser for molecule re-activation (405nm CW, 100mW, Coherent). Excitation light was controlled and modulated either directly via the laser controller or

via an acousto-optic tunable filter (AA Opto Electronic). Variable angle TIRF or near-TIRF illumination was achieved by coupling all light sources through an optical fiber, whose output was positioned in an optical plane conjugate to the objective lens back focal plane. By placing the output of the fiber on a motorized translation stage, the illumination angle could be continuously varied for optimal signal to background ratio. The 4Pi microscope cavity was based on two high-NA objective lenses (Olympus, 100x, silicone oil immersion, NA 1.35). One objective was fixed in position on a mounting block while the other was adjustable in three dimensions using a 3-axis piezo stage (Physik Instrumente, P-733.3). The adjustable objective was also adjustable in tip/tilt and XYZ via micrometer screws for coarse positioning and alignment. Illumination and control beams were introduced into the 4Pi cavity and brought out again via dichroic mirrors (ZT405-488-561-640-950RPC, Chroma). The detected fluorescence from the two objectives was recombined at a 50:50 beam-splitter (Halle). Prior to the beam-splitter each detected beam passed through a quarter wave plate (Halle) and a custom Babinet-Soleil compensator made of quartz and BK7 glass, one of which with an adjustable thickness of quartz glass, which allowed a precise phase delay to be introduced between the P- and S-polarized fluorescence light. The remainder of the detection path consisted of an optical relay to crop and focus the overlaid P- and S- polarized images onto four quadrants of an EMCCD camera (Andor Ixon DU897) as previously described. Before the camera, the light was filtered with fluorescence emission filters (Semrock LP647RU, Semrock FF01-770SP) and optionally a dichroic mirror (Semrock FF685-Di02) which allowed the fluorescence in one polarization channel to be filtered selectively for two-color 4Pi-SMLM imaging. Control systems included the sample focus control and the objective alignment control, and each of these was based on an infra-red laser beam introduced into the 4Pi cavity. The sample focus control was based on a design similar to that used in a standard STORM microscope: an infrared beam (830nm laser diode, Thorlabs) was reflected from the sample-glass interface, and the position of the reflected beam was detected on a photodetector. Fine control of the sample position was maintained with a linear piezo stage (Physik Instrumente, P-752) mounted underneath the top section of the three-axis linear stage used for sample positioning (Newport, M-462-XYZ-M). For the objective alignment control, a second infra-red beam (940nm laser diode, Thorlabs) was collimated and passed through the two objective lenses, focusing at the sample plane. Any motion of the two objectives with respect to each other resulted in a lateral shift in the transmitted beam, or a change in the collimation of the transmitted beam. The lateral shift was continuously monitored via a quadrant photodiode, and the transmitted beam collimation was monitored by splitting the beam and focusing it onto two pinholes positioned on either side of the focus, with photodetectors behind each pinhole. These signals were measured using a DAQ card (National Instruments), and a software-based feedback loop was then used to adjust the position of the movable objective lens to keep it aligned with the fixed objective lens. All microscope control and data acquisition were performed using custom software written in Labview (National Instruments).

Imaging The sample was illuminated with 642 nm excitation light in order to switch off the fluorophores and cause them to blink stochastically. The emitted light was filtered spectrally (see above) and detected at the EMCCD camera, running at

a frame rate of 101 Hz. Typically, 100000 image frames were acquired in a single measurement. During the experiment, the power of the 405 nm laser was manually adjusted to re-activate the fluorophores and keep the number of localizations per frame constant. Optical stabilization of the z-focus (focus-lock) was engaged before starting each recording, in order to minimize sample drift during the measurement. Prior to each set of 4Pi measurements, images of a fluorescent bead located on the sample were recorded as the bead was scanned in the Z-dimension, in order to create a calibration scan which was used in post-processing analysis of the 4Pi STORM image data. For all experiments, images of beads located at different positions in the sample plane were recorded, in order to generate a coordinate mapping which allowed the coordinate systems of the different image channels to be mapped onto each other.

Image reconstruction STORM image analysis and reconstruction follows a standard approach based on peak finding and localization [23]. Two color imaging via the ratiometric method was analyzed as described previously [18, 24]. Correction of sample drift in post-processing was done based on image correlation of the 3D STORM data with itself over multiple time windows. STORM images were rendered as summed Gaussian peaks with a Gaussian width approximately equal to the previously measured localization precision (typically 3.5 nm in X, Y, and Z).

3.3.3. DATA FUSION PIPELINE

Our data fusion framework is largely the same as our earlier work [13] with 3D instead of 2D localization data. The anisotropic localization precision in 3D is naturally incorporated into the pair-wise alignment procedure using the Bhattacharya distance. We have to replace the consistency evaluation as rotations in 2D can be characterized by one in-plane angle only and therefore a straightforward threshold can be applied to the angle difference. In 3D, the three Eulerian angles are required to describe a rotation which complicates matter significantly as different rotations do not commute. To this end we used the geodesic distance equation Equation 3.1 on $SO(3)$ as a measure for the dissimilarity between different rotations. Next to this necessary change for applying the framework in 3D, we have also made two other modifications to the earlier pipeline.

Incorporation of symmetry For symmetric structures and in the case of underlabeling or a nonuniform distribution of localizations per binding sites (e.g. in STORM), the hotspot problem reported earlier [13] is unavoidable. The registration always tries to match dense regions of the structure and consequently the unbalanced occupancy of sites is reinforced in the process. We overcome this problem by properly incorporating prior knowledge about the symmetry group of the structure. For NPC, which has an eight-fold rotational symmetry (2D cyclic group \mathcal{C}_8) around the rotation axis through the center of the cytoplasmic and nuclear rings, we randomly added integer multiples of $2\pi/8$ to the alignment angles of the particles at each iteration of the bootstrapping. This subsequently results in a uniform distribution of localizations over the binding sites. It is worth mentioning that this approach is different than what is done in single particle averaging in EM [25] and in the method of Sieben et al. [11] where the asymmetrical subunit of the particles is replicated to generate a symmetric structure based on the given

symmetry group. In our approach the final reconstruction is mathematically not symmetric, but the symmetry is used to resolve the hotspot problem. This approach can easily be adapted to other simple point groups such as cyclic \mathcal{C}_n and dihedral \mathcal{D}_n groups given the axis (or axes) of rotation(s).

Outlier particle removal In our earlier work [13], we kept all initially picked particles for the final superparticle. We only removed many of the bad registrations from the all-to-all matrix as long as the graph stays connected. In practice, however, it happens that the segmented particle set contains “outliers” that are either not a particle but background or just very low-quality particles. We propose a simple and efficient method for excluding outliers with small computational cost. After the bootstrapping step, we construct an $N \times N$ matrix with elements equal to the Bhattacharya cost function for all pairs of aligned particles (Figure 3.A11a). We sum over the columns (or rows) of this similarity matrix to assign a single score to each individual particle. If all particles are of good quality, these scores should be similar in magnitude. For outlier particles, however, we observe that the histogram of scores has an extended tail. We identify outliers as particles with scores are more than three scaled median absolute deviations (MAD) away from the median (Figure 3.A11b). This outlier particle removal only works properly if most of the segmented particles are of good quality and the particle fusion has not failed. The visual experience of the final reconstruction is barely affected for the examples shown in Figure 3.2, however, the best and worst particles demonstrate how this approach can rank the quality of the included particles (Figure 3.A11c-d).

3.3.4. SIMULATION SETUP

Our groundtruth model consists of 2×16 copies of NUP107 arranged in 8 pairs on the cytoplasmic and nuclear ring of the NPC with ~ 13 degree of azimuthal shift (Figure 3.1b). PAINT and STORM switching kinetics were simulated as earlier described [13]. For each parameter setting, we generated 15 datasets containing 100 particles each.

3.3.5. REGISTRATION ERROR MEASURE IN SIMULATIONS

To assess the performance of the method on simulated data, we devised an error metric which is independent of the shape of the groundtruth superparticle, does not have a global offset problem i.e. any transformation of the whole ensemble of particles gives the same error, can solve the symmetry ambiguity, is not impaired by underlabeling and has the same unit as the localization data. The error is the averaged Euclidean distance between corresponding binding sites after applying the data fusion process. This works in simulation only as there we know the ground truth and thus, we can establish point-correspondence between binding sites. This measures the registration error, however, if we would do the same with the localization data, we would get a convoluted compound of registration error and localization error and an overweighting of sites with many localizations. In Figure 3.A12 and Figure 3.A13, we illustrate the process. We find the point correspondence by measuring the distance for all possible combinations of binding sites and then report the minimum as the registration error between the two particles. Figure 3.A13 demonstrates such combinations for a simplified NUP structure with $K = 16$ designed binding sites. Mathematically, the registration error of N aligned particles is

computed as follows:

$$\text{error} = \frac{2}{N(N-1)} \left(\sum_{m=1}^{N-1} \sum_{n=m+1}^N \min_{i=1, \dots, K} \sqrt{\frac{1}{K} \sum_{j=1}^K \|x_m(j) - x_n(\text{mod}(i+j, K))\|^2} \right) \quad (3.2)$$

in which x_m is the localization data (3D coordinate) of the particle m from the set of all particles and “mod” is the modulo operator. The double sum sums over all pairs of particles and the sum over all possible correspondence of the binding sites for the current pair of particles.

3.3.6. POSE VARIATION IN SIMULATION

In simulation we allow full orientational freedom, which is not encountered in our experiment. Due to the linear approximation of the exponential mapping from $SO(3)$ to the Lie-algebra representation, averaging on $SE(3)$ works only if the pose variation of particles is within a certain range. Therefore, fusion of particles with arbitrary poses can result in clusters of particles which are aligned within clusters but not across them (Figure 3.A14a-b). We developed a work-around for this problem as follows. As for outlier removal routine, we first compute the similarity matrix. Then, we subtract each row (or column) from the self-similarity (the Bhattacharya distance of a particle from itself) of the corresponding particle to convert the matrix into a dissimilarity matrix. We then use multidimensional scaling (MDS) [26] to translate the information about the pairwise distances between the N particles into a constellation of N points in Cartesian two-dimensional space. Subsequently, we use k -means clustering to identify clusters of particles (Figure 3.A14c). The user can easily identify the number of clusters in the MDS plot and for the current experiments we set it empirically to 3-4. Since the particles within each cluster are already well aligned (Figure 3.A14d-f), one can do a pairwise registration at the end to align all or some of the identified clusters.

3.3.7. ANALYSIS OF NPC STRUCTURAL PARAMETERS

NPCs are embedded in the nuclear membrane and their tilt axis aligns reasonably with the optical axis (normal distribution with about zero mean, Figure 3.A4). Consequently, the Lie-algebra always aligns the particles with the x-y plane for experimental data. A moment analysis of the super-particle is used to align the average pose with the principle planes (xy, xz, yz and etc.), i.e. aligning the symmetry axis of the NPC superparticle with the z-axis. The distance between the upper and lower rings of the NPCs is estimated by first computing the histogram of the z coordinate of the localization data in the superparticle. Then, a kernel-smoothing distribution with a bandwidth of 4 nm is fitted to the histogram and, finally, the distance between the two peaks of the fit is computed (Figure 3.2b, g and l). The radius of the two rings is measured by separating the localization data of the superparticle in two halves using a segmentation threshold which is computed as the local minimum of the z coordinate histogram. Then, the x and y coordinates of the localization data are transformed to two-dimensional polar coordinates (r, θ). The peak of the histogram of the r component of the localizations defines the radius of the rings (Figure 3.2c-d, h-i and m-n). The angular shift between the two rings of the NUP107 is estimated by, first fitting the function $b_0 + b_1 \sin(8\theta + b_2)$ to the angu-

lar components of the localization data in each ring. The iterative least squares method is used for this nonlinear regression model to find the unknown coefficients b_0 , b_1 and b_2 . Then, the difference between the fitted b_2 parameters for the two rings defines the angular phase difference (Figure 3.A7).

REFERENCES

- [1] Hamidreza Heydarian, Adrian Przybylski, Florian Schueder, Ralf Jungmann, Ben van Werkhoven, Jan Keller-Findeisen, Jonas Ries, Sjoerd Stallinga, Mark Bates, and Bernd Rieger. Three dimensional particle averaging for structural imaging of macromolecular complexes by localization microscopy. *bioRxiv*, 2019.
- [2] M. Bates, B. Huang, and X. Zhuang. Super-resolution microscopy by nanoscale localization of photo-switchable fluorescent probes. *Curr Opin Chem Biol*, 12(5): 505–14, 2008.
- [3] Robert P. J. Nieuwenhuizen, Keith A. Lidke, Mark Bates, Daniela Leyton Puig, David Grünwald, Sjoerd Stallinga, and Bernd Rieger. Measuring image resolution in optical nanoscopy. *Nature methods*, 10(6), 2013.
- [4] W. Li, S. C. Stein, I. Gregor, and J. Enderlein. Ultra-stable and versatile wide-field cryo-fluorescence microscope for single-molecule localization with sub-nanometer accuracy. *Opt Express*, 23(3), 2015.
- [5] Siegfried Weisenburger, Daniel Boening, Benjamin Schomburg, Karin Giller, Stefan Becker, Christian Griesinger, and Vahid Sandoghdar. Cryogenic optical localization provides 3d protein structure data with angstrom resolution. *Nature Methods*, 14, 2017.
- [6] F. Balzarotti, Y. Eilers, K. C. Gwosch, A. H. Gynna, V. Westphal, F. D. Stefani, J. Elf, and S. W. Hell. Nanometer resolution imaging and tracking of fluorescent molecules with minimal photon fluxes. *Science*, 355(6325), 2017.
- [7] Jelmer Cnossen, Taylor Hinsdale, Ramsus Thorsen, Florian Schueder, Ralf Jungmann, Carlos S Smith, Bernd Rieger, and Sjoerd Stallinga. Localization microscopy at doubled precision with patterned illumination. *BioRxiv*, 2019.
- [8] Anna Löschberger, Sebastian van de Linde, Marie-Christine Dabauvalle, Bernd Rieger, Mike Heilemann, Georg Krohne, and Markus Sauer. Super-resolution imaging visualizes the eightfold symmetry of gp210 proteins around the nuclear pore complex and resolves the central channel with nanometer resolution. *Journal of Cell Science*, 125(3), 2012.
- [9] Jordi Broeken, Hannah Johnson, Diane S. Lidke, Sheng Liu, Robert P. J. Nieuwenhuizen, Sjoerd Stallinga, Keith A. Lidke, and Bernd Rieger. Resolution improvement by 3d particle averaging in localization microscopy. *Methods and Applications in Fluorescence*, 3(1), 2015.

- [10] Desirée Salas, Antoine Le Gall, Jean-Bernard Fiche, Alessandro Valeri, Yonggang Ke, Patrick Bron, Gaetan Bellot, and Marcelo Nollmann. Angular reconstitution-based 3d reconstructions of nanomolecular structures from superresolution light-microscopy images. *Proceedings of the National Academy of Sciences*, 114(35), 2017.
- [11] Christian Sieben, Niccolò Banterle, Kyle M. Douglass, Pierre Gönczy, and Suliana Manley. Multicolor single-particle reconstruction of protein complexes. *Nature Methods*, 15(10), 2018.
- [12] X. Shi, 3rd Garcia, G., Y. Wang, J. F. Reiter, and B. Huang. Deformed alignment of super-resolution images for semi-flexible structures. *PLoS One*, 14(3), 2019.
- [13] Hamidreza Heydarian, Florian Schueder, Maximilian T. Strauss, Ben van Werkhoven, Mohamadreza Fazel, Keith A. Lidke, Ralf Jungmann, Sjoerd Stallinga, and Bernd Rieger. Template-free 2d particle fusion in localization microscopy. *Nature Methods*, 15(10), 2018.
- [14] V. Govindu. Lie-algebraic averaging for globally consistent motion estimation. In *2013 IEEE Conference on Computer Vision and Pattern Recognition*, volume 1. IEEE Computer Society, jul 2004.
- [15] Jervis Vermal Thevathasan, Maurice Kahnwald, Konstanty Cieliski, Philipp Hoess, Sudheer Kumar Peneti, Manuel Reitberger, Daniel Heid, Krishna Chaitanya Kasuba, Sarah Janice Hoerner, Yiming Li, Yu-Le Wu, Markus Mund, Ulf Matti, Pedro Matos Pereira, Ricardo Henriques, Bianca Nijmeijer, Moritz Kueblbeck, Vilma Jimenez Sabinina, Jan Ellenberg, and Jonas Ries. Nuclear pores as versatile reference standards for quantitative superresolution microscopy. *Nature Methods*, 16(10), 2019.
- [16] Yiming Li, Markus Mund, Philipp Hoess, Joran Deschamps, Ulf Matti, Bianca Nijmeijer, Vilma Jimenez Sabinina, Jan Ellenberg, Ingmar Schoen, and Jonas Ries. Real-time 3d single-molecule localization using experimental point spread functions. *Nature Methods*, 15, 2018.
- [17] Yiming Li, Yu-Le Wu, Philipp Hoess, Markus Mund, and Jonas Ries. Depth-dependent psf calibration and aberration correction for 3d single-molecule localization. *Biomedical Optics Express*, 10(6), 2019.
- [18] D. Aquino, A. Schonle, C. Geisler, C. V. Middendorff, C. A. Wurm, Y. Okamura, T. Lang, S. W. Hell, and A. Egner. Two-color nanoscopy of three-dimensional volumes by 4pi detection of stochastically switched fluorophores. *Nat Methods*, 8(4), 2011.
- [19] Gleb Shtengel, James A. Galbraith, Catherine G. Galbraith, Jennifer Lippincott-Schwartz, Jennifer M. Gillette, Suliana Manley, Rachid Sougrat, Clare M. Waterman, Pakorn Kanchanawong, Michael W. Davidson, Richard D. Fetter, and Harald F. Hess. Interferometric fluorescent super-resolution microscopy resolves 3d cellular ultrastructure. *Proceedings of the National Academy of Sciences*, 106(9), 2009.

- [20] A. von Appen, J. Kosinski, L. Sparks, A. Ori, A. L. DiGiulio, B. Vollmer, M. T. Mackmull, N. Banterle, L. Parca, P. Kastritis, K. Buczak, S. Mosalaganti, W. Hagen, A. Andres-Pons, E. A. Lemke, P. Bork, W. Antonin, J. S. Glavy, K. H. Bui, and M. Beck. In situ structural analysis of the human nuclear pore complex. *Nature*, 526(7571), 2015.
- [21] Florian Schueder, Juanita Lara-Gutiérrez, Brian J. Beliveau, Sinem K. Saka, Hiroshi M. Sasaki, Johannes B. Woehrstein, Maximilian T. Strauss, Heinrich Grabmayr, Peng Yin, and Ralf Jungmann. Multiplexed 3d super-resolution imaging of whole cells using spinning disk confocal microscopy and dna-paint. *Nature Communications*, 8(1), 2017.
- [22] Joerg Schnitzbauer, Maximilian T. Strauss, Thomas Schlichthaerle, Florian Schueder, and Ralf Jungmann. Super-resolution microscopy with dna-paint. *Nature Protocols*, 12(6), 2017.
- [23] M. Bates, S. A. Jones, and X. Zhuang. Stochastic optical reconstruction microscopy (storm): a method for superresolution fluorescence imaging. *Cold Spring Harb Protoc*, 2013(6), 2013.
- [24] I. Testa, C. A. Wurm, R. Medda, E. Rothermel, C. von Middendorf, J. Folling, S. Jakobs, A. Schonle, S. W. Hell, and C. Eggeling. Multicolor fluorescence nanoscopy in fixed and living cells by exciting conventional fluorophores with a single wavelength. *Biophys J*, 99(8), 2010.
- [25] Joachim Frank. *Three-dimensional electron microscopy of macromolecular assemblies: visualization of biological molecules in their native state*. Oxford University Press, 2006.
- [26] A. Mead. Review of the development of multidimensional scaling methods. *Journal of the Royal Statistical Society. Series D (The Statistician)*, 41(1), 1992.

3.A. APPENDIX

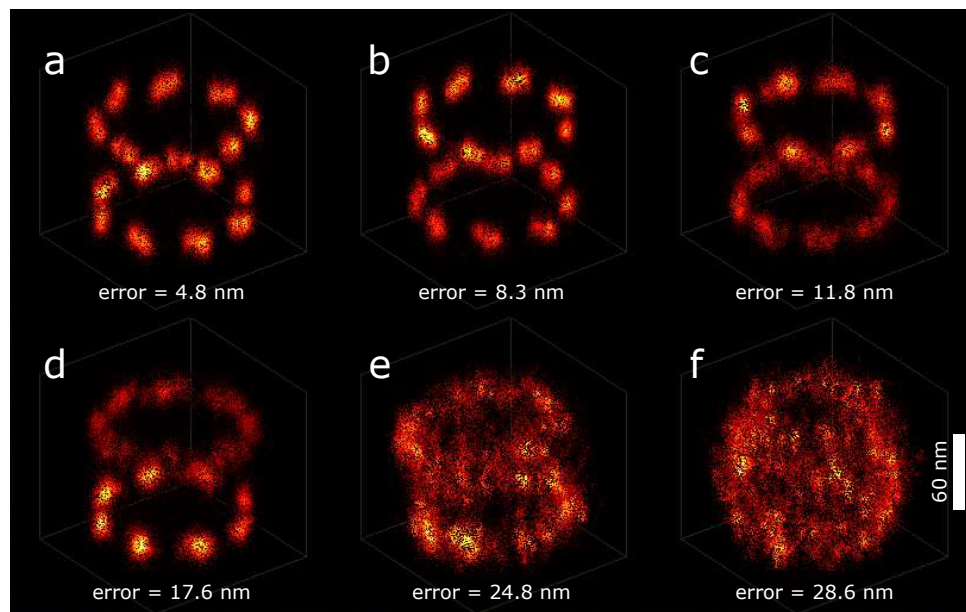


Figure 3.A1: Particle fusion error for different reconstructions of a simulated STORM dataset. (a-f) Each reconstruction is the result of fusing 100 simulated particles with an average localization uncertainty of 4 nm and 50% DOL. From top to bottom and left to right, the error is increasing which also visually matches the quality of the reconstructions. For the error less than ~ 10 nm (a-b), the double blobs are still recognizable. For larger error as in (c-d), the double blobs merge into a single blob and for errors above ~ 20 nm the reconstructions lose the geometrical features of the groundtruth.

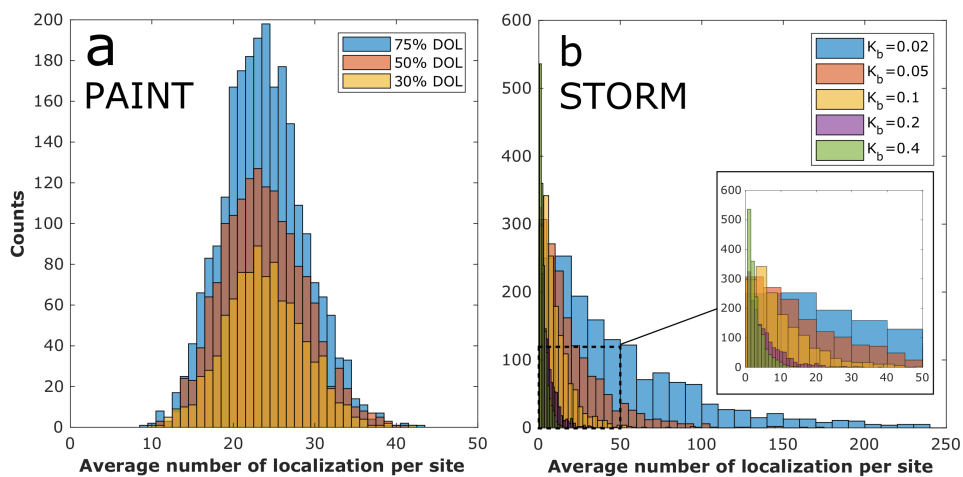


Figure 3.A2: Statistics of localizations per binding sites for (a) PAINT and (b) STORM simulations. For PAINT particles, the distribution of localizations per site follows a Gaussian distribution while for STORM it is a Poisson. In case of STORM data, higher bleaching rate result in fewer localization per sites and a narrower bandwidth for the distribution.

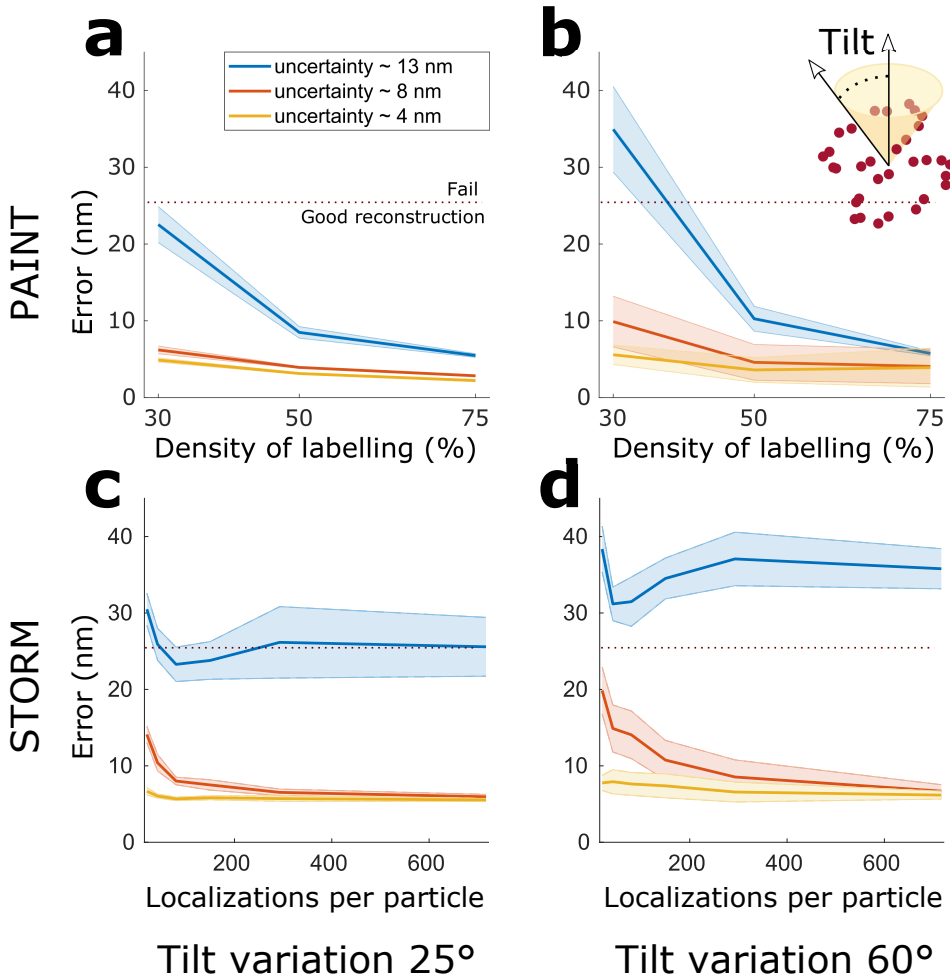


Figure 3.A3: Particle fusion error for the alignment of PAINT and STORM SLM images of simulated NUP107 particles with different initial tilt variations. (a-b) Particle fusion error of simulated PAINT data for different DOLs and for two range of tilt variations. (c-d) Particle fusion error of simulated STORM data for different number of localizations per particle (proportional to bleaching rate) and for two range of tilt variations. The particle fusion performance is getting slightly worse by increasing the tilt variations but in general it is quite stable even at high tilt angle range of 60 degree

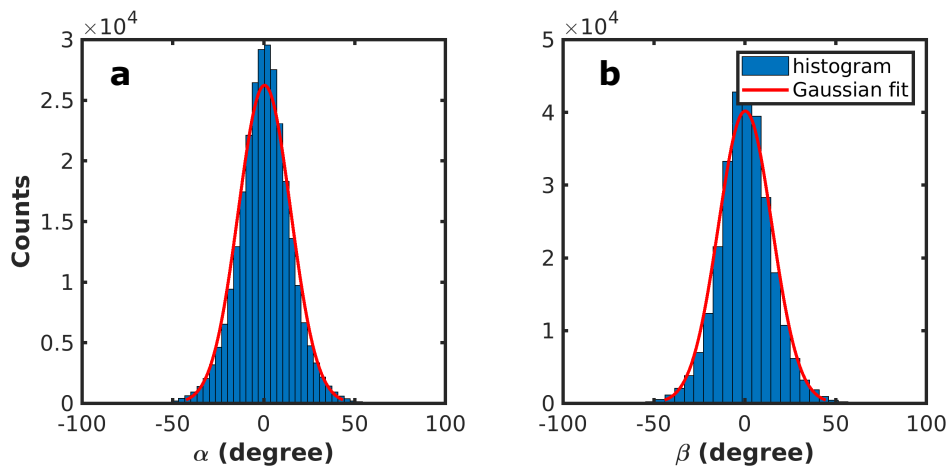


Figure 3.A4: Tilt variations of the 4Pi experimental particles. (a-b) The histograms of the Euler angles α and β (rotation around x and y axis) expressing the tilt variations of the unaligned particles with respect to each other. Both histograms fit a normal distribution with a standard deviation of 14 degree.

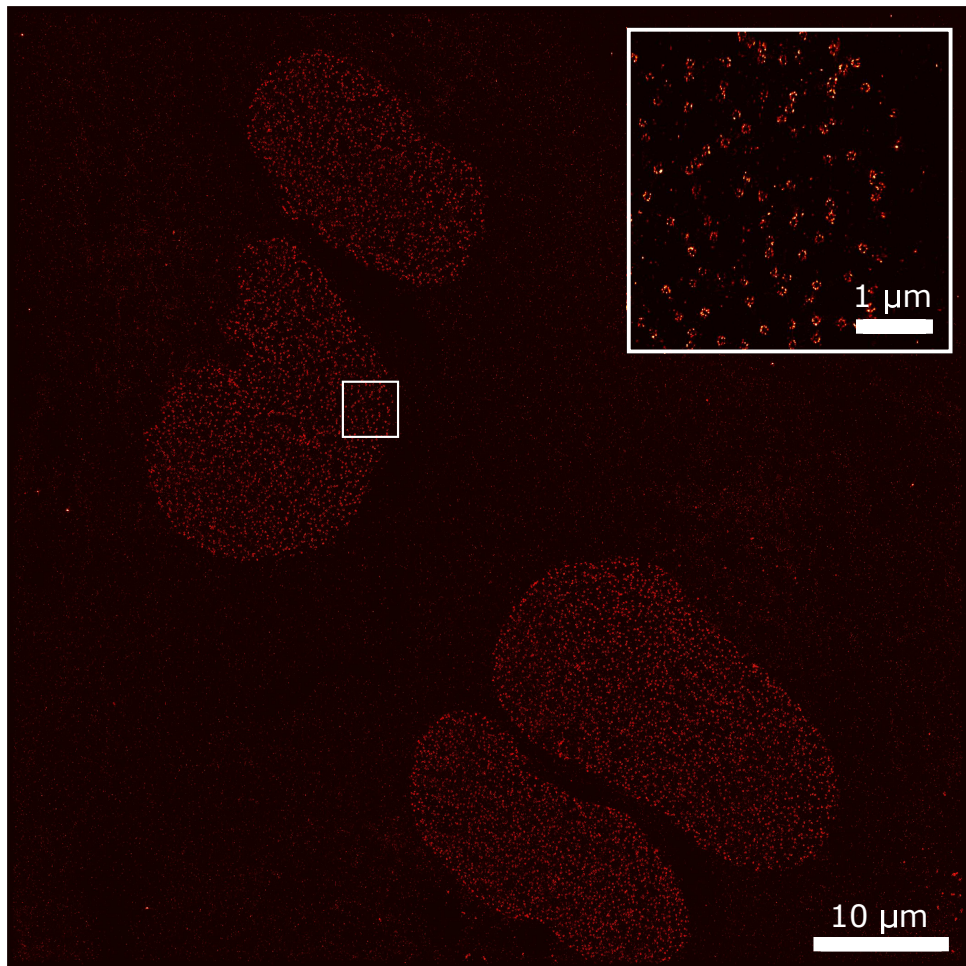


Figure 3.A5: Whole field of view of SNAP-Tag labelled NUP107 proteins for DNA-PAINT imaging. The field of view shows the nuclei of four U2OS cells. The insert in the top-right corner presents a zoom in into the highlighted area.

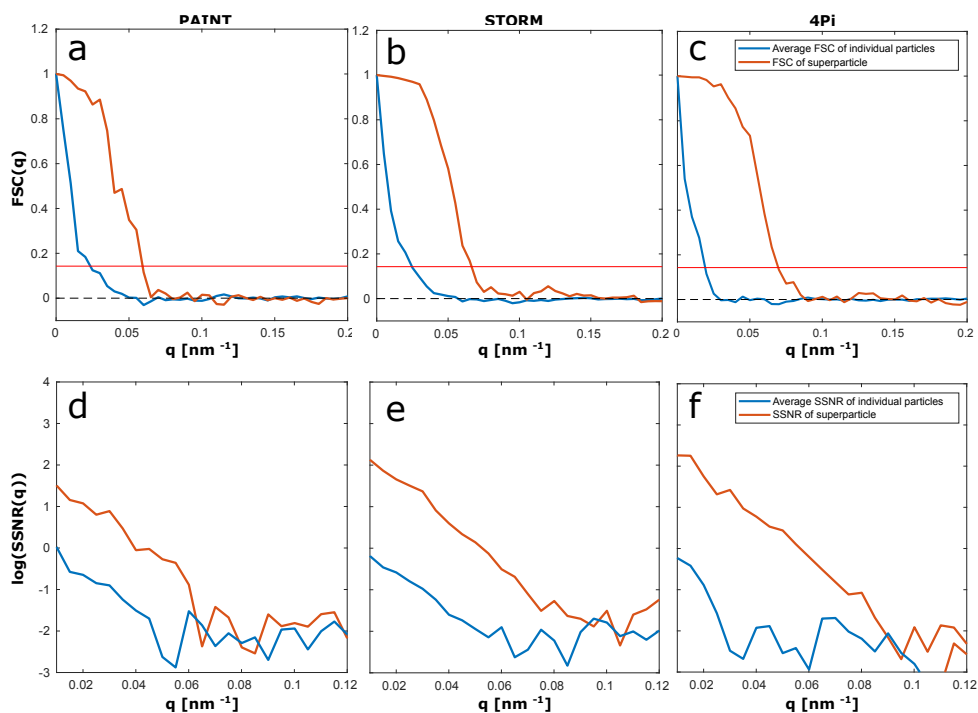


Figure 3.A6: Fourier shell correlation¹ (FSC) and spectral signal-to-noise ratio (SSNR) curves for the initial particles and the corresponding super-particles of 3D astigmatic PAIN^T, 3D astigmatic STORM and 4Pi STORM data. (a-c) The FSC curves show the resolution improvement from 42.6, 40.5, and 52.2 nm to 16.6, 15.1 and 14.2 nm for the three reconstructions respectively. (d-f) The SSNR curves show about two orders of magnitude improvement in spectral signal-to-noise ratio over. These values are in good accordance with the visual quality of the super-particles. From these FSC values it is also clear that the dimers cannot be resolved which are at 12 nm distance according to the EM model. The FSC/SSNR curves for individual particles averages (blue) are computed between pairs of individual particles and then averaged. SSNR is computed as follows $SSNR = FSC / (1 - FSC)$.

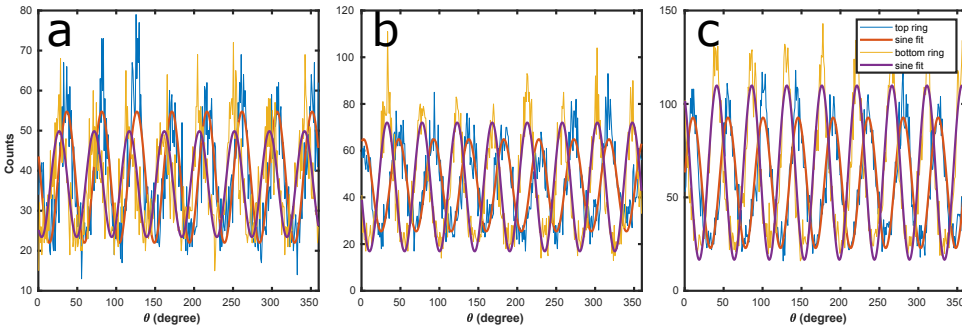


Figure 3.A7: The distribution of the localizations over azimuthal angle and the fitted sine function for the super-particles in Figure 3.2. (a) PAINt reconstruction. (b) STORM reconstruction. (c) 4Pi reconstruction. In order to find the phase shift between the cytoplasmic and nuclear rings, we fit a sine function to the azimuthal angles of the localization data points in each ring. The difference in the phases of the fitted sine function for each reconstruction defines the azimuthal phase shift of the two rings.

3

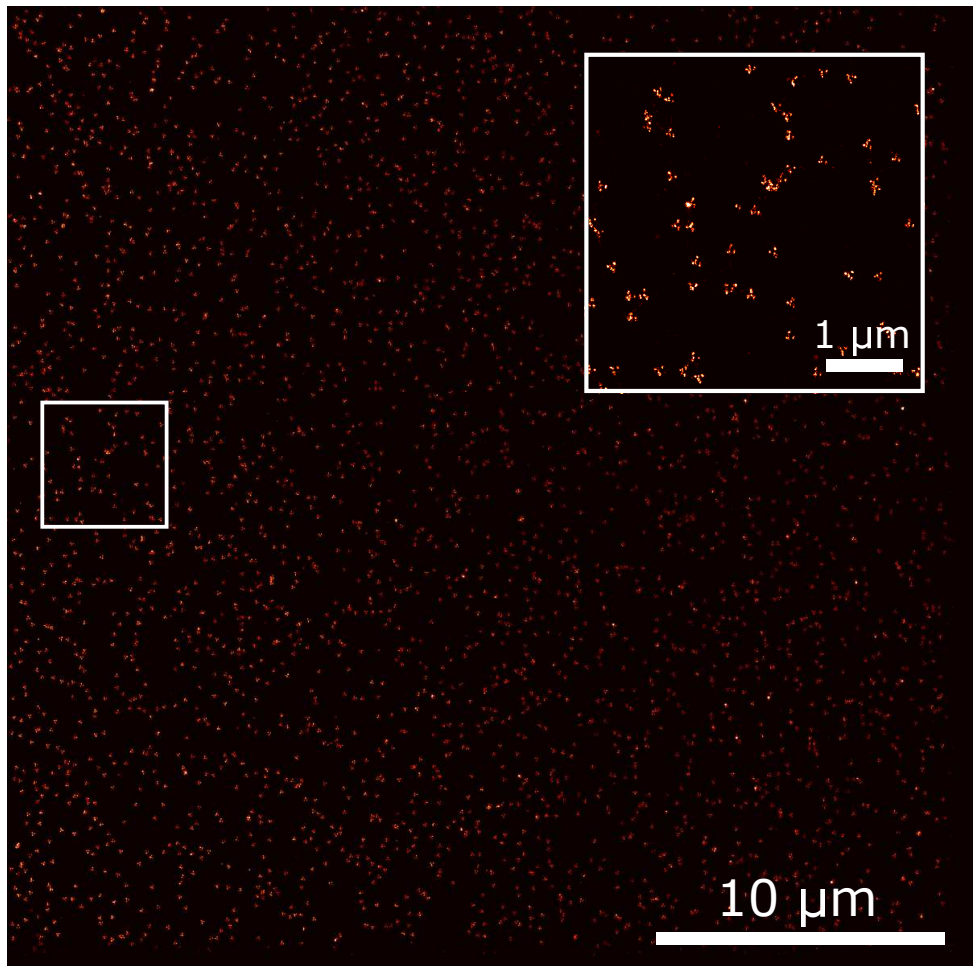


Figure 3.A8: Whole field of view of three-dimensional DNA origami tetrahedron structures imaged with DNA-PAINT on a spinning disk microscope. The side length of the symmetric tetrahedron structure is 100 nm. The insert in the top-right corner presents a zoom in into the highlighted area.

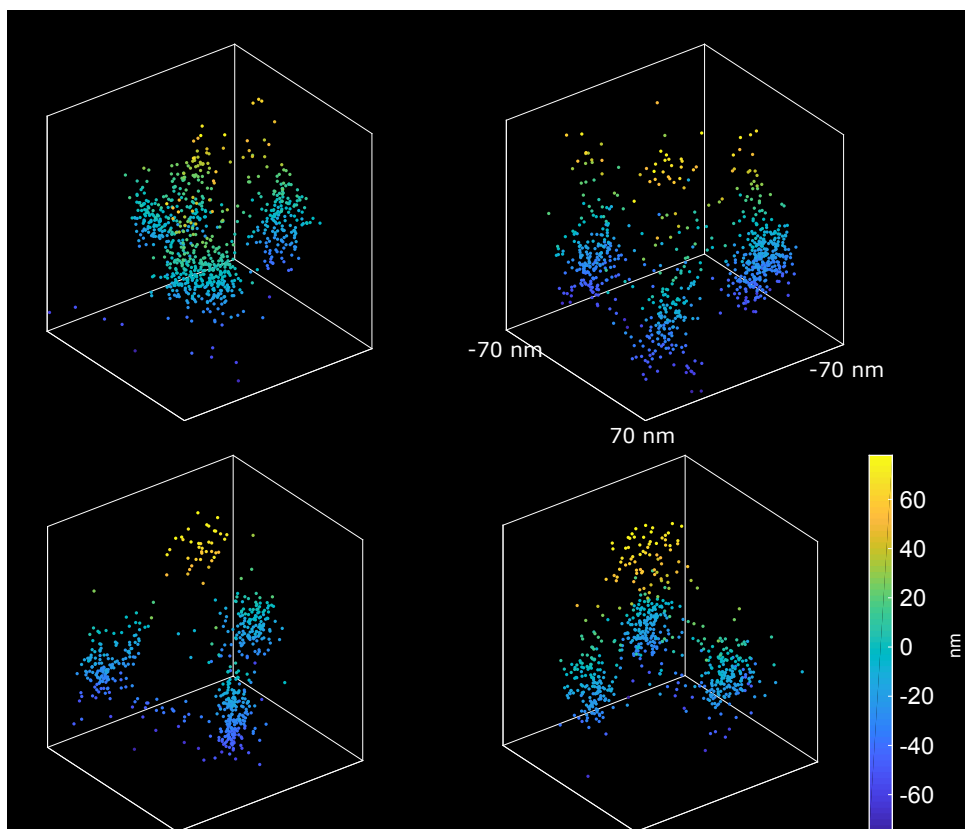


Figure 3.A9: Example images of tetrahedron DNA-origami nanostructures imaged with PAINTE.

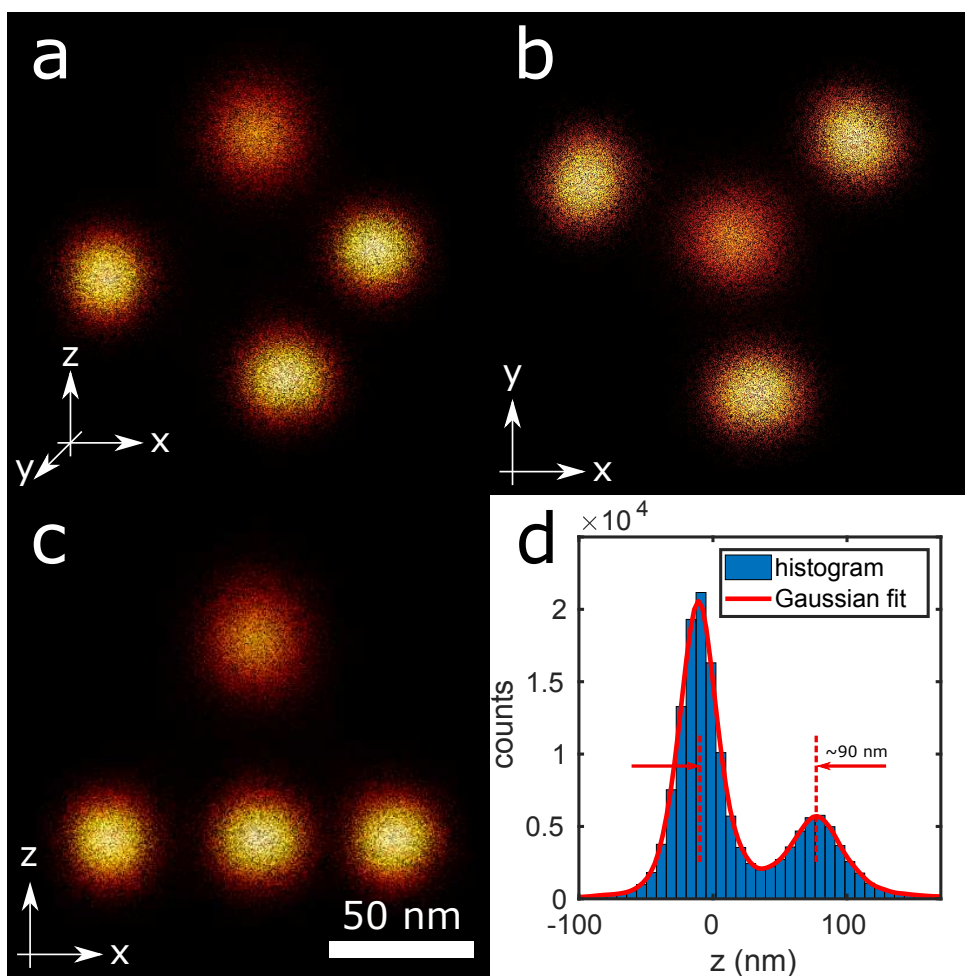


Figure 3.A10: Fusion of 256 tetrahedron DNA-origami nanostructures. (a) Side view of the super-particle. (b) Top (x-y) view of the super-particle. (c) Front (x-z) view of the super-particle. (d) Histogram of the z coordinate of the localization data showing a distance of ~ 90 nm between the two peaks. Particle fusion of the nanostructures result in an isotropic distribution of the localization over the four binding sites of the tetrahedron as seen from the round localization distributions around the binding sites.

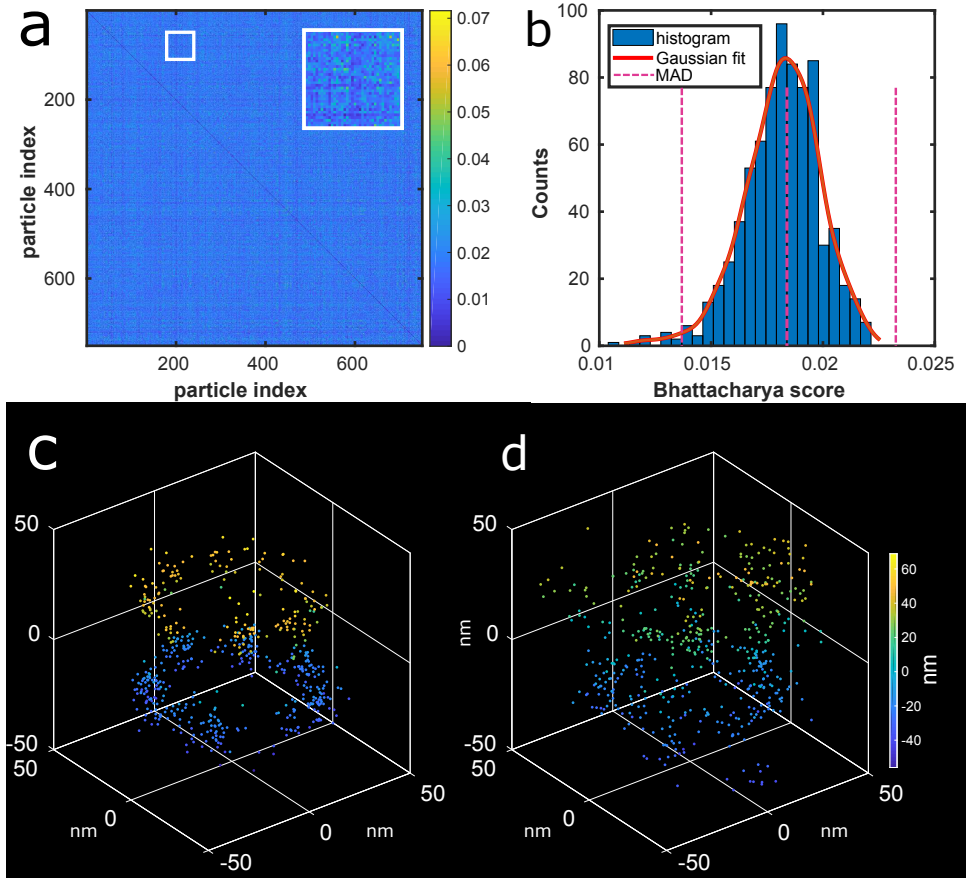


Figure 3.A11: | Outlier particle removal. (a) All-to-all Bhattacharya heat map matrix for the fusion of 750 particles from the 4Pi dataset. Each value is rendered as a pixel in a 750×750 image. (b) The histogram of the Bhattacharya scores (cost function value) of each particle which is obtained by averaging the matrix in a along the columns (or rows) together with the median absolute deviations (MAD) magenta line magenta and its lower and upper bounds. Only 9 particles are recognized as outliers in this dataset with these default settings of the MAD threshold. (c) Overlay of the localizations of the best particles (20 top scores). (d) Overlay of the localizations of the worst particles (20 lowest scores). While the (good) particles in c form a sharp super-particle, the overlay in d is quite blurry and the localizations are more scattered around the NUP structure.

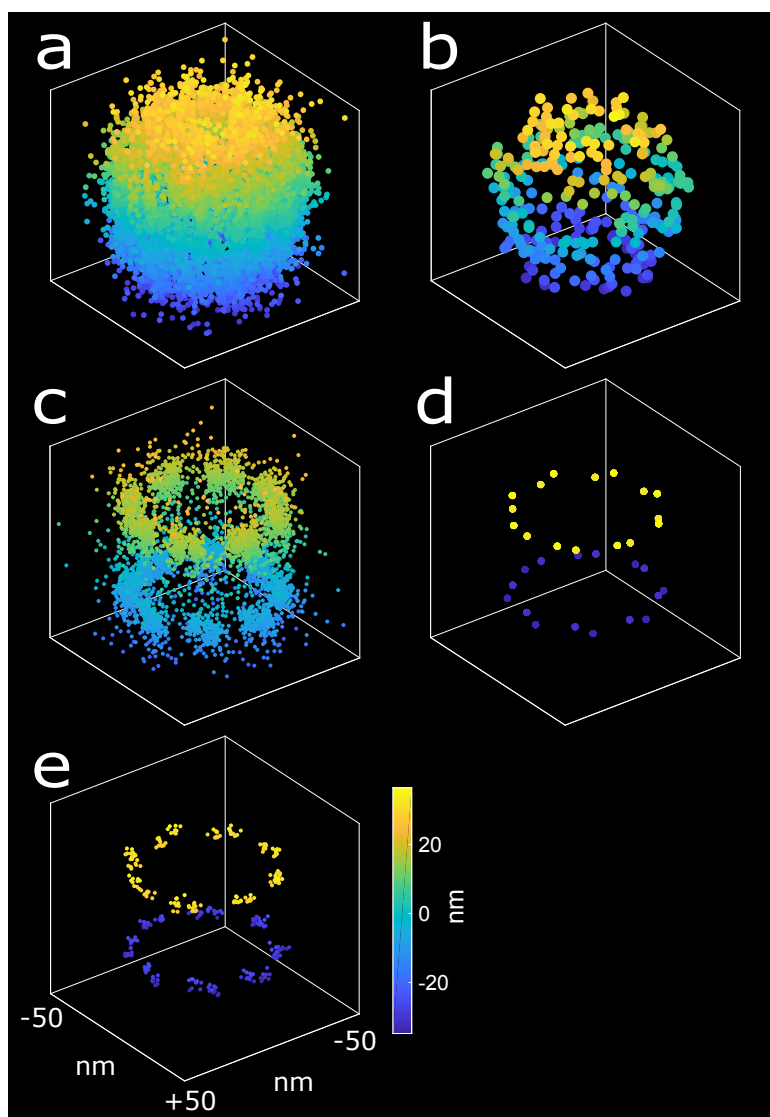


Figure 3.A12: The principle of the proposed registration error measurement. (a) Overlay of 10 simulated particles before alignment. (b) Overlay of the binding sites of the particles in a. (c) Superparticle as a result of fusing the particles in a. (d) The corresponding binding sites of the aligned particles in c in a perfect fusion (zero measurement error). (e) The corresponding binding sites of the aligned particles in c with the effect of the registration error taken into account. Ideally and in a perfect fusion, all the binding sites of the ground-truth simulation model should co-locate. Due to the registration error they scatter around the mean shape model of the super-particle. The corresponding registration error for a run of the particle fusion pipeline is found by quantifying this scatter.

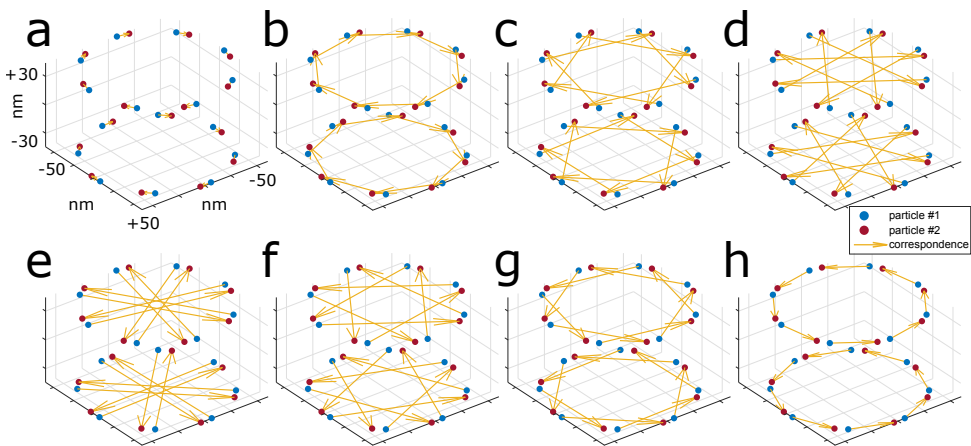


Figure 3.A13: Correspondence problem in matching binding sites of two aligned particles. (a-h) Different correspondence possibilities for computing the error between the registered particles with registration error. In this example, each particle includes 16 binding sites. Since the binding sites are ordered, there are only 8 different combinations of the correspondences between them. The minimum Euclidean distance among these eight candidates defines the correct correspondence and its value is the alignment error.

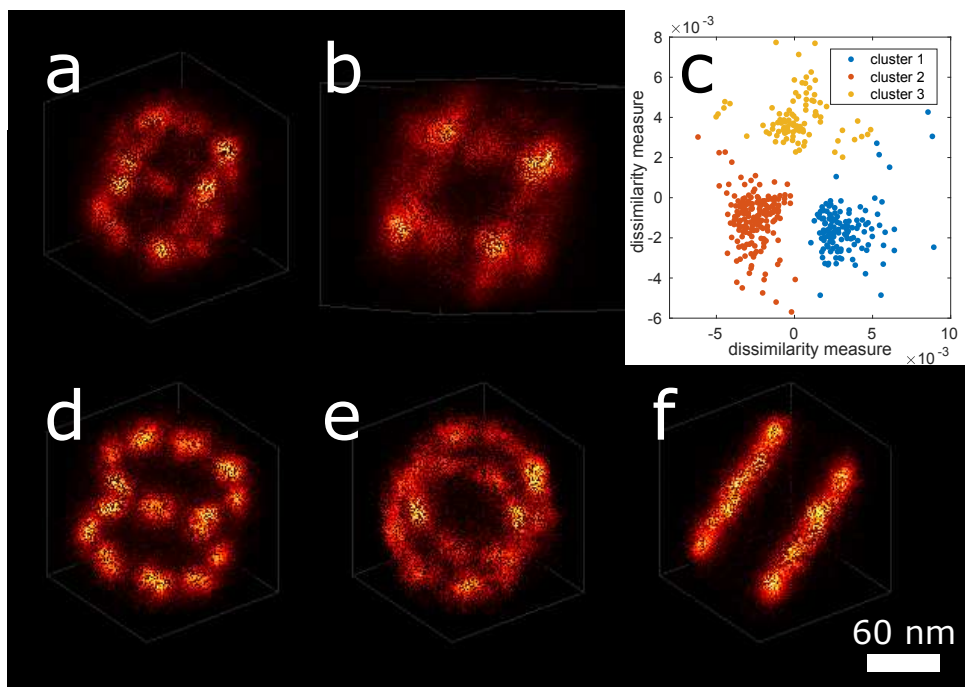


Figure 3.A14: | Fusion of particles with arbitrary poses. (a-b) Two views of the initial super-particle after the bootstrapping step for fusing 400 simulated PAINT particles. (c) K-means clustering ($k = 3$) on multi-dimensional scaling of the dissimilarity matrix of the all-to-all matrix. (d-f) Three clusters of particles which are separated using the proposed method each containing 176, 96 and 128 particles, respectively. When the initial particles have arbitrary poses, the particle fusion results in clusters of particles which are aligned together. To separate these clusters, the all-to-all Bhattacharya score matrix can be used to map them to the two-dimensional Cartesian space using multi-dimensional scaling (MDS). By clustering the MDS, particles which are aligned together can be automatically separated.

4

CONCLUSION AND OUTLOOK

4.1. CONCLUSION

Single molecule localization microscopy (SMLM) has provided us with the ability to look at macromolecular structures and complexes at a resolution of around 20 nm. This resolution is limited because practical difficulties with sample preparation stand in the way of a complete and dense labeling of the structures of interest. Also, the number of photons that is collected per emitting fluorophore is limited, which subsequently results in a low localization precision. Particle fusion is an attempt to mitigate in particular the first shortcoming by aggregating the information content in SMLM images of multiple imaged copies of the same structure [1].

Particle fusion can be considered as a variant of groupwise image or point cloud registration, which is a well-established topic in image processing and computer vision. Despite the similarity in the problem statement, unique features of SMLM data make it very difficult to directly utilize existing methods for SMLM particle averaging. These are, among others, the inherent heterogeneity of the set of particles due to severe underlabeling, different types of noise sources, different geometrical constellations of the points (localizations) within the particles, i.e. true volumetric versus planar or surface data, and the necessity to take into account relevant information in addition to the localization coordinates such as localization uncertainties and symmetries.

This thesis proposed a new approach for particle fusion dedicated to SMLM data which properly takes into account localizations and the corresponding uncertainties. It does not need any prior knowledge of the underlying structure but can exploit geometrical features like symmetry into the fusion pipeline. It works both for 2D (chapter 2) and 3D (chapter 3) data in their native format, i.e. points represented by Cartesian coordinates without reference to a pixel or voxel grid, and finally makes use of the maximum pairwise information available from the data, providing redundancy and robustness.

We evaluated the performance of the developed image processing pipeline on two SMLM imaging techniques, PAINT and STORM, and characterized the needs for successful reconstruction for both modalities on experimental data. In 2D, we achieved an impressive FRC resolution of 3.3-5.0 nm by fusing hundreds of DNA-origami nanostructures displaying the TUD logo at different labeling densities. In 3D, we performed particle fusion on 3D Nup107 NPCs imaged using different SMLM modalities and setups to show the potentials that our developed pipeline provides for structural biology. By an extensive simulation study, we explored different experimental conditions that touch the envelope of the method, i.e. the boundary conditions of the experimental parameters within which the pipeline works, and the ultimate resolution that can be achieved given a particular set of experimental parameters. In addition, this thesis has provided the community with an open source tool for structural analysis of biological macromolecular complexes with SMLM.

In the following sections, I will discuss ways in which the current processing pipeline can be improved in the short-term (section 2), and subsequently, I will present avenues for future research in a more general context of data fusion (section 3).

4.2. SHORT-TERM OUTLOOK

HOTSPOT PROBLEM

In SMLM, the localizations are not uniformly distributed over the binding sites in particles, i.e. some sites get more localizations compared to the others. The distribution is even different from one imaging modality to the other. While in STORM, the localizations per binding site follows a mixed geometric-Poisson distribution, due to the bleaching of the fluorescent molecules [2], in PAINT, this distribution is Poissonian, as there is no bleaching. In chapters 2 and 3, we showed that the so-called hotspot problem is inevitable for highly underlabeled data, because the particle fusion algorithm always tries to match dense regions in one particle to dense regions in another particle, leading to an accumulation of localizations in such dense regions during the entire particle fusion process. This problem could be solved by incorporating the rotational symmetry information in the bootstrapping stage of the pipeline. Alternatively, symmetry or any other prior knowledge can be considered earlier, at the all-to-all registration phase. This can be advantageous as it reduces the search space considerably even for very simple symmetries like the eight-fold symmetry of the NPC structure. To achieve this, one needs to optimize the cost function on the appropriate subgroup of the full special Euclidean group of rotations and translations $SE(n)$, in which $n = 2$ or $n = 3$ is the dimension, which in simple cases like the NPC is the point symmetry group [3]. This is, however, nontrivial as these symmetry subgroups cannot be represented easily on smooth manifolds.

The Bhattacharya cost function is based on the one-to-one localization distances and their uncertainties. Another way of preventing the hotspot problem is to modify the cost function in such a way that it penalizes the local density of the localizations. In this way, we can down-weight the localizations in very dense regions to avoid accumulation of localizations. Ideas from previous studies in point set registration [4] and in clustering of unbalanced data [5] could provide directions to address the problem in this way.

GPU ACCELERATION

In our particle fusion pipeline, there are two levels of parallelism which can improve the computational time of the algorithm to a large extent. At the lowest level, the Bhattacharya cost function can be evaluated in a highly parallel manner as it requires the calculation of the exponential distance of each single localization in one particle to all localizations in the other particle. In the current version of our code, this computation is already implemented both on CPU and GPU. At a higher level, we have the computation of the all-to-all registration matrix. Given N particles, there are $N(N-1)/2$ independent pair-wise registrations that can in principle be done simultaneously. This, however, is not a trivial task as solving each pair-wise registration is a constrained optimization problem, which is difficult to implement on a GPU core as its stepping algorithm is sequential. Currently, we make use of different CPU cores to accelerate the computation of these parallel problems, which is limited to tens of cores on typical hardware setups in labs. Implementing this constrained optimization on a GPU can considerably speed up the pipeline, as each individual problem is not computationally very expensive.

OPTIMIZATION ON A MANIFOLD

The particle fusion pipeline, at its core, optimizes a cost function for 2D/3D registration parameters for each pair of particles. The rigid registration parameters that parameterize the special Euclidean group $SE(n)$ include rotation angle(s) and translation vector components. In our 3D optimization of the cost function we have used the quaternion representation of rotations. Generally, groups can be parameterized in different ways. Exploration of these ways, so-called optimization on the manifold [6], could enable a reduction in the search space during the optimization, reducing computation times and increase robustness. In addition, it could make it possible to better take into account group properties such as symmetries.

INCREMENTAL FUSION

Ideally, $N-1$ pair-wise registrations are enough for the alignment of N given particles. In practice, however, this minimum number is not enough, due to registration errors and low-quality particles. For that reason, we have made use of the maximum available information in our data by averaging all $N(N-1)/2$ registrations. In the outlier registration removal phase of the developed pipeline we have observed that much of this redundant information can be ignored without affecting the quality of the final reconstruction. Therefore, it seems reasonable to investigate the possibility of incremental fusion of the particles. In this setting, one can start with the minimum spanning tree of the connecting graph of all particles (see Chapter 2) and then gradually add more pair registrations until the superparticle reaches a certain quality criterion. The big challenge to implement this idea is to modify the Lie-algebraic averaging such that the result of averaging a subset of registrations (elements in $SE(3)$) in the all-to-all matrix can be used for averaging a larger subset up to the maximum number of entries $N(N-1)/2$.

BOOTSTRAPPING STOPPING CRITERION

It turned out that bootstrapping improves the quality of the superparticle to a satisfactory state in just a few iterations. We have not, however, investigated an automatic way of stopping the iterations. A possible suitable stopping criterion is to look at the Bhattacharya cost function value between each single particle and the superparticle at each iteration of the bootstrapping and find the point where this value converges or does not change significantly anymore.

SOFTWARE DISTRIBUTION

The developed pipeline is open source and publicly available for users to download and run [7]. However, the main core of the software is written in MATLAB [8] which is a commercial software package. In the 3D study, we have already provided a wrapper which made the software accessible for users without a MATLAB license. Unfortunately, a potential user still needs to install the MATLAB runtime library, which may be impractical for users without administrative rights on their machines. Considering the potential of other programming languages and the simplicity of the developed pipeline, a good extension to this work could be to port the software to completely open source platforms like Python, C or C++.

4.3. LONG-TERM OUTLOOK

Future advances in SMLM will continue to enhance the achievable resolution in light microscopy and improve our understanding of the nanoworld. There are many possibilities for developing computational routines to gain as much information out of the acquired data as possible, next to opportunities in sample preparation, labeling strategies and microscopy setups. In the following, I briefly sketch directions of research in particle averaging for localization microscopy:

PARTICLE PICKING

So far, we assumed that the relevant particles are properly segmented from the whole field of view. For the experimental datasets in chapter 2-3 of this thesis, this was done by two-dimensional rendering of the big SMLM images using Picasso [9] and then manually picking the relevant particles. In 2D, software packages from EM [10, 11] are available that can perform automatic particle picking by training neural network on hand-picked particles from the data. In our very basic investigations, we observed that direct use of these software packages on SMLM data is only useful when the quality of the data, especially the labeling density, is high and the particles are well separated over the field of view. This could be primarily due to the fact that the architecture of these networks is not suitable for the SMLM modality, which is very different from EM. Therefore, designing new neural network architectures can be helpful for automatic particle picking. In 3D, one can first project the data along one axis, if the underlying structure lies on a 2D plane like NPCs in the cell membrane, and then uses 2D routines as before. However, in many situations, this is not the case and the particles can have an arbitrary orientation in 3D. Therefore, one needs to invent new approaches for automatic particle picking in 3D. Deep learning approaches from the computer vision community can be inspiring in this regard [12–14].

PARTICLE HETEROGENEITY

SMLM data acquired for particle fusion can consist of multiple structures in one field of view [15] and it is then necessary to make an initial separation of the subclasses before the start of the fusion. Even within one class of particles structural variations are expected for many biological structures. These variations can arise from biological dynamics, deformation of the cellular structure, or phenotypical variations, e.g. sometimes the NPC can be nine-fold symmetric [16]. Although there are many approaches in the field of image processing and computer vision for multiclass object detection in natural images (see for example [17, 18]), they are not readily useful choices for SMLM particle discrimination. This is primarily due to the inherent source of heterogeneity in SMLM dataset as a result of underlabeling. SMLM particles, even in one class, exhibit too much shape variations that make inter-class differentiation very hard. If different classes are known in advance, then the fusion of particles of good quality (hand-selected and within each class) and resampling them to regenerate synthetic datasets to produce various examples in the population can be an option for developing learning methods to separate different classes. If, however, the number of unlike particles is low compared to the whole set one can use a distance measure, like Bhattacharya cost function, to rank similarities of the particles after fusion (see Chapter 3).

INPAINTING OF INITIAL PARTICLES

Alternatively to all the approaches proposed in the previous section to avoid hotspot problem in the implemented pipeline, one can inpaint the initial particles using structural prior knowledge. As an example, for NPC data, it is possible to replicate each individual particle eight times around its symmetry axis on multiples of $2\pi/8$ to have a uniform distribution of localizations over the binding sites and then start the particle fusion. Once all particles are aligned, the spurious localizations can be removed easily from the superparticle afterward. This is very similar to 3D single particle reconstruction in cryo-EM where the asymmetric unit is replicated according to the symmetry class of the particle [10]. The big problem to be solved, here, is to find the axis(es) of symmetry in the initial particles which can be challenging if the pose variation within the set of particles is high.

4

HOW MANY PARTICLES DO WE NEED?

Acquiring SMLM data can be very challenging and time consuming especially for new modalities like expansion microscopy [19]. Therefore, it is always good to know in advance how many particles one needs to acquire in order to achieve a certain resolution or quality. We empirically found that 50-100 particles are enough to achieve a registration error of about 8 nm according to the metric we proposed for fusion of 3D NPCs [20]. A theoretical framework needs to be established to generalize this for arbitrary structures and modalities.

MULTICHANNEL PARTICLE FUSION

Multicolor SMLM enables researchers to colocalize different molecular structures such as proteins at nanometer resolution. Our particle fusion pipeline, however, is only capable of single-channel fusion. In chapter 3 of this thesis, we showed the possibility of multicolor alignment of 3D data by applying the estimated transformations from one channel to the other. In that experiment, the secondary channel data was an unstructured complex. If the particles in different channels do not conform to each other geometrically, e.g. have different rotational symmetry groups, the approach that we took does not work anymore. Even without enforcing symmetry at the bootstrapping phase, the pairwise registration in the beginning of the pipeline is subject to nonunique solutions due to the symmetry in one channel that is not necessarily compatible with the symmetry in the other channel. New cost functions need to be devised which can perform joint alignment of multichannel data.

INCORPORATION OF ADDITIONAL INFORMATION

The estimated fluorescent molecule locations (2/3D coordinates) are not the only measured parameters that are obtained in an SMLM experiment. Localization uncertainties, photon count per molecule, frame number, background and even sometimes dipole orientation are other sources of information that may be available in SMLM data. Despite this rich content, scientists usually look at the localization data and use summary statistics for the other data. This is mostly due to the fact that the inference of the other information is not straightforward. In our particle fusion pipeline, we incorporated the localization uncertainties along with the localizations. However, there are still possibilities

to include the other mentioned information sources in the fusion pipeline. This would need new cost functions that can properly integrate different sources of information for particle alignment.

REGISTRATION ERROR MEASUREMENT

Quantitative assessment of the superparticle resulting from the fusion of many particles is an essential step in developing better particle fusion algorithms and also to find the requirements for a successful fusion. Visual inspection, measures like Fourier Ring Correlation (FRC) [21] and decorrelation analysis [22], and finally prior knowledge-based approaches like what we presented in chapter 3 of this thesis are the available tools for quality assessment of a superparticle. FRC does not necessarily correspond to the registration error as a superparticle can have a very low registration error according to the method we developed but still have a large FRC (low resolution) at the same time (see chapter 2, Supplementary Figure 3). The error measure that we proposed in chapter 3 does properly measure registration errors of simulated data but is structure dependent and needs to be reparametrized for other structures. Considering these limitations, it seems necessary to develop new approaches that can quantify registration error without having an established ground-truth model for the structure at hand.

ADVANCED ANALYSIS TOOLS

Particle fusion shows promise for new inroads to structural analysis of subcellular complexes. This is, however, dependent on the availability of statistical routines for the analysis of 2/3D point patterns. In chapter 3 of this thesis, we used basic tools such as histogram (radial and circular) fitting to characterize the geometry of Nup107, e.g. for finding the azimuthal phase shift of the two Nup107 rings. Advanced tools can be adapted from the field of spatial statistics [23, 24], which deals with statistical analysis of spatial data, applied mostly in remote sensing. Cluster analysis, quantitative assessment of labeling density, drift, molecular photophysical properties and pose variation of cellular structures are among the range of interesting topics that can be explored in this regard.

As an example, we used the result of fusing the highly underlabeled TUD dataset (30% density of labeling (DOL)) for investigating if the hotspot problem in the reconstructed superparticle is real or an artefact caused by the fusion algorithm. We clustered each aligned superparticle using the Gaussian Mixture (GM) approach, as described in [25], with an estimated number of components of 20 (more than what is expected for 30% labeled data). Then, we filtered the least significant Gaussian components using the saliency scores that the algorithm provides. Finally, the localizations of each component are assigned to the nearest binding sites in the origami design.

Figure 4.1 demonstrates our final analysis on the underlabeled superparticle. Each ellipse in this figure represents one standard deviation of the aggregated Gaussians for each binding sites. The black crosses show the estimated center of these clusters which are quite often away from their actual positions in the origami design (center of the red circles). Furthermore, the number of times each binding site is activated is color-coded to show how often each site is activated. The visualization clearly shows that site activation is not uniform. Some sites are activated more often than the others (3 times in the worst case), the edges are among those sites with low chance of activation, in accor-

dance with [26], and the hotspot problem is indeed real in the acquired data and it is not a particle fusion artefact.

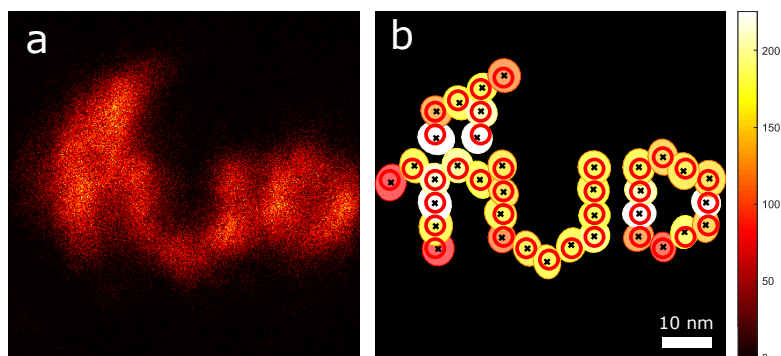


Figure 4.1: Analysis of the superparticle for the 30% DOL experimental dataset of chapter 2. (a) Superparticle. (b) Cluster analysis and number of localizations per binding site. The analysis shows non-uniform activation of the binding sites in addition to deviations of the cluster centers (red circles) from the ground-truth binding sites (black crosses).

REFERENCES

- [1] Hamidreza Heydarian, Florian Schueder, Maximilian T. Strauss, Ben van Werkhoven, Mohamadreza Fazel, Keith A. Lidke, Ralf Jungmann, Sjoerd Stallinga, and Bernd Rieger. Template-free 2d particle fusion in localization microscopy. *Nature Methods*, 15(10), 2018.
- [2] Robert P. J. Nieuwenhuizen, Mark Bates, Anna Szymborska, Keith A. Lidke, Bernd Rieger, and Sjoerd Stallinga. Quantitative localization microscopy: Effects of photophysics and labeling stoichiometry. *PLOS ONE*, 10(5), 05 2015.
- [3] S.L. Altmann. *Rotations, Quaternions, and Double Groups*. Dover Publications, 2005.
- [4] F. J. Lawin, M. Danelljan, F. S. Khan, P. Forssén, and M. Felsberg. Density adaptive point set registration. In *2018 IEEE/CVF Conference on Computer Vision and Pattern Recognition*, 2018.
- [5] D. Marin, M. Tang, I. B. Ayed, and Y. Boykov. Kernel clustering: Density biases and solutions. *IEEE Transactions on Pattern Analysis and Machine Intelligence*, 41(1), 2019.
- [6] Nicolas Boumal, Bamdev Mishra, P.-A. Absil, and Rodolphe Sepulchre. Manopt, a matlab toolbox for optimization on manifolds. *J. Mach. Learn. Res.*, 15(1), 2014.
- [7] H. Heydarian, Werkhoven B., and Rieger B. Software for template-free 2d particle fusion in localization microscopy. 2018. URL https://github.com/imphys/smlm_datafusion2d.

- [8] Matlab. URL <https://www.mathworks.com/products/matlab.html>.
- [9] Joerg Schnitzbauer, Maximilian T. Strauss, Thomas Schlichthaerle, Florian Schueder, and Ralf Jungmann. Super-resolution microscopy with dna-paint. *Nature Protocols*, 12(6), 2017.
- [10] Guang Tang, Liwei Peng, Philip R. Baldwin, Deepinder S. Mann, Wen Jiang, Ian Rees, and Steven J. Ludtke. Eman2: An extensible image processing suite for electron microscopy. *Journal of Structural Biology*, 157(1), 2007.
- [11] Thorsten Wagner, Felipe Merino, Markus Stabrin, Toshio Moriya, Claudia Antoni, Amir Apelbaum, Philine Hagel, Oleg Sitsel, Tobias Raisch, Daniel Prumbaum, Dennis Quentin, Daniel Roderer, Sebastian Tacke, Birte Siebolds, Evelyn Schubert, Tanvir R. Shaikh, Pascal Lill, Christos Gatsogiannis, and Stefan Raunser. Sphire-cryolo is a fast and accurate fully automated particle picker for cryo-em. *Communications Biology*, 2(1), 2019.
- [12] Martin Simon, Stefan Milz, Karl Amende, and Horst-Michael Gross. Complex-yolo: An euler-region-proposal for real-time 3d object detection on point clouds. Computer Vision ECCV 2018 Workshops. Springer International Publishing, 2018.
- [13] Charles Ruizhongtai Qi, Wei Liu, Chenxia Wu, Hao Su, and Leonidas Guibas. Frustum pointnets for 3d object detection from rgb-d data. 06 2018.
- [14] Y. Zhou and O. Tuzel. Voxelnet: End-to-end learning for point cloud based 3d object detection. In *2018 IEEE/CVF Conference on Computer Vision and Pattern Recognition*, 2018.
- [15] Mingjie Dai, Ralf Jungmann, and Peng Yin. Optical imaging of individual biomolecules in densely packed clusters. *Nature Nanotechnology*, 11(9), 2016.
- [16] Anna Löschberger, Christian Franke, Georg Krohne, Sebastian van de Linde, and Markus Sauer. Correlative super-resolution fluorescence and electron microscopy of the nuclear pore complex with molecular resolution. *Journal of Cell Science*, 127(20), 2014.
- [17] Joseph Redmon and Ali Farhadi. Yolov3: An incremental improvement. *arXiv preprint arXiv:1804.02767*, 2018.
- [18] Shaoqing Ren, Kaiming He, Ross Girshick, and Jian Sun. Faster r-cnn: Towards real-time object detection with region proposal networks. *IEEE Trans. Pattern Anal. Mach. Intell.*, 39(6), 2017.
- [19] Davide Gambarotto, Fabian U. Zwettler, Maeva Le Guennec, Marketa Schmidt-Cernohorska, Denis Fortun, Susanne Borgers, Jörn Heine, Jan-Gero Schloetel, Matthias Reuss, Michael Unser, Edward S. Boyden, Markus Sauer, Virginie Hamel, and Paul Guichard. Imaging cellular ultrastructures using expansion microscopy (u-exm). *Nature Methods*, 16(1), 2019.

- [20] Hamidreza Heydarian, Adrian Przybylski, Florian Schueder, Ralf Jungmann, Ben van Werkhoven, Jan Keller-Findeisen, Jonas Ries, Sjoerd Stallinga, Mark Bates, and Bernd Rieger. Three dimensional particle averaging for structural imaging of macromolecular complexes by localization microscopy. *bioRxiv*, 2019.
- [21] Robert P. J. Nieuwenhuizen, Keith A. Lidke, Mark Bates, Daniela Leyton Puig, David Grünwald, Sjoerd Stallinga, and Bernd Rieger. Measuring image resolution in optical nanoscopy. *Nature methods*, 10(6), 2013.
- [22] A. Descloux, K. S. GrusSmayer, and A. Radenovic. Parameter-free image resolution estimation based on decorrelation analysis. *Nature Methods*, 16(9), 2019.
- [23] B.D. Ripley. *Spatial Statistics*. Wiley, 1981.
- [24] J. Illian, P.A. Penttinen, H. Stoyan, and D. Stoyan. *Statistical Analysis and Modelling of Spatial Point Patterns*. Wiley, 2008.
- [25] Israel Dejene Gebru, Xavier Alameda-Pineda, Florence Forbes, and Radu Horaud. Em algorithms for weighted-data clustering with application to audio-visual scene analysis. *IEEE Trans. Pattern Anal. Mach. Intell.*, 38(12), 2016.
- [26] Maximilian T. Strauss, Florian Schueder, Daniel Haas, Philipp C. Nickels, and Ralf Jungmann. Quantifying absolute addressability in dna origami with molecular resolution. *Nature Communications*, 9(1), 2018.

SUMMARY

Single molecule localization microscopy (SMLM) shows promise for quantitative structural analysis of subcellular complexes and organelles with a resolution well below the diffraction limit. This superresolution microscopy technique relies on the blinking events of fluorescent molecules that labeled the structure of interest and are spatiotemporally spread over the entire field of view and time. Once hundred thousands frames of these sparse events are recorded, single molecule positions are localized with nanometer precision to form a 2D/3D point set of coordinates. Therefore, SMLM images are not conventional pixelated images but rather spatial point patterns.

Photon scarcity and incomplete labeling of the imaged structure, however, limit the resolution that can possibly be achieved by means of SMLM. Moreover, due to experimental limitations the axial resolution is typically ~2-3 times worse than the lateral resolution in conventional setups. Inspired by single particle analysis (SPA) in cryo-electron microscopy (cryo-EM), proper alignment of repeated structures ("particle fusion") in a 2D/3D SMLM measurement can overcome these limiting factors and so push for isotropic resolution. The existing approaches for particle fusion in SMLM can be classified into customized routines that are borrowed from SPA in EM or methods that use strong prior knowledge about the structure to be reconstructed. While the first approaches are completely ignoring the differences in image formation model between EM and SMLM, the second ones are highly prone to the template-bias problem.

In this thesis, a dedicated particle fusion pipeline for 2D/3D SMLM data is proposed. The approach properly considers the pointillistic nature of the SMLM modality and takes into account the localization uncertainties. Furthermore, while it does not require any prior knowledge about the underlying structure of the particles, it can incorporate certain features such as symmetry into the fusion process. Owing to the novel all-to-all registration scheme, the application of the devised pipeline on experimental data with very poor labeling density has been successfully demonstrated. The requirements for successful particle fusion for different SMLM modalities, namely PAINT and STORM, have been characterized through extensive study on 2D and 3D experimental and simulation data. In 2D, an FRC resolution of 3.3 nm on DNA-origami nanostructures has been achieved, and, in 3D, it was demonstrated how the combination of SMLM as a light microscopy technique and a computational approach enables structural analysis of the Nuclear Pore Complex.

Future advances of SMLM rely highly on computational routines after data acquisition. Advanced data analysis techniques such as particle fusion can help pushing the boundaries of structural biology using light microscopy.

SAMENVATTING

Enkel-molecuul lokalisatiemicroscopie (SMLM) heeft veel potentie voor kwantitatieve structurele analyse van sub-cellulaire complexen en organellen met een resolutie significant onder de diffractie limiet. Deze superresolutie microscopie techniek is afhankelijk van het knippen van fluorescente moleculen die structuren onder studie gelabeld hebben en tijdruimtelijk verdeeld zijn over het hele gezichtsveld en tijd. Als honderdduizenden plaatjes van deze verspreide gebeurtenissen opgenomen zijn, kunnen individuele molecuul posities worden geschat met nanometer precisie om een 2D/3D punt set van coördinaten te creëren. Daardoor zijn SMLM plaatjes geen conventionele gepixelde plaatjes maar spatiele punt patronen.

Een beperkt aantal fotonen en incomplete etikettering van de afgebeelde structuur, begrenzen de resolutie die behaald kan worden met SMLM. Bovendien is de axiale resolutie door experimentele beperkingen typisch ~ 2 - 3 keer slechter dan de laterale resolutie in conventionele opstellingen. Geïnspireerd door enkele deeltjes analyse (SPA) in cryo-elektronenmicroscopie (cryo-EM), kunnen we door goede registratie van herhaalde structuren (deeltjesfusie) in 2D/3D SMLM metingen deze limiterende factoren overwinnen en richting een isotrope resolutie werken. De bestaande methoden voor deeltjesfusie in SMLM kunnen geclassificeerd worden als aangepaste algoritmes die hun oorsprong vinden in het veld van SPA in EM, of als methodes die gebruik maken van voorkennis over de structuur die gereconstrueerd wordt. De eerste aanpak negeert de verschillen in de beeldvormingsmodellen tussen EM en SMLM, de tweede is zeer vatbaar voor het probleem dat het gebruik van een sjabloon vooringenomenheid met zich meedraagt.

Dit proefschrift beschrijft een specifieke deeltjes fusie pijplijn voor 2D/3D SMLM data. Deze methode neemt de pointillistische aard van de SMLM beeldvorming in acht en neemt de lokalisatie onzekerheden ook mee. Daarbovenop heeft de methode geen voorkennis nodig heeft over de structuur van de deeltjes, en kunnen er wel extra kenmerken zoals symmetrie meegenomen worden in het fusieproces. Dankzij het voorgestelde allen-naar-allen registratie stelsel, kan de pijplijn succesvol gebruikt worden voor experimentele data met een zeer lage etiket-dichtheid. Verder worden de eisen voor succesvolle deeltjesfusie voor verschillende SMLM modaliteiten, namelijk PAINT en STORM, gekarakteriseerd door een grondig onderzoek met 2D en 3D experimentele en gesimuleerde data. In 2D wordt een FRC resolutie van 3.3 nm voor DNA-origami structuren behaald, en in 3D wordt aangetoond hoe een combinatie van SMLM als lichtmicroscopie-techniek en een rekenkundige aanpak de structurele analyse van kernporiecomplexen mogelijk maakt.

Toekomstige stappen in SMLM berusten voor een groot gedeelte op algoritmes toegepast op de vastgelegde data. Geavanceerde data-analysetechnieken zoals deeltjesfusie kunnen helpen om grenzen te verleggen in structurele biologie gebaseerd op lichtmicroscopie.

CURRICULUM VITÆ

Hamidreza Heydarian was born in Mashhad, Iran on June 29, 1985. He received the B.S. and M.S. degrees in electrical engineering from Ferdowsi University of Mashhad, Iran, in 2007 and 2010, respectively. In 2009, he cofounded Payatech, a startup company in the field of biomedical engineering and instrumentation and was working there for three years.

He left the company in 2012 and moved to Germany to study visual computing, a specialized master program in the field of image processing and computer vision. He obtained his second master degree under the supervision of professor J. Weickert in 2015 in the Mathematical Image Analysis (MIA) group at Saarland University, Germany.

In October 2015, he started as a PhD student under the supervision of professor B. Rieger and S. Stallinga in the Computational Imaging group of the Imaging Physics (Im-Phys) department of the Applied Sciences faculty at TU Delft. In his research, he focused on the analysis of single molecule localization microscopy (SMLM) data to develop computational algorithms for improving the achievable resolution in SMLM.

ACKNOWLEDGEMENTS

"In the Name of Allah, the All-merciful, the All-compassionate, My God, the uninterrupted flow of Thy graciousness hast distracted me from thanking Thee! The flood of Thy bounty has rendered me incapable of counting Thy praises! The succession of Thy kind acts has diverted me from mentioning Thee in laudation! The continuous rush of Thy benefits has thwarted me from spreading the news of Thy gentle favours! This is the station of him who confesses to the lavishness of favours, meets them with shortcomings, and witnesses to his own disregard and negligence. Thou art the Clement, the Compassionate, the Good, the Generous, who does not disappoint those who aim for Him ..."¹

It is my pleasure to express my gratitude to everyone who has helped me in any way to get this work done.

I should start by thanking **Joachim Weickert**, my supervisor during my master studies, for introducing me to the field of image analysis and for suggesting me to contact **Lucas van Vliet** for doing a PhD in his group. I initially wrote an email to Lucas to work with him and he forwarded my email to **Bernd Rieger** for the vacancy he had at that time. I did not had the chance to directly work with Lucas during my PhD but the few discussions that I had with him during coffee breaks or around the campus were indeed inspiring and helpful. Thanks Lucas for your support and helpful advice.

I would like to give special thanks to **Bernd Rieger** and **Sjoerd Stallinga**, my supervisors during my PhD studies. We had a lot of great discussions during our weekly meetings which were continuously held during the four years of my PhD. You helped me a lot to learn about a field which I was not familiar with in the beginning. You gave me the opportunities to attend a lot of conferences, workshops and courses to develop my research related skills and also develop my network in the field. I also learned from you how to have a critical mind to analyze the problems and ideas, during the seminars that we had in our group or department, when you always could challenge the presenter with your relevant questions and comments. My special thanks to you for all your support and what I have learned from you.

I would like to recognize the invaluable assistance that the staff members of the Computational Imaging group provided during my PhD studies. **Annelies** and **Angela**, thanks for your great support for helping me handling the issues and problems related to my project, work and life in the Netherlands. **Ronald** and **Ron**, thank you for your great and important technical support and for all general discussions that we had. Thanks to **Nicolette** for perfect organization and management of the ImPhys department.

I would like to also acknowledge other faculty members in our group and department for the useful and inspiring feedbacks during the seminars and the fruitful discussions

¹Al-Sahifa al-Sajjadiyya, The Whispered Prayer of the Thankful (Shakereen)

that we had every now and then around the coffee machine. I would like to especially name **Frans Vos, Jeroen Kalkman, Jaap Caro** and **Sebastian Weingärtner**.

Special thanks go to my colleagues at Computational Imaging and Medical Imaging groups at the ImPhys department. We have shared great times during coffee breaks, lunch, day-out and seminars. I thank my previous officemates **Robert Nieuwenhuizen** and **Tian** and my current officemate **Wenxiu**. I always enjoyed talking to **Leon, Christian, Jelle, Jos (de Wit), Jos (van Rooij), Yan, Taylor, Martijn, Rasmus, Gyllion, Bolling, Willem, Juan** and **Arnica**. I must thank **Robert Moerland** for great moments that we had during the time he was working here or the conferences that we attended together and the great moments that he recorded with his camera at different events in our group. I would like to also thank my Iranian colleagues in our department **Mojtaba, Babak, Mohammad, Moein, Verya** and **Mohsen**.

During the past ten years, I have been in contact with friends through social media whom I have rarely met but our friendship has been as deep and meaningful as long-standing friendships in the real world. First of all, I would like to thank **Hatef (Kharchangzade)** who has been my oldest and closest friend on social media since 2008. I would like to thank **Sarkar Ostovar, Esmail MP, Peykan, Abolfazl, Khoushonat, Sirous, Amirhassan, Bisim, Benyamin, Akbarzade, Terakmeh, Hadian, Zamani** and **Danesh-talab** for the great moments, discussions and interactions that we have had during these years on Facebook, Friendfeed and Telegram.

I wish to also express my gratitude to two of my teachers. I would like to first thank **Mr. Shaerbaaf**, my math teacher at Shahed 11 secondary school, who had great impact on my studies and field of interest. One of the greatest opportunity that I had during my academic life was to attend the lectures offered by **Reza Lotfi** during my Bachelor study at Ferdowsi University of Mashhad. **Reza** was a great teacher and later a great colleague and friend of mine and I always enjoyed meeting and talking to him.

I want also to thank my friends and classmates, **Massoud, Sahamoddin, Sajjad, Ehsan, Javad (Asgari)** and **Javad (Ghalibafan)**. I would like to acknowledge all of you for the great memories that we had together. We were not only friends but indeed brothers.

Much appreciation goes to my family members abroad, **Amir, Boshra, Hanieh** and **Ali** for all the memorable gathering that we have had here in the Netherlands and in Germany. Your presence was and is really a blessing for me in the absence of my family.

I would like to present my sincere thankfulness to my dear parents **Marziyeh** and **Nader** and my brother **Alireza** for their great role in my life and their numerous sacrifices for me. The one thing that I missed the most when I moved abroad were YOU. Thanks for your endless love, prayers and encouragement. *O God, thank them for my upbringing, reward them for honouring me, and guard them as they guarded me in my infancy!*²

I would like to finish this acknowledgement with expressing my deepest gratitude to my wife and love of my life, **Zahra**. I was lucky that our marriage almost coincided with the start of my PhD and I believe that this was not an accident but a precious gift God gave me. You embraced leaving your job and moving with me from Nijmegen to Delft, accepting all the oddities of living with a PhD student. You kept me going on and I would not have been able to finish this thesis without your support and sacrifice. Thanks for your patience and tolerance over these years. This thesis is dedicated to you.

²Al-Sahifa al-Sajjadiyya, Supplication 24 (translation by William C. Chittick)